Consortium

for

Small-Scale Modelling

Newsletter

December 2008 *No. 9*

Deutscher Wetterdienst

MeteoSwiss

ΕΘΝΙΚΗ ΜΕΤΕΩΡΟΛΟΓΙΚΗ ΥΠΗΡΕΣΙΑ

Ufficio Generale Spacio Aero e Meteorologia

Instytucie Meteorogii i Gospodarki Wodnej

Administratia Nationala de Meteorologie

Agenzia Regionale per la Protezione Ambientale dell Piemonte

Agenzia Regionale per la Protezione Ambientale dell Emilia-Romagna: Servizio Idro Meteo

Centro Italiano Ricerche Aerospaziali

Amt für GeoInformationswesen der Bundeswehr

www.cosmo-model.org

Editors: Ulrich Schättler (DWD); Cosmin Barbu (NMA)
Printed at Deutscher Wetterdienst, P.O. Box 100465, 63004 Offenbach am Main

Table of Contents

1 Introduction

As has traditionally been the case, all contributions to this COSMO Newsletter are summaries of presentations given at the last COSMO General Meeting which took place from 15 to 19 September 2008 in Cracow, Poland. The last COSMO General Meeting has been the 10^{th} one in a row, starting from the first meeting in 1999 in Bologna, Italy, and having been hosted in Zurich, Athens, Warsaw, Langen, Milan, Zurich, Bucharest, and Athens, respectively, in the years in between. Within these 10 years, the meetings have grown a lot, starting from a two-day get-together with a list of participants that easily fitted onto a single sheet of paper to a full-week parallel-session event with around 80 colleagues participating. Needless to say that this nicely reflects the success of the COSMO model as well as the fruitful collaboration within the Consortium for Small-Scale Modelling.

Additional to this Newsletter, the final reports of the first COSMO Priority Projects, introduced and started at the Zurich meeting in 2005, will be published as COSMO Technical Reports within the next few weeks. This partly explains why this years Newsletter is comparatively thin, since a lot of last years COSMO work has taken place within the Priority Projects, and will hence be reported on in the upcoming COSMO Technical Reports rather than in this Newsletter.

For those of you who would like to participate at a COSMO General Meeting, rather than 'only' reading the Newsletters: the next General Meeting will take place from 7 to 11 September 2009 at the DWD in Offenbach, Germany!

Marco Arpagaus
COSMO Scientific Project Manager

Figure 1: Participants of the 10th COSMO General Meeting in Cracow

Developments at DWD: Integrated water vapour (IWV) from ground-based GPS

Christoph Schraff, Maria Tomassini, and Klaus Stephan

Deutscher Wetterdienst, Frankfurter Strasse 135, 63067 Offenbach, Germany

1 Introduction

Detailed analysis used for very short-range numerical weather prediction (NWP) requires observational information of good quality and with high spatial and temporal resolution. Sampling tropospheric humidity by radiosondes or by meteorological satellite systems is often not sufficient for this purpose.

The delay of radio signals from several GPS satellites to a GPS receiver at the ground can be processed to derive the integrated water vapour (IWV) in the atmospheric column above the station with good accuracy, provided that the pressure and temperature at the GPS station are also known (Bevis et al., 1994). In 2001 and 2002, DWD has tested the assimilation of hourly or half-hourly data from some 100 GPS Stations in Germany processed by the GeoForschungsZentrum Potsdam (GFZ, see Reigber et al., 2002; Gendt et al., 2004) into the then operational configuration of the COSMO model (formerly Lokal Modell LM) which had a mesh width of 7 km (Tomassini, 2003; Tomassini and Schraff, 2002).

Since then, GFZ has further increased the number of stations and enhanced the data frequency to one every 15 minutes. In the current contribution, the assimilation of these GPS data is tested for the first time with the convection-permitting configuration COSMO-DE.

2 Nudging of integrated water vapour and experimental set-up

The data assimilation scheme of the COSMO-Model is based on nudging towards observations (see Schraff and Hess, 2003). This technique can make full use of high-frequent data such as the GPS data considered here. However, the observation increments have to be expressed (nearly) in terms of the model state variables. Since specific humidity rather than IWV is the state variable for water vapour, the observational information on IWV has to be conveyed into information on specific humidity. For this purpose, a 'pseudo-observed' profile of specific humidity is retrieved by scaling iteratively the model humidity profile with the ratio of observed to modelled IWV. (The iteration may be necessary to avoid over-saturation, and the IWV ratio takes into account the (mostly very small) differences between station height and model orography.)

The retrieved humidity profile can then be nudged in a similar way as a radiosonde humidity profile. However, an additional quality weight ≤ 1 and proportional to the specific humidity at saturation and to the thickness of the model layer is assigned to the humidity retrieval at each model level. In this way, the GPS humidity profile is given larger weight at those levels which can give a larger contribution to the integrated value IWV, normally between 700 hPa and 800 hpa, and less at other levels. Furthermore, the horizontal radius of influence is reduced from about 120 km valid for radiosondes to about 50 km, which appears to be adequate for the dense GPS network.

169 GPS stations, most of them in Germany, have been selected for assimilation after a monitoring period. Generally, the GPS-derived IWV has been found to verify well with the humidity from the Vaisala Radiosondes RS92, except for the well-known 12-UTC (midday) dry bias of the RS92 version that was widely used in summer 2007. The assimilation period from 1 to 13 June 2007 was characterised by weakly anticyclonic air-mass convection. 21-hour forecasts were started daily at 0, 6, 12, and 18 UTC from the assimilation cycle with the COSMO-DE configuration, i.e. using a mesh width of 2.8 km . 3 experiments are compared:

- CNT: operational set-up, including latent heat nudging for the assimilation of radar-derived surface precipitation rate
- GPS: like CNT, but with additional assimilation of the GPS-derived IWV data
- NoRSq: like CNT, but without nudging of radiosonde humidity

Note that in NoRSq, the humidity runs nearly freely in the inner model domain since the direct influence of the only used humidity observations, that is from surface mesonet stations, is limited to the lowest model layer which has a thickness of 20 m only. Some additional influence from radiosonde humidity comes through the lateral boundaries.

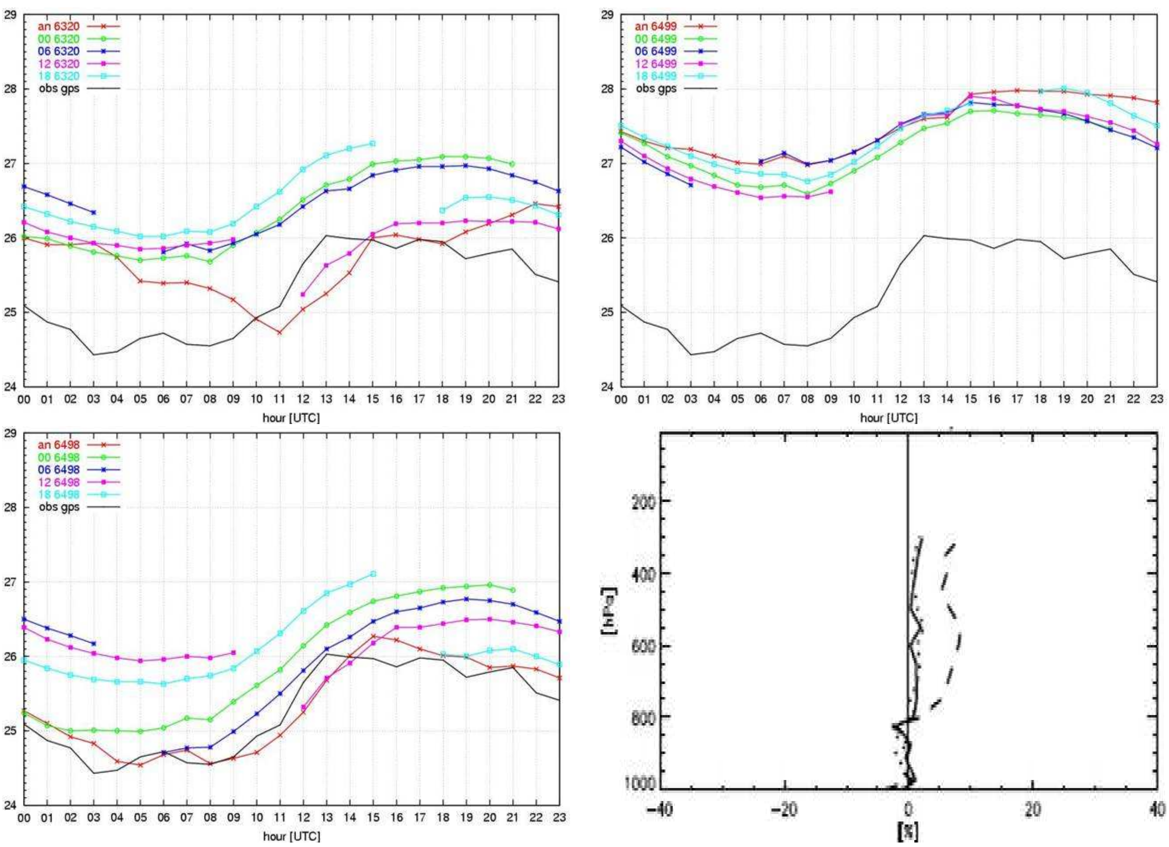

Figure 1: Integrated water vapour IWV in kg m^{-2} averaged over the 169 GPS observation locations as a function of daytime (UTC) for the period of 1 - 13 June 2007. Black line: GPS observations; red: COSMO-DE assimilation cycle; green: 00-UTC forecast runs; blue: 06-UTC forecast runs; purple: 12-UTC forecast runs; cyan: 18-UTC forecast runs. Upper left panel: CNT; upper right: NoRSq (i.e. without use of radiosonde humidity data); lower left: GPS experiment. Lower right panel: Vertical profile of bias (model - radiosonde observations) of relative humidity for the same period. Solid: CNT; dashed: NoRSq; dotted: GPS.

3 Case Study

Since experiment NoRSq is only very weakly affected by humidity observations, its mean IWV content should reflect well the model climate of the water cycle. The 'model climate' shall denote here simply the mean model state reached after running the model freely for a long time without any influence from observations. It is the model-internal equilibrium which depends on all the (physical and numerical) processes simulated by the model. Figure 1 shows that while the daily variation of IWV in NoRSq matches the GPS observations well, the mean IWV is overestimated both in the assimilation cycle and in all forecasts by about 2 $\mathrm{kg\,m^{-2}}$. Thus, the model has to build up too large an amount of moisture in the atmosphere until evaporation and precipitation become equilibrated. It appears that the processes which decrease the moisture content, typically by precipitation, are not effective enough in COSMO-DE. It is interesting to note that the excess of moisture in the model climate takes place above rather than within the planetary boundary layer (see lower right panel of Figure 1).

With the assimilation of the radiosonde humidity data in CNT, the bias in IWV is at least halved in the assimilation cycle. It even becomes negative at noon and in the early afternoon as a result of the above-mentioned dry bias of the Vaisala RS92 sondes used in 2007. The remaining bias of 1 $\mathrm{kg\,m^{-2}}$ at 0 UTC indicates that the assimilation of the radiosonde data is not effective enough to completely eliminate the model's wet bias in the whole region covered by the GPS stations although there is nearly no wet bias against the radiosondes themselves

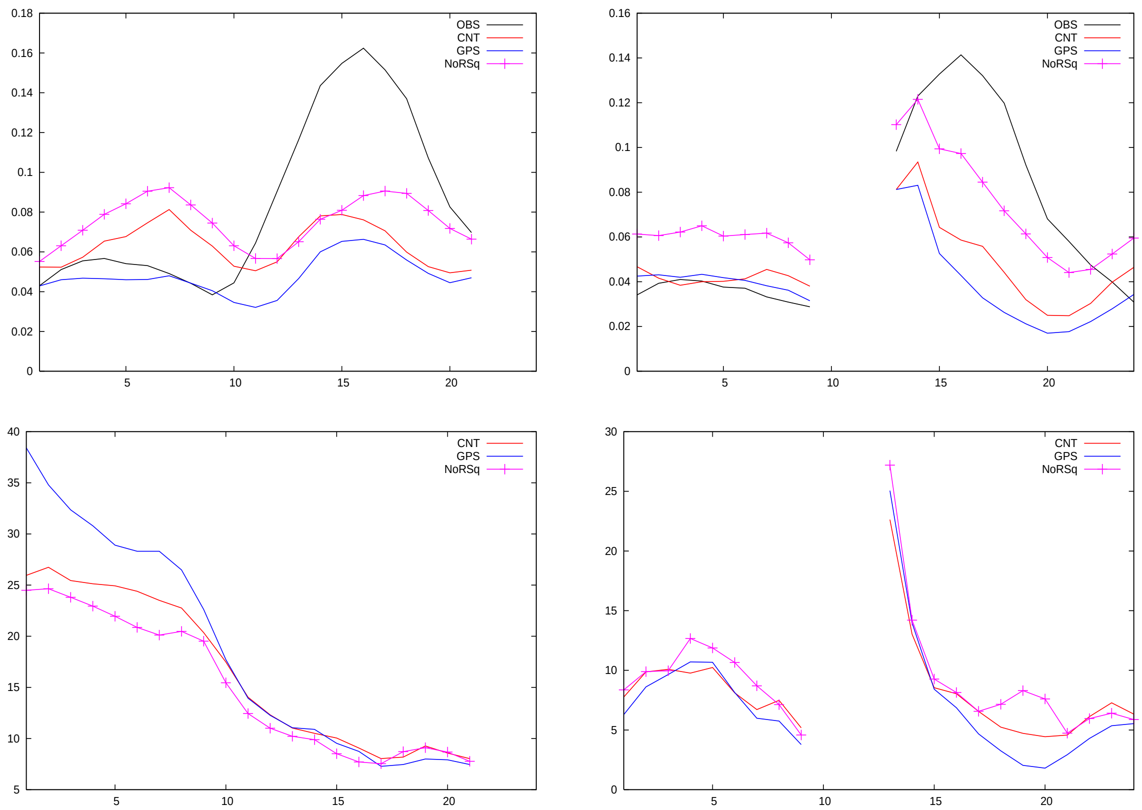

Figure 2: Upper left panel: hourly precipitation amounts greater than 0.1 mm/h from COSMO-DE 00-UTC forecast runs averaged over the radar domain as a function of daytime (UTC) for the period of 31 May to 13 June 2007. Lower left: as upper left, but Equitable Threat Score (ETS) of hourly precipitation against radar data for a threshold of 0.1 mm/h. Right panels: as left panels, but for 12-UTC forecast runs and a threshold of 1.0 mm/h. Black solid line: radar-derived precipitation; red solid: CNT; blue solid: GPS; purple crosses: NoRSq.

(see lower right panel of Figure 1 for relative humidity – the temperature bias (not shown) is also close to zero). In agreement with the assimilation cycle, the 12-UTC forecast runs start with a dry bias but moisten rapidly towards the model's wet-biased internal equilibrium. The other forecasts start already with a wet bias which increases moderately during the forecasts but remains smaller than in NoRSq.

With the assmilation of GPS-derived IWV, the bias against the GPS data disappears during the assimilation cycle and at the beginning of the forecasts. In all the forecasts of experiment GPS, a wet bias then develops and increases towards the model climate, attaining similar values as in CNT.

The model bias in atmospheric water vapour is closely related to biases in surface precipitation (see Figure 2). In comparison to the radar-derived precipitation which has a very pronounced peak in the afternoon, NoRSq strongly overestimates both weak and strong precipitation in the night and early morning and strongly underestimates it throughout the afternoon. The assimilation of radiosonde humidity in CNT reduces precipitation in the 0-UTC forecast runs moderately. In the 12-UTC forecast runs, however, the reduction is large throughout the forecast period and eliminates the positive bias at night. When the GPS data are additionally assimilated, the positive bias in the night and morning is eliminated and close to zero both for 0- and 12-UTC runs. On the other hand, the negative bias in the afternoon is further enhanced.

In terms of equitable threat scores (ETS) against radar-derived precipitation (lower panels of Figure 2), the assimilation of the GPS data has a large positive impact in the first 9 hours of the 0-UTC runs for low thresholds (which reflect areas of precipitation). In contrast, there is a clear negative impact on the 12-UTC runs during the late afternoon, particularly for strong precipitation (e.g. 1.0 mm/h threshold). The ETS score is a quality measure and should indicate mainly how well the patterns match. However, it is not independent from the bias. Past experience with many experiments has shown that it correlates positively with the frequency bias (FBI) not only for FBI values less than 1 (negative bias) but up to values of about 2. This suggests that the use of the GPS data has indeed improved the geographical location of precipitation in the 0-UTC forecast runs while it is unclear whether and to what extent the decrease of the ETS in the 12-UTC runs is an effect of the enhanced negative bias.

4 Concluding Remarks

This study illustrates that the GPS data are very useful for verification of the daily cycle of humidity in the model. It is revealed that the model-internal equilibrium (or 'model climate') of COSMO-DE has a strong overall positive water vapour bias in summer. With the assimilation of GPS-derived IWV, this bias is greatly reduced in the assimilation and early in the forecast. Also, the mean precipitation amounts are reduced throughout the forecast range. Since the diurnal cycle of convection is far too weak in the model, both positive and negative impacts on biases and verification scores result. Maybe apart from the consistent benefit in the 0-UTC forecast runs during the first 9 hours, the impact of the GPS data appears to be dominated by effects of model biases. For instance, this is likely true for the enhanced tendency to suppress strong precipitation in the afternoon.

The above experiments have been performed with a model version that was operational at DWD before September 2008. Then, DWD operationally introduced a modification in the subgrid-scale cloud scheme and a reduction of the upper limit for the turbulent mixing length (Seifert et al., 2008). Tests have shown, that the new version of COSMO-DE reduces the underestimation of the diurnal cycle of convective precipitation and also improves the bias and ETS of the 0-UTC runs during the first about 9 hours. It is expected that this will influence the impact of the GPS data. Therefore, similar experiments and evaluations as done in this study should be repeated with the new model version to assess the impact of nudging GPS data into a convection-permitting model when the biases are not so large. Further experiments should also be done for winter periods, including low stratus cases.

References

Bevis, M, S. Businger, S. Chiswell, T. A. Herring, R. A. Anthes, C. Rocken, and R. H. Ware, 1994: GPS Meteorology: Mapping zenith wet delay onto precipitable water. *J. Appl. Meteor.*, 33, 379-386.

Gendt, G., G. Dick, C. Reigber, M. Tomassini, Y. Liu, and M. Ramatschi, 2004: Near real-time GPS water vapour monitoring for numerical weather prediction in Germany. *J. Met. Soc. Japan*, 82, 361-370.

Reigber, C., G. Gendt, G. Dick, and M. Tomassini, 2002: Near real-time water vapour monitoring for weather forecast. *GPS World*, 13, 18-27.

Schraff, C., and R. Hess, 2003: A description of the nonhydrostatic regional model LM. Model Documentation Part III: Data assimilation. Available at:
http://www.cosmo-model.org/content/model/documentation/core/cosmoAssim.pdf

Seifert, A., M. Baldauf, K. Stephan, U. Blahak, and K. Beheng, 2008: The challenge of convective-scale quantitative precipiation forecasting. *Proc. 15th Int. Conf. Clouds and Precip., Cancun, Mexico, 7 - 11 July 2008,* http://convention-center.net/iccp2008/abstracts

Tomassini, M., 2003: Assimilation of integrated water vapour from ground-based GPS in the limited area model of DWD. *ECMWF/GEWEX Workshop on humidity analysis, 8 - 11 July 2002,* 107-116.

Tomassini, M., and C. Schraff, 2002: Assimilation of GPS data in August 2002. *COSMO Newsletter No. 3*, 158-163.

Improvements of the operational latent heat nudging scheme used in COSMO-DE at DWD

Klaus Stephan and Christoph Schraff

Deutscher Wetterdienst, Frankfurter Strasse 135, 63067 Offenbach, Germany

1 Introduction

Since April 2007 the convection permitting model COSMO-DE (Baldauf et al., 2007) runs operationally. Its main purposes is the prediction of severe weather events related to deep moist convection and to interactions of the flow with small scale topography. To satisfy this goal the initial conditions include small scale precipitation information obtained from radar measurements beside the large scale structures obtained from conventional data. The radar measurements are assimilated by applying the latent heat nudging (LHN) approach. Herein an assumed relation between precipitation formation and latent heat release is used to change the model dynamics in such a way that the model will respond by producing a rain rate close to the observed one. At every model grid point the model is compared to the radar measurement. If the two are different, the vertical profile of modelled latent heat release at that grid point is scaled according to the ratio between observed and modelled precipitation rate. The original LHN technique proposed by Jones and Macpherson (1997) had to be adapted for COSMO-DE because the latter uses a prognostic precipitation scheme (Klink et al., 2006; Stephan et al., 2008). The adapted LHN scheme applied in COSMO-DE deploys a reference precipitation rate for comparison with the observed precipitation rate. This mitigates the spatial and temporal decorrelation of precipitation and latent heat release, caused by treating precipitation as prognostic variable. This improves the performance of LHN unless the used reference is globally biased to the surface precipitation.

Recent changes within the microphysical parameterisation of COSMO model, which improved the quality of the precipitation forcast of COSMO-DE (and of the coarser-resolution COSMO-EU), resulted in a bias between reference and modelled surface precipitation. The changes modified the formation of precipitation and included a reduction of evaporation and a more comprehensive parameterisation of the snow formation. This had an impact on LHN, and the model overestimated the surface precipitation during assimilation significantly. Furthermore it confirmed, that the LHN is strongly dependent on the microphysics. Especially the formulation of the grid point search algorithm within the LHN was found to be very sensitive to the changes in the microphysics. Therefore, two modifications of the operational LHN scheme will be discussed in the following:

- revised definition of the reference precipitation to correct its bias against surface precipitation,
- improvement of the LHN-internal grid point search algorithm.

2 Improvement of the LHN scheme

2.1 Correction of the bias between reference and surface precipitation

Since COSMO-DE treats precipitation as a prognostic variable the original LHN scheme had to be adapted so as to cope with the drifting of precipitation (Stephan et al. 2008). A major challenge was to reduce the decorrelation of the latent heat release and surface precipitation. This is mainly caused by the temporal delay of the precipitation reaching the ground relative to the time of condensation and precipitation formation. One adaptation of the LHN scheme has been to introduce a reference precipitation, which should be closer in time to the process of precipitation formation. It is compared with the observed precipitation and defined as

$$R_{Ref} = \frac{1}{z(k_{top}) - z(k_0)} \int_{k_0}^{k_{top}} \left[\sum_i \{\rho(z) q_i(z) \nu_i\} \right] dk \qquad (1)$$

where q_i is the mass fraction and v_i the sedimentation velocity of precipitate i (rain, snow, or graupel). The fluxes of the different precipitation constituents are integrated vertically starting from a certain layer k_{top} down to the ground (k_0). Herein k_{top} is a free parameter, which is not predetermined by a physical constraint. It determines the number of layers which are considered for the average. Therefore the amount of the reference precipitation depends on the parameter k_{top}. k_{top} was defined as the uppermost layer in which the precipitation flux exceeds 0.1 mm/h. This seemed plausible because this value is used as a general threshold within LHN, below which no LHN is performed in order to introduce precipitation. With this definition of k_{top} and for the former parameter setting of the microphysics the resulting reference was nearly unbiased to the surface precipitation. However, the changes within the microphysics and especially the reduction of evaporation of the precipitation beneath clouds have caused a significant bias. The surface precipitation is enhanced, whereas the reference precipitation is nearly unchanged.

One opportunity to reduce the bias is changing the definition of k_{top}. The new definition sets k_{top} at the uppermost layer in which the precipitation flux exceeds a certain ratio α of the maximum of the precipitation flux within the column. Then, α determines the height of the column used for the vertical average. A value 0.4 for α has been evaluated to be optimal with respect to both the mentioned bias as well as the overall performance of LHN. Figure 1 illustrates the correction of the bias. It shows that the surface precipitation in the operational analysis was much higher than the reference precipitation, especially for higher precipitation amounts. The new definition of the reference precipitation reduced this positive bias to the extent that, in fact, a slight overestimation of the reference precipitation against the surface precipitation occurs. As a result when using the new reference precipitation for

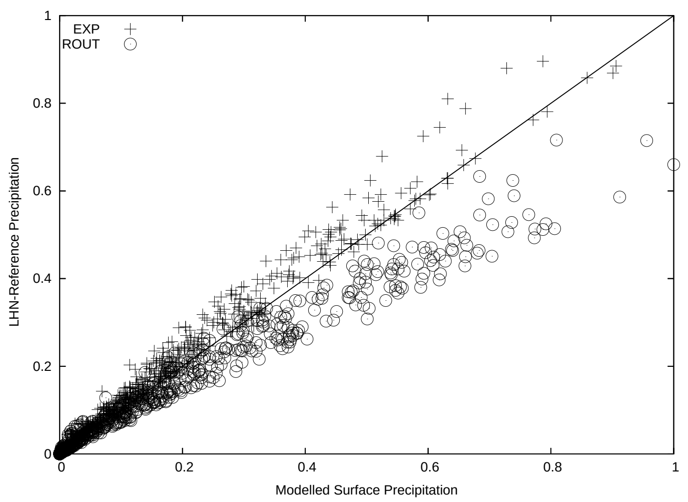

Figure 1: Scatter plot of reference precipitation against surface precipitation for spatially averaged hourly precipitation in August 2007. The circles indicate the values obtained from the operational analyses and the plus signs the values for the experimental analyses with the revised definition for the reference precipitation.

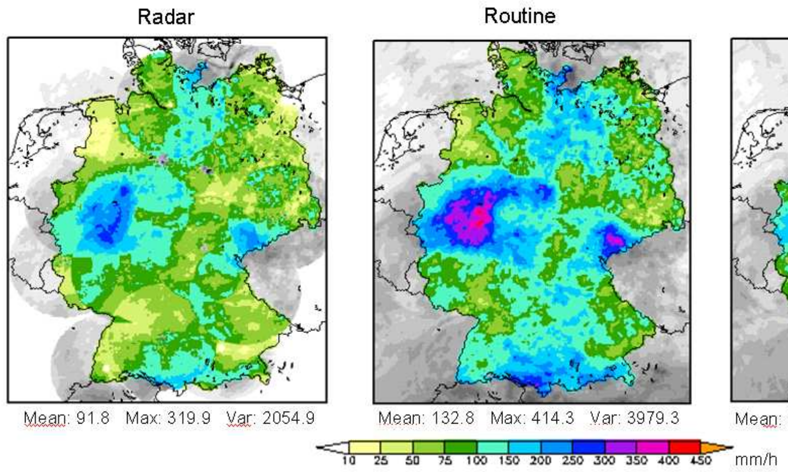

Figure 2: Monthly precipitation of August 2007: radar observastion (left), operational analysis (middle), experimental analysis with the revised definition of the reference precipitation (right)

the assimilation of August 2007 the overestimation of surface precipitation against radar observations was reduced (see Figure 2). The impact on the free forecast is slightly positive.

2.2 Improvement of the LHN-internal grid point search algorithm

While the above mentioned modification is important in general, the second modification concerns cases in which the model produces far too little precipitation compared to the observation. Then the latent heating profile at this grid point is not likely representative for conditions as indicated by the observed precipitation.

In such a case, a 'suitable' nearby grid point is searched (within a search radius of 10 grid points). The scaled heating profile from that grid point is then defined to be the profile of LHN temperature increments at the target grid point. (If no point is found, a climatological profile will be scaled and used.) The suitable nearby grid point had to satisfy two criteria. Firstly, it should be representative of the real conditions at the target grid point. The only direct indication of these conditions comes from the radar observation. Therefore, it was required that the reference precipitation at the selected grid point had to be close to the observed value at the target point. With the prognostic treating of precipitation in the model this however does not imply that the latent heat release is large enough to allow for reasonable LHN increments. Near-zero latent heating occurs for instance at precipitating grid points at the upstream edge of precipitation cells where cloud formation is almost finished. Therefore, a second criterion was defined which required that the vertical integral of modelled latent heat release had to be larger at the suitable nearby grid point than at the target grid point.

The above-mentioned changes of the microphysics have significantly increased the variability of the local ratio between precipitation rate and latent heating. In some cases, the latent heating could become very large at grid points which met both criteria and were selected by the grid point search algorithm. The resulting excessively large LHN increments then caused strong gravity waves related to small-scale, mostly positive strong pressure anomalies and excessive precipitation. This is illustrated in Figure 3 for a frontal case. To avoid that, the second criterion has been revised as follows. At a suitable grid point, the ratio between the

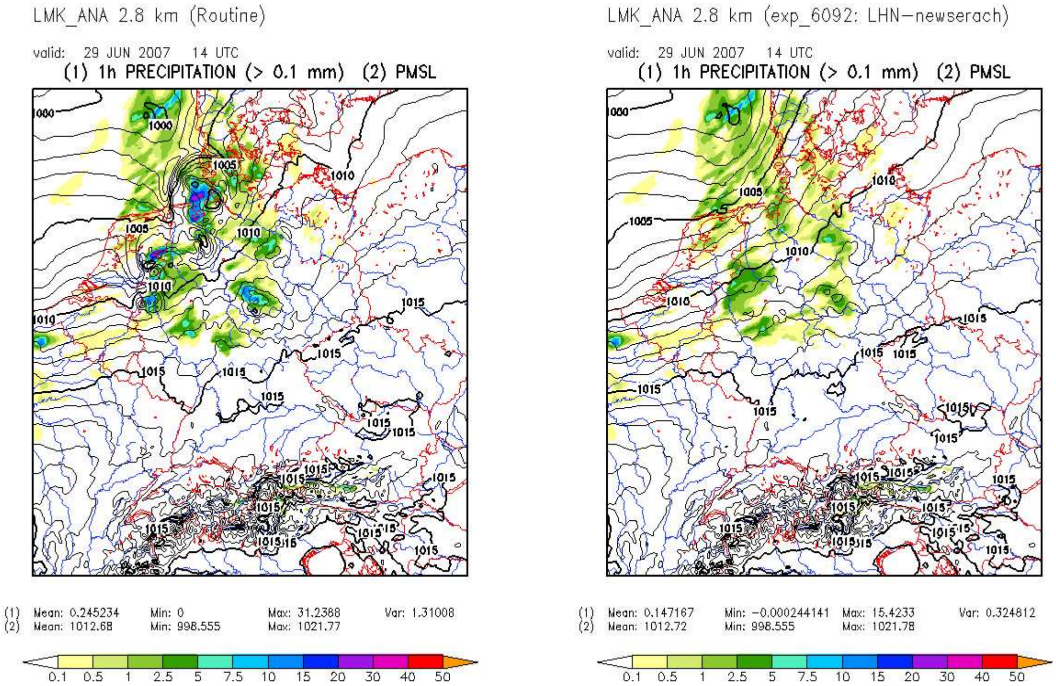

Figure 3: Analysis of surface pressure (contours) and hourly precipitation (colors) for 29. June 2007 14 UTC obtained from COSMO-DE assimilation. Left: operational analysis, Right: experimental analysis with the revised grid point search

precipitation rate and the integral of latent heat release must not exceed ± 50% of the ratio of the model's climate (as obtained from long-term averaging). The result of this improvement is shown in the right panel of Figure 3 for the considered case. The pressure anomaly vanishes and the precipitation pattern responds quite well to the observations. The modification also improves the 24-hour precipitation sum as shown in Figure 4.

The positive impact of both modifications found during the assimilation cycle disappears quickly in the free forecast. This is revealed by a verification against radar observations.

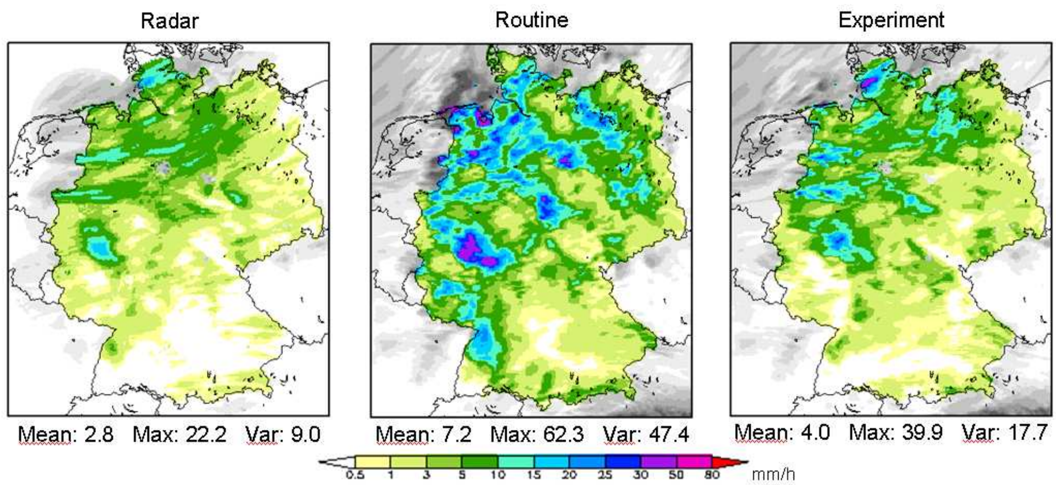

Figure 4: 24h precipitation of 29. June 2007: radar observastion (right), operational analysis (middle), experimental analysis with revised grid point search (left)

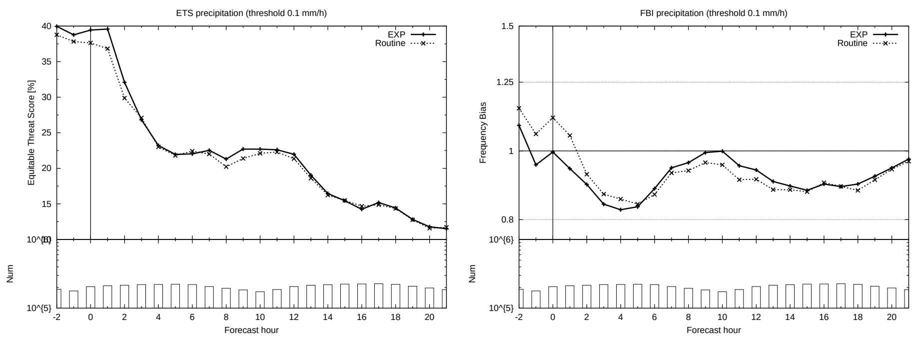

Figure 5: Verification of modelled hourly precipitation greater than 0.1 mm/h against radar observations for 34 forecasts in August 2006 for the last two hours of assimilation and the consegutive forecast (21 hours), left: ETS and right: FBI. The dashed line depicts the scores for the operational setup and the solid line for the experimental setup with revised grid point search and definition of the reference precipitation. The bars at the botton indicate the number of radar observations.

Figure 5 shows equitable threat scores (ETS) and frequency biases (FBI) for the last hours of assimilation and 34 consecutive forecasts over 21 hours. The modifications improve the ETS and FBI during the assimilation, but the positive effect almost vanishes after about three hours of free forecast.

3 Conclusions

The improved grid point search and definition of the reference precipitation in the latent heat nudging provide a better match of the initial state of COSMO-DE to the precipitation patterns derived by radar observations. Both improvements reduce the overestimation of surface precipitation during the assimilation. Especially the overestimation of higher precipitation amounts (greater than 5 mm/h) could be greatly reduced. However, the positive impact during the assimilation reduces very rapidly in the free forecast.

It can be assumed that the better agreement of the precipitation patterns in the analysis with real measurements should gradually improve the distribution of modelled soil moisture. As soil moisture is a sensitive parameter for the simulation of moisture fluxes into the atmosphere, an improvement of the free forecast might occur after a longer period than inverstigated in the present study.

References

Baldauf M., K. Stephan, S. Klink, C. Schraff, A. Seifert, J. Forstner, T. Reinhardt, C.-J. Lenz, 2007: The new very short range forecast model COSMO-LMK for the convection-resolving scale. *WGNE Blue Book* **2007** Sect. 5 1–2

Jones, C. D., B. Macpherson, 1997: A Latent Heat Nudging Scheme for the Assimilation of Precipitation Data into an Operational Mesoscale Model. –*Meteorol.Appl.* **4**, 269–277

Klink, S., K. Stephan, C. Schraff, 2006: Assimilation of Radar Data in the Mesoscale NWP-Model of DWD. *WGNE Blue Book* **2006** Sect. 1 15–16

Stephan K., S. Klink, C. Schraff, 2008: Assimilation of radar derived rain rates into the convective scale model COSMO-DE at DWD. *Q.J.R.Meteorol.Soc.* **134**, 1315-1326

Screen-level data assimilation in COSMO-I2

Massimo Milelli, Elena Oberto, Marco Turco

ARPA Piemonte, Via Pio VII 9, I-10135 Torino, Italy

1 Introduction

A mesoscale four-dimensional data assimilation (hereafter FDDA) and very short-term forecasting system has been developed and tested. The assimilation method is based on the Newtonian relaxation technique where model solutions are nudged towards individual observations (see Stauffer and Seaman, 1990, or Stauffer and Seaman, 1994). The system tested here is based on the COSMO-I7 operational run to provide boundary and initial conditions (hereafter ICs and BCs respectively) to the COSMO-I2 model, which is run with operational namelists with the exception of the domain (see Fig. 1) and some modifications in INPUT_ASS (see Tab. 1). Then a set of different assimilation/forecast (12h assimilation and 24h forecast) cycles is conducted by varying the assimilated data. The aim of the work is to investigate the assimilation of the non-GTS data from the ARPA Piemonte high-resolution network in order to create an operational very high-resolution analysis. Moreover, it is important to test the option of running in the future a very short-range forecast (6h to 12h) starting from these analysis.

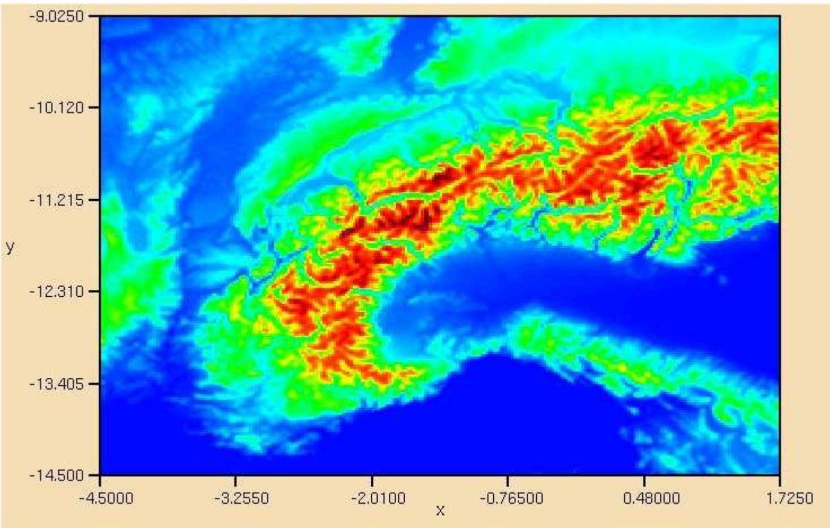

Figure 1: Domain of the simulations

2 Method

The ARPA Piemonte network of non-GTS stations (see Fig. 2) includes more than 500 stations and each set of gauges (W10m, Slp, T2m, Rh2m) has been subdivided into two homogeneously distributed groups (see Figs. 3 to 6): one of them is included into the assimilation cycle, the other one is used for verification. In this way we can perform an

parameter name	default	new value
altopsu	100, 5000, 5000, 5000	700, 700, 700, 700
doromx	100, 400, 160, 160	100, 100, 100, 100
gnudgsu	0.0006, 0.0012, 0, 0.0006	0.0006, 0.0006, 0.0006, 0.0006
rhiflsu	70, 70, 100, 70	40, 46, 22, 30

Table 1: parameters changed in INPUT_ASS.

independent validation of the results. The assimilated data belong to stations below 700 m, as evident from the namelist parameter *altopsu* in Tab. 1. The new values of *gnudgsu* and *rhiflsu* derive by purely empirical reasons, without any tuning study.

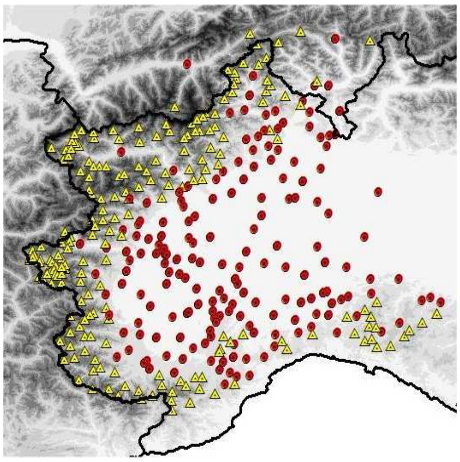

Figure 2: Piemonte high resolution stations distribution. The red dotes indicate stations below 700 m, the yellow triangles above

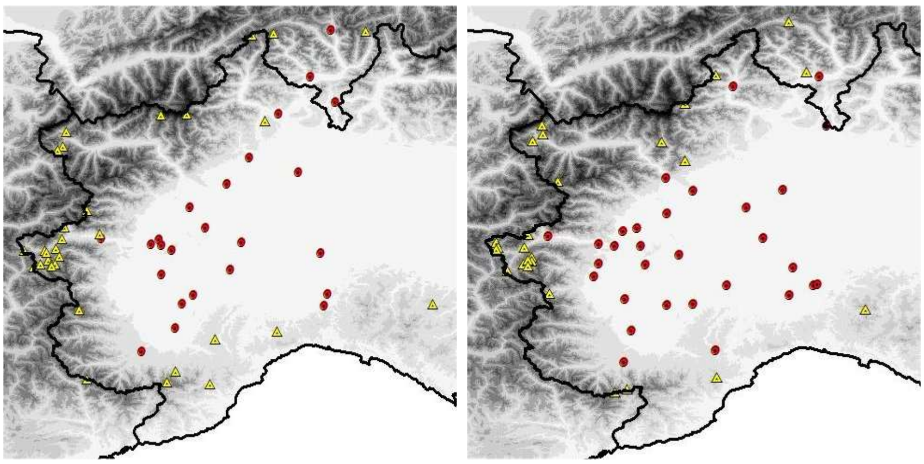

Figure 3: Piemonte high resolution distribution for wind velocity and direction sensors: assimilated into the model (left) and used for verification (right). The red dotes indicate stations below 700 m, the yellow triangles above

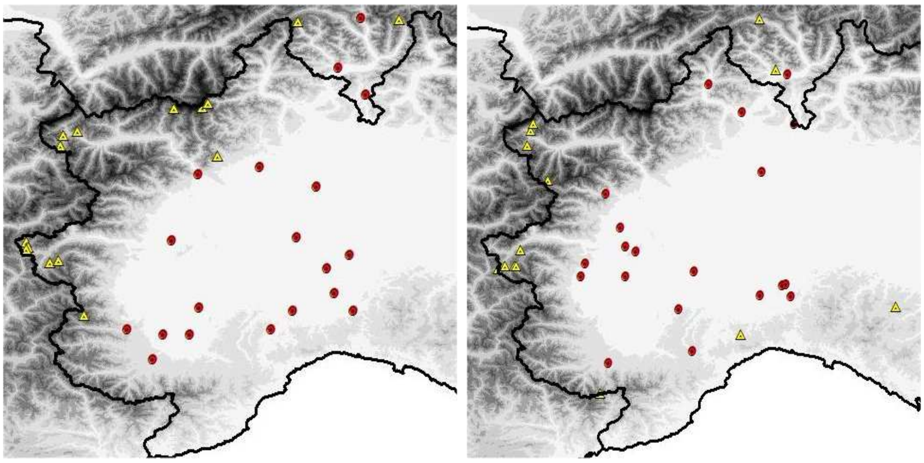

Figure 4: Piemonte high resolution distribution for surface pressure sensors: assimilated into the model (left) and used for verification (right). The red dotes indicate stations below 700 m, the yellow triangles above

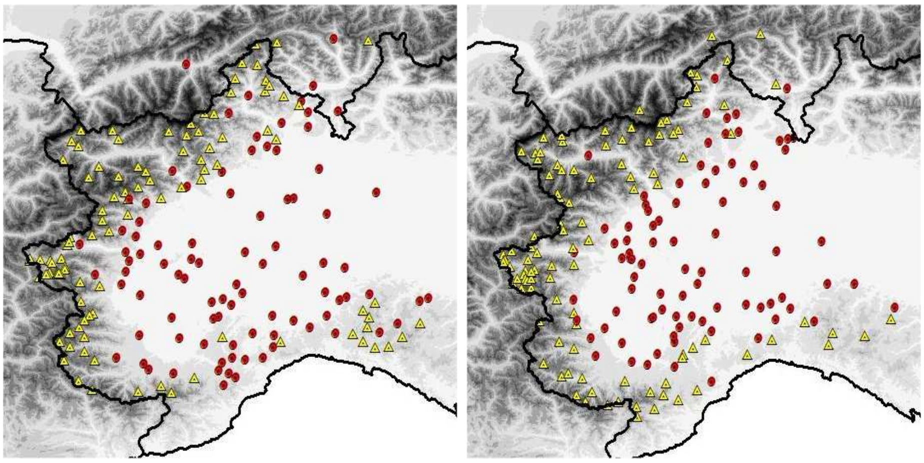

Figure 5: Piemonte high resolution distribution for temperature sensors: assimilated into the model (left) and used for verification (right). The red dotes indicate stations below 700 m, the yellow triangles above

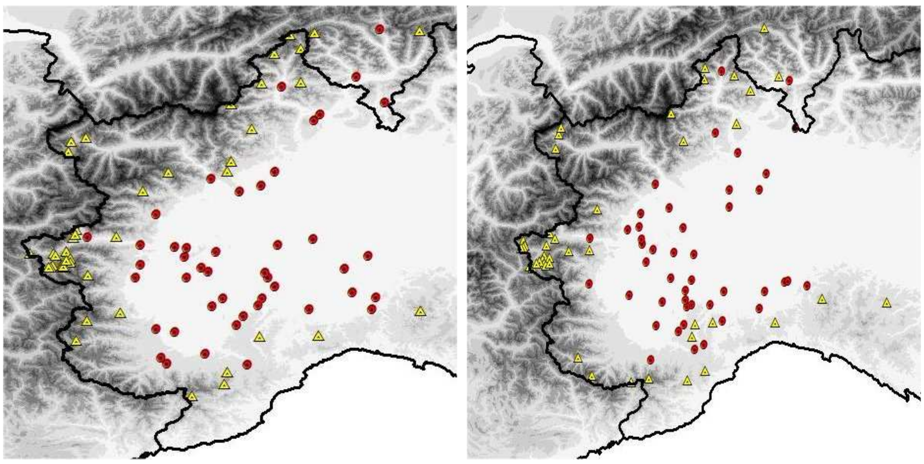

Figure 6: Piemonte high resolution distribution for relative humidity sensors: assimilated into the model (left) and used for verification (right). The red dotes indicate stations below 700 m, the yellow triangles above

Simulation name	Assimilated parameter	Simulation name	Assimilated parameter
Sim. 0	no assimilation (ctrl)	Sim. 8	Slp + T2m
Sim. 1	W10m	Sim. 9	Slp + Rh2m
Sim. 2	Slp	Sim. 10	T2m + Rh2m
Sim. 3	T2m	Sim. 11	W10m + Slp + T2m
Sim. 4	Rh2m	Sim. 12	W10m + Slp + Rh2m
Sim. 5	W10m + Slp	Sim. 13	W10m + T2m + Rh2m
Sim. 6	W10m + T2m	Sim. 14	Slp + T2m + Rh2m
Sim. 7	W10m + Rh2m	Sim. 15	W10m + Slp + T2m + Rh2m

Table 2: scheme of the performed simulations.

Three different test cases have been run for 36h (12h of assimilation and 24h of forecast):

- 20060817 starting at 00UTC: super cell with underestimation and slightly wrong localization (COSMO PPQPF test case);
- 20070501 starting at 12UTC: thunderstorms not correctly localized;
- 20080217 starting at 00UTC: stratiform clouds not correctly forecasted.

A number of simulations have been run for each test case, using all the possible combinations for the assimilation of the four parameters, according to Tab. 2.

There are two possible ways of verification:

- verification against observation, in order to observe the behavior of the direct model output;
- verification against the control run, in order to observe the contribution of a single modification to the model, more suitable for sensitivity studies like this one. In particular we followed the approach of Stein and Alpert, 1993 called Factor Separation Method.

3 Results

In the following, we show only a selection of results which are representative of all the simulations and permit to draw some general conclusion. In particular, we focus on the 20070501 test case. Moreover, we point the attention on the simulations 0 to 4, from which it is possible to derive some coherent behavior of the model. In the other simulations (Sim. 5 to 15), the results are honestly fuzzy and difficult to interpret, since each test case behaves in a different with respect to the parameter and to the forecast time, i.e. in the assimilation cycle or in the free forecast. In Tab. 3 the actual distribution of stations between assimilation and verification is shown.

A general comment, looking at Fig. 7 and Fig. 8, is that after $\approx$ 20h of simulation, the runs tend to overlap: the effect of the nudging vanishes as expected, but there is also a possible influence from the BCs since the boundaries are probably too close to the area of interest and rapidly dominate the inner domain. More in detail:

- the RMSE plots in Fig. 7 show a certain insensitivity of the pressure to any change, while the other variables are indeed influenced. In particular the major impact (positive) comes from the temperature assimilation (Sim. 3), while the pressure assimilation

	aof		ver	
	h ≤ 700 m	h > 700 m	h ≤ 700 m	h > 700 m
W10m	24	32	30	26
Slp	19	15	20	14
T2m	86	107	86	107
Rh2m	45	44	45	44

Table 3: Number of stations in the assimilation file (aof) and in the verification file (ver), according to the parameter and the height.

(Sim. 2) deteriorates Rh2m and W10m, but still improves T2m. The assimilation of Rh2m (Sim. 4) determines only a worsening of Rh2m itself and Sim. 1 (wind assimilation) is basically neutral for the four variables;

- the ME plots in Fig. 8 show a constantly positive bias for T2m and negative for Rh2m. W10m has a positive bias almost always, except for the first hours of Sim. 3. Finally Slp has a slightly negative bias which turns to be slightly positive in Sim. 2 and 3.

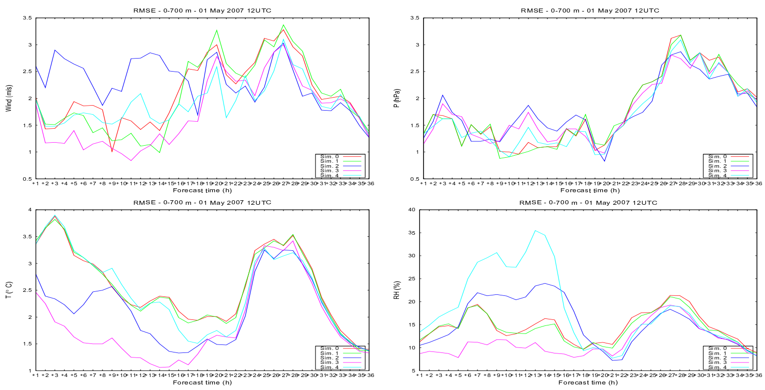

Figure 7: 20070501 12UTC test case; Root Mean Square Error of simulations 0, 1, 2, 3, 4 from +1h to +36h for wind (top left), surface pressure (top right), temperature (bottom left) and relative humidity (bottom right) respectively

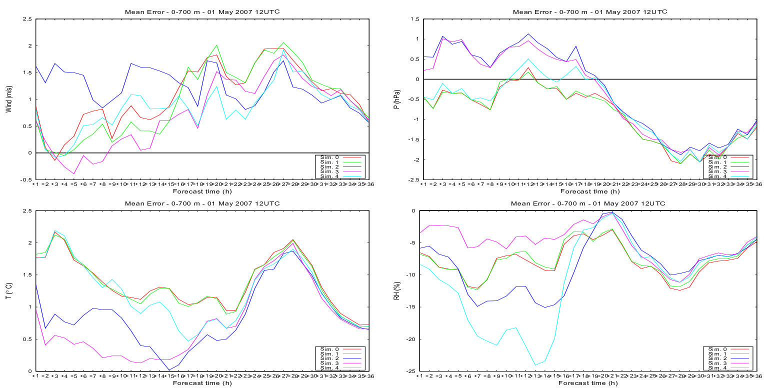

Figure 8: 20070501 12UTC test case; Mean Error of simulations 0, 1, 2, 3, 4 from +1h to +36h for wind (top left), surface pressure (top right), temperature (bottom left) and relative humidity (bottom right) respectively

The vertical profiles of temperature observed and forecasted at CUNEO GTS station in Fig. 9 show an unexpected general improvement. The left panel shows the profiles at the end

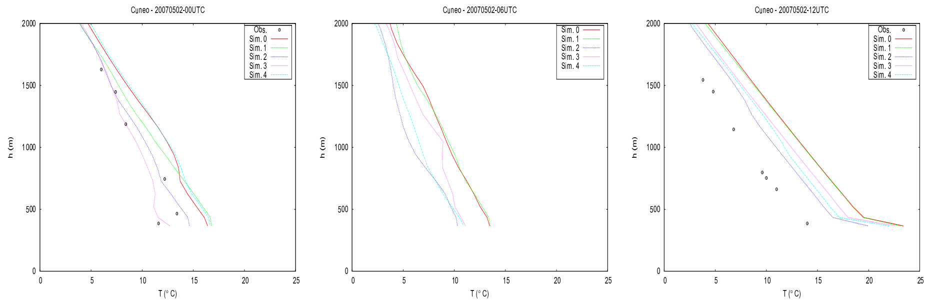

Figure 9: 20070501 12UTC test case; vertical profiles of temperature in Cuneo for simulations 0, 1, 2, 3, 4 at +12h (left), +18h (centre) and +24h (right) respectively. At +18h there is no observation

of the 12h assimilation cycle and it can be seen that Sim. 2 and Sim. 3 are much closer to observation than Sim. 0 (Ctrl). In the central panel, despite the lack of observation, there is still an influence from the nudging and this is confirmed also at +24h (right panel), 12h after the end of the assimilation cycle. The result is noticeable because it shows that fine-adjusted surface data assimilation does not destroy the vertical profile as observed by Stauffer and Seaman with a coarser resolution (Stauffer and Seaman, 1990), but indeed improves it slightly. In general the results tend to differ only below $\approx$ 2000 m. A reason could be the density of observations in the neighborhood of the Cuneo airport which is in fact surrounded by a large number of stations (also at high altitude) and this influences the model PBL also if we are only assimilating screen-level data.

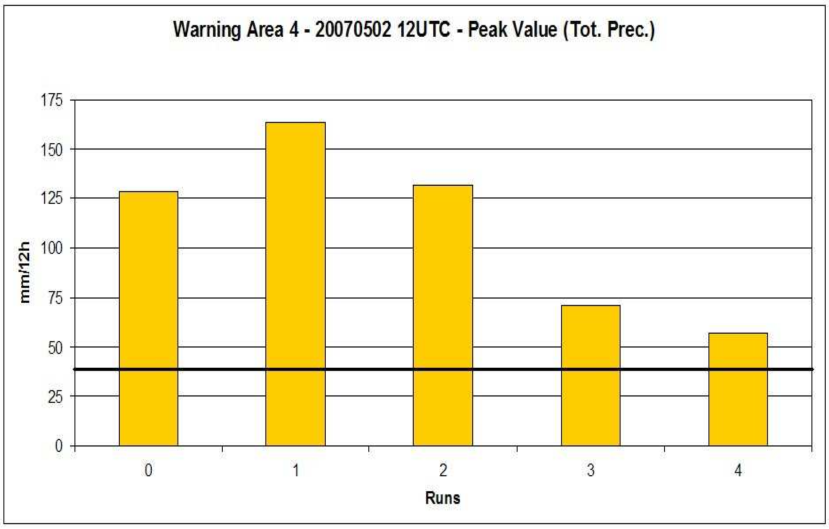

Figure 10: 20070501 12UTC test case; peak of precipitation in the warning area 4 from +12h to +24h for simulations 0, 1, 2, 3, 4. The black line is the observed value

Finally, considering the precipitation, we plot in Fig. 10 (as an example) the peak values over the warning area no. 4 of the regional alerting system from +12 to +24h, after the assimilation cycle. In that case, we had a false alarm since the forecasted precipitation over the area was largely overestimated (the observed peak was around 40 mm/12h). It can be seen that with Sim. 3 and 4 there is a considerable reduction of the precipitation (40 to 50 % reduction with respect to Sim. 0). It is important to highlight that the precipitation is correctly forecasted by Sim. 3 and 4 in the adjacent areas (not shown here) which means that there is not a simple shift of the peak value but a real reduction.

4 Conclusions and future work

Summarizing, we can state that:

- the assimilation of T2m (Sim. 3) improves T2m and seems to have neutral or slightly positive impact on the other variables (W10m, Slp, Rh2m);
- the assimilation of the other variables (alone or in combinations, not shown here), produces fuzzy results, especially in the assimilation cycle, but sometimes also in the forecast;
- the vertical profiles are much less perturbed by the assimilation (expected), but below 2000 m there is still a small (positive) impact;
- the precipitation does not always improve, except with the assimilation of T2m which changes the results a bit in the desired direction;
- the results look coherent for the three case studies.

A reason for the general improvement with the assimilation of T2m is certainly linked to the much larger number of thermometers spread in a homogeneously way inside the territory compared to the other sensors (see Tab. 3).

About the future work, the next steps can be here presented:

- investigation of a longer period (1-15 September 2008, summer regime) for a larger statistics;
- comparison of Ctrl and Sim. 3 (assimilation of T2m, not only for h <700 m) for the 00 and the 12 runs up to +24h (12h assimilation cycle and 12h free forecast);
- investigation of a second period (to be defined) but in winter regime.

References

Stauffer, D.R., and Seaman, N.L., 1990: Use of four-dimensional data assimilation in a limited-area mesoscale model, Part.1: Experiments with synoptic-scale data. Mon. Wea. Rev., 118, 1250-1277.

Stauffer, D.R., and Seaman, N.L., 1994: Multi-scale four-dimensional data assimilation. J. Appl. Meteor., 33, 416-434.

Stein, U., and Alpert, P., 1993: Factor Separation in Numerical Simulations. J. Atm. Sc., 50, 14, 2107-2115.

A linear solution for flow over mountains and its comparison with the COSMO model

Michael Baldauf

Deutscher Wetterdienst, Frankfurter Str. 135, 63067 Offenbach, Germany

1 Introduction

Comparing against analytical solutions for the equations of motion is one of the main testing tools during the development of dynamical cores. The broadest class of analytical solutions are linearisations and the most important ones are the solutions for flow over mountains. Such solutions are well known since several decades (e.g. Queney, 1948, Smith, 1979, 1980). The problem in the application of model testing lies in the choice of the approximations made for them. Whereas for a physical understanding of the atmosphere the challenge lies in the choice of profound approximations to get simple but still realistic solutions (or better say: simple formulae). In contrast for the testing of dynamical cores as few as possible approximations should be made, or better say, the system of equations used for the analytic solution should be as close as possible to the equations underlying the numerical model. It is not important that the analytic solution (or formula) is simple, but that it can be calculated with a much higher numerical confidence than the numerical solution of PDE's, e.g. by numerically calculating integrals or Fouriertransforms.

During the COSMO priority project 'Runge-Kutta' a program for calculating linear solutions for flow over mountains of the compressible Euler-equations for a stably stratified atmosphere with a constant Brunt-Vaisala frequency was developed. The *prerequisites* are: adiabasy, no friction, no Coriolis force, dry atmosphere, and no earth curvature. Further on the prerequisite is made, that the inflow does not change direction with height. The only a priori *approximation* done is that of linearisation about the mountain height. These prerequisites are easily fulfilled for the dynamical core by switching off the other processes; the approximation is easily fulfilled by choosing a very small hill. The only additional (a posteriori) approximation is to neglect a small height dependency of the vertical wavelength k_z. The error induced by this is estimated by the program.

All in all the requirements are stronger than those which can be found in the literature, but this allows to reduce the number of approximations only to the two mentioned before, which can be easily controlled.

2 Linearised equations

This section presents the derivation of the solution for linear flow over mountains. The starting point are the papers of Smith (1979, 1980) with the following prerequesites:

- no friction
- only adiabatic processes (in particular no phase changes)
- ideal gas law
- $c_p = const.$, $c_v = const.$, $R = const.$

- All movements are taking place on a plane (no earth curvature)
- no Coriolis force

This leads to the following system of equations (Smith, 1979):

$$\begin{aligned}
\rho \frac{du}{dt} &= -\frac{\partial p}{\partial x}, && (1)\\
\rho \frac{dv}{dt} &= -\frac{\partial p}{\partial y}, && (2)\\
\delta_1 \rho \frac{dw}{dt} &= -\frac{\partial p}{\partial z} - \rho g, && (3)\\
\delta_2 \frac{\partial \rho}{\partial t} + \delta_3 \boldsymbol{v} \cdot \nabla \rho + \rho \nabla \cdot \boldsymbol{v} &= 0, && (4)\\
\frac{dp}{dt} &= c^2 \frac{d\rho}{dt}, \qquad c^2 := \frac{c_p}{c_V} \frac{p}{\rho}, && (5)\\
p &= \rho R T. && (6)
\end{aligned}$$

Here some *tracer-parameters* were introduced:

- $\delta_1 = 0/1$: hydrostatic / non-hydrostatic approximation
- $\delta_2 = 0/1$: incompressible / compressible model
- $\delta_3 = 0/1$: shallow / deep atmosphere

To linearize these equations a *base state* has to be chosen: it has to be stationary, hydrostatic and at most dependent from z (the last choice requires the neglection of the Coriolis force)

$$\begin{aligned}
u_0 &= u_0(z), && (7)\\
v_0 &= 0, && (8)\\
w_0 &= 0, && (9)\\
T_0 &= T_0(z), && (10)\\
p_0 &= \rho_0 R T_0, && (11)\\
\frac{\partial p_0}{\partial z} &= -g \rho_0. && (12)
\end{aligned}$$

Later on we will consider an atmosphere with a constant Brunt-Vaisala frequency N. This leads to the base state temperature profile

$$\begin{aligned}
T_0(z) &= T_0(z=0) \left(a - (a-1) e^{z/H} \right), && (13)\\
H &:= \frac{g}{N^2} \sim 100\, km, && (14)\\
a &:= \frac{g^2}{N^2 \, c_p \, T_0(z=0)} \sim 3. && (15)
\end{aligned}$$

Such an atmosphere has negative values of temperature above $z_{max} = H \log a/(a{-}1) \sim 35$ km for realistic values.

Perturbation equations The above chosen base state leads to the perturbation equations

$$\rho_0 \left(\frac{\partial u'}{\partial t} + u_0 \frac{\partial u'}{\partial x} + w' \frac{\partial u_0}{\partial z} \right) = -\frac{\partial p'}{\partial x}, \tag{16}$$

$$\rho_0 \left(\frac{\partial v'}{\partial t} + u_0 \frac{\partial v'}{\partial x} \right) = -\frac{\partial p'}{\partial y}, \tag{17}$$

$$\rho_0 \left(\delta_1 \frac{\partial w'}{\partial t} + \delta_1 u_0 \frac{\partial w'}{\partial x} \right) = -\frac{\partial p'}{\partial z} - g\rho', \tag{18}$$

$$\delta_2 \frac{\partial \rho'}{\partial t} + \delta_3 u_0 \frac{\partial \rho'}{\partial x} + \delta_3 w' \frac{\partial \rho_0}{\partial z} = -\rho_0 \left(\frac{\partial u'}{\partial x} + \frac{\partial v'}{\partial y} + \frac{\partial w'}{\partial z} \right), \tag{19}$$

$$\frac{\partial p'}{\partial t} + \delta_4 u_0 \frac{\partial p'}{\partial x} + \underbrace{w' \frac{\partial p_0}{\partial z}}_{=-g\rho_0 w'} = c_0^2 \left(\frac{\partial \rho'}{\partial t} + u_0 \frac{\partial \rho'}{\partial x} + w' \frac{\partial \rho_0}{\partial z} \right). \tag{20}$$

where a 4th tracer-parameter was introduced (Pichler, 1997):

- $\delta_4 = 0/1$: small / big Mach-numbers.

These perturbation equations are fouriertransformed, i.e. the fields are represented by waves of the form

$$\phi'(x,y,z,t) = \phi'(k_x, k_y, z, \omega) \cdot e^{i(k_x x + k_y y - \omega t)}. \tag{21}$$

This leads to

$$-i\omega u' + ik_x u_0 u' + \frac{\partial u_0}{\partial z} w' = -ik_x \frac{1}{\rho_0} p', \tag{22}$$

$$-i\omega v' + ik_x u_0 v' = -ik_y \frac{1}{\rho_0} p', \tag{23}$$

$$\delta_1 \left(-i\omega w' + ik_x u_0 w' \right) = -\frac{1}{\rho_0} \frac{\partial p'}{\partial z} - \frac{\rho'}{\rho_0} g, \tag{24}$$

$$-\delta_2 i\omega \rho' + \delta_3 ik_x u_0 \rho' + \delta_3 \frac{\partial \rho_0}{\partial z} w' = -\rho_0 \left(ik_x u' + ik_y v' + \frac{\partial w'}{\partial z} \right), \tag{25}$$

$$-i\omega p' + \delta_4 ik_x u_0 p' - g\rho_0 w' = c_0^2 \left(-i\omega \rho' + ik_x u_0 \rho' + \frac{\partial \rho_0}{\partial z} w' \right). \tag{26}$$

We first express u', v' and ρ' through the other variables

$$u' = \frac{1}{\omega - k_x u_0} \left(k_x \frac{1}{\rho_0} p' - i \frac{\partial u_0}{\partial z} w' \right), \tag{27}$$

$$v' = \frac{1}{\omega - k_x u_0} \left(k_y \frac{1}{\rho_0} p' \right), \tag{28}$$

$$\rho' = \frac{1}{\omega - k_x u_0} \left(\frac{1}{c_0^2} (\omega - \delta_4 k_x u_0) p' - i\rho_0 \left(\frac{g}{c_0^2} + \frac{1}{\rho_0} \frac{\partial \rho_0}{\partial z} \right) w' \right). \tag{29}$$

It is common practice to introduce the following denotations:

Heterogenity (Queney, 1947)

$$S_0 := \frac{1}{\rho_0} \frac{d\rho_0}{dz} \equiv \frac{d \log \rho_0}{dz} \tag{30}$$

Stability parameter

$$\beta_0 := \frac{1}{\Theta_0} \frac{d\Theta_0}{dz} \equiv \frac{d \log \Theta_0}{dz} \tag{31}$$

Mach-number

$$Ma := \frac{u_0}{c_0} \tag{32}$$

We are interested only in the stationary case $\omega = 0$ and to begin with we consider the case $k_x \neq 0$.

(29) simplifies to

$$\rho' = \frac{1}{c_0^2}\delta_4 p' - i\rho_0 \frac{1}{k_x u_0}\beta_0 w' \tag{33}$$

and (26) leads to

$$p' = i\frac{k_x}{k_x^2 + k_y^2}\frac{\rho_0 u_0}{\mu_0}\left(\left[\delta_3 \frac{g}{c_0^2} + \frac{1}{u_0}\frac{\partial u_0}{\partial z}\right] w' - \frac{\partial w'}{\partial z}\right), \tag{34}$$

where

$$\mu_0 := 1 - \delta_3\delta_4 \frac{k_x^2}{k_x^2 + k_y^2} Ma^2 \tag{35}$$

was defined. Both inserted into (24) delivers an ODE of 2nd order for $w'(k_x, k_y, z, \omega)$

$$\frac{d^2 w'}{dz^2} + \frac{dw'}{dz}\left(\frac{d}{dz}\log d(z)\right) + b(z)w' = 0 \tag{36}$$

with

$$d(z) = \frac{\partial}{\partial z}\log\frac{\rho_0}{\mu_0} + (\delta_4 - \delta_3)\frac{g}{c_0^2} = \begin{cases} \frac{\rho_0}{\mu_0} & \text{, if } \delta_4 = \delta_3 \\ \frac{1}{\Theta_0 \mu_0} & \text{, if } \delta_4 = 1, \delta_3 = 0 \\ \frac{\Theta_0 \rho_0^2}{\mu_0} & \text{, if } \delta_4 = 0, \delta_3 = 1 \end{cases} \tag{37}$$

$$b(z) = -\delta_1 \mu_0 k_h^2 - \left[\delta_3 \frac{g}{c_0^2} + \frac{\partial}{\partial z}\log u_0\right]\left(\frac{\partial}{\partial z}\log\frac{\rho_0 u_0}{\mu_0} + \delta_4 \frac{g}{c_0^2}\right) - \left[\delta_3 \frac{\partial}{\partial z}\frac{g}{c_0^2} + \frac{\partial^2}{\partial z^2}\log u_0\right] + \frac{g\beta_0}{u_0^2}\mu_0 \frac{k_h^2}{k_x^2} \tag{38}$$

With the variable transformation

$$w'(z) = \frac{1}{\sqrt{d}} W(z) \tag{39}$$

this can be transformed into an 'oscillation equation'

$$\frac{d^2 W}{dz^2} + k_z^2 W = 0, \tag{40}$$

$$k_z^2(k_x, k_y) := \frac{1}{4}\frac{d'^2}{d^2} - \frac{1}{2}\frac{d''}{d} + b \tag{41}$$

Therefore the main task is to solve this ODE with the appropriate boundary conditions, then to calculate the fields w', p', u', v', and ρ' by the above given formulas and to carry out a Fourier backtransformation to get these fields in the physical space.

There remain two special cases. The first one is $\omega = 0$, $k_x = 0$, $k_y \neq 0$. The original fouriertransformed perturbation equations (22)-(26) deliver successively $p' = 0$, $\rho' = 0$, $w' = 0$, and $v' = 0$. It is remarkable that no statement can be given for u'. This describes the fact that in a frictionless flow over a flat plane an arbitrary vertical shear can occur. The second special case is $\omega = 0$, $k_x = 0$, $k_y = 0$. Now u' and v' can be chosen arbitrarily. p' and ρ' are connected by (24). In the case $\delta_3 = 0$ (shallow atmosphere approximation) it follows from the lower boundary condition (see below) $w' = 0$. In the case $\delta_3 = 1$ (deep atmosphere) also only $w' = 0$ leads to an equation system without contradictions.

Boundary conditions We prescribe an orography $h(x, y)$. The *lower boundary condition* consists in the free-slip condition. Its linearisation in $z = h(x, y)$ leads to

$$w'(x, y, z = 0) \approx U_0 \frac{\partial h}{\partial x}. \tag{42}$$

A horizontal Fourier transform delivers

$$\tilde{w}'(k_x, k_y, z = 0) \approx i k_x U_0 h(k_x, k_y), \tag{43}$$

and with the above variable transformation follows

$$W(k_x, k_y, z = 0) \approx i k_x U_0 h(k_x, k_y) \sqrt{d(z = 0)}. \tag{44}$$

The *upper boundary condition* is a little bit more delicate. We assume that k_z^2 does not depend from z. In this case we can solve the oscillation equation directly

$$W(k_x, k_y, z) = A e^{i k_z z} + B e^{-i k_z z} \tag{45}$$

Two cases have to be distinguished:

- case $k_z^2 < 0$: only a solution which decays with height seems to be physical. We define $k_z := i\sqrt{-k_z^2}$ and omit the term $\sim B$.
- case $k_z^2 > 0$: the reuirement is that no energy transport to the ground takes place. Again we omit the term $\sim B$ and define $k_z := \mathrm{sgn}(U_0 k_x) \cdot \sqrt{k_z^2}$ (Smith, 1980).

Therefore for height independent k_z^2 we get the solution

$$W(k_x, k_y, z) = i k_x U_0 h(k_x, k_y) \sqrt{d(k_x, k_y, z = 0)} \cdot e^{i k_z z}. \tag{46}$$

3 A Case Study

A first test with the COSMO-model was done with the case described in Schär et al. (2002)[section 5b]. A 2D-flow over a modulated Gaussian hill

$$h(x) = h_0 \, e^{-\frac{x^2}{b^2}} \cos^2 \pi \frac{x}{\lambda} \tag{47}$$

with $b = 5$ km and $\lambda = 4$ km is considered. The atmospheric conditions are: inflow velocity of $U_0 = 10$ m/s, a constant Brunt-Vaisala-frequency $N = 0.01$ 1/s, and a surface temperature of $T(z = 0) = 288$ K. The maximum height of the mountains is $h_0 = 25$ m (reduced by a factor of 10 compared to Schär et al., 2002). This results in a small inverse vertical Froude number of $1/Fr = N h_0 / U_0 = 0.025$ and therefore allows the application of a linearized solution.

Simulations with two resolutions were made: the first uses $\Delta x = 500$ m, $\Delta z = 300$ m with a time step of $\Delta t = 8$ s as in Schär et al. (2002), the second uses $\Delta x = 250$ m, $\Delta z = 200$ m, and therefore a slightly smaller time step of $\Delta t = 6$ s. The first setup uses 80 vertical levels, the second one 120 levels, therefore in both setups the upper model boundary lies in $z = 24$ km. The upper relaxation zone starts in $z = 13$ km with a thickness of 11 km. Such a thick relaxation zone is crucial to damp out perturbations to be able to properly compare with the analytical solution. The COSMO-version 4.6 was used with the Runge-Kutta dynamical core (Namelist-Parameters irunge_kutta=1, irk_order=3). Simulation results after 24 h and the appropriate analytic solution are shown in figure . The similarity with the analytical solution

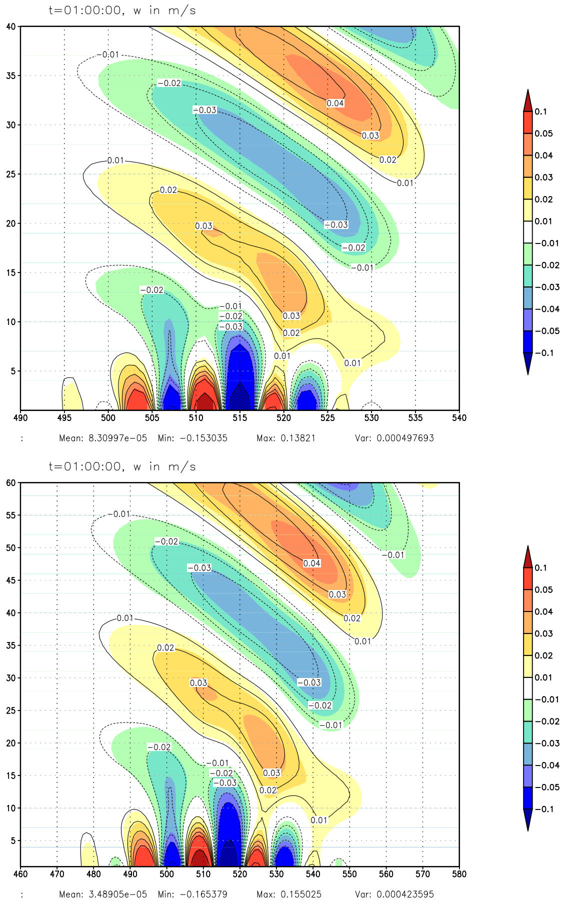

Figure 1: Comparison of the vertical velocity w between the COSMO-model (coloured) and the analytic solution (black lines) for the Schär et al. (2002) test case. Above: $\Delta x = 500$m, $\Delta z = 300$m, below: $\Delta x = 250$m, $\Delta z = 200$m.

is very close for both resolutions. Therefore even with $\Delta x = 500$ m , a good convergence has been reached.

References

Pichler, H., 1997: Dynamik der Atmosphäre, Spektrum Akademischer Verlag, Heidelberg.

Queney, P., 1948: The problem of air flow over mountains: A summary of theoretical studies. Bull. Am. Meteorol. Soc. 29, 16-26.

Schär, C., D. Leuenberger, O. Fuhrer, D. Lüthi, and C. Girard, 2002: A New Terrain-Following Vertical Coordinate Formulation for Atmospheric Predicition Models, Mon. Wea. Rev. 130/10, 2459-2480.

Smith, R. B., 1979: The influence of mountains on the Atmosphere, Adv. Geophys. 21, 87-220.

Smith, R. B., 1980: Linear theory of stratified hydrostatic flow past an isolated mountain, Tellus 32, 348-364.

Evaluation of Precipitation Forecast for the COSMO Model in Reference to Z vs. Terrain Following Coordinates Version

E. Avgoustoglou and I. Papageorgiou

Hellenic National Meteorological Service, El. Venizelou 14, Hellinikon, Athens 16777, Greece

1 Introduction

In our previous works (Refs. [8] and [9]), it was found that the earlier Z-coordinate versions of COSMO Model (former LM) (Refs. [1] - [7]) available for testing (i.e COSMO_Z_1.4 and COSMO_Z_1.5) showed relative preponderance over the terrain-following-coordinates version (COSMO_TF_3.15) which was used at the time for operational purposes at HNMS. The comparisons were focused on the precipitation associated with modest (Ref. [8]) and strong frontal activity over Greece (Ref. [9]) for COSMO_Z_1.4 and COSMO_Z_1.5 respectively. Since then, a significant amount of work was invested towards the development of a Z-coordinate (COSMO_Z_1.9) version which incorporates the latest advances of its COSMO_TF counterpart for more consistent comparisons. In consequence, part of our previous work (Ref. [9]) is evaluated again using the new version of COSMO_Z.

2 Case Study

The frontal development during the three day period of the 17^{th}, 18^{th}, and 19^{th} of November 2005 is re-investigated within this new framework. Based on the synoptic analysis presented in Ref. [9], we proceed directly into the comparison of the results of this past work and the control experiments performed with the latest version COSMO_Z_1.9 based again on the boundary conditions from the Global Model of the German Meteorological Service (DWD) with analysis of 00 UTC for every date under consideration. In Fig. 1, we present in the right column, the 12-hour forecasted accumulated precipitation from the control experiments using COSMO_Z_1.9 against the corresponding findings from our previous work (Ref. [9]) given in the left column. The results are further organized in three four-picture panels, one for every date considered. For every one of these dates and by directly looking at the forecasts from the later COSMO_TF control runs, there is a significant overall reduction of the accumulated precipitation against the older runs based on LM_TF_3.15. The impact of this feature is also depicted to the graphs stemming from COSMO_Z_1.9 against those of COSMO_Z_1.5 runs. On a more quantitative standpoint, the observed 12-hour accumulated precipitation observations for the available meteorological stations were compared against the nearest grid point corresponding forecasted values. A rather detailed presentation regarding the status of our results is given in Table 1 where the threat scores are presented for thresholds of 1-5 mm. The threat scores (TS) are defined as follows:

$$TS = \frac{Hits}{Observations + FalseAlarms}100 \tag{1}$$

where

$Hits$ are cases where observed and forecasted precipitation is greater or equal to a threshold value.

	November 17 57 Stations				November 18 55 Stations				November 19 55 Stations			
mm	TF_(1.9)	Z_1.9	TF_3.15	Z_1.5	TF_(1.9)	Z_1.9	TF_3.15	Z_1.5	TF_(1.9)	Z_1.9	TF_3.15	Z_1.5
1	60	57	60	65	26	31	10	27	67	73	59	79
	27,33,12	24,33,9	27,33,12	28,33,10	5,7,12	5,7,9	4,7,33	6,7,15	36,48,6	37,48,3	32,48,6	42,48,5
2	62	65	57	62	20	21	6	28	62	57	54	67
	24,30,9	22,30,4	24,30,12	25,30,10	3,5,10	3,5,9	2,5,31	4,5,9	31,45,6	29,45,6	28,45,6	34,45,6
3	67	70	52	68	16	22	0	12	51	47	51	66
	22,28,5	21,28,2	21,28,12	24,28,7	2,2,10	2,2,7	0,2,29	1,2,6	24,37,10	21,37,8	23,37,8	29,37,7
4	67	74	52	75	20	14	0	17	56	40	51	60
	20,26,4	20,26,1	20,16,12	24,26,6	2,2,8	1,2,5	0,2,28	1,2,4	22,30,9	16,30,10	20,30,9	24,30,10
5	65	77	55	74	20	25	0	0	58	39	54	54
	19,25,4	20,25,1	19,25,9	23,25,6	2,2,8	1,2,2	0,2,27	0,2,4	19,26,7	14,26,10	19,26,9	20,26,11

Table 1: Threat scores (%) for observed and forecasted precipitation. Hits, observations and false Alarms are ordered below the threat score values.

	November 17 57 Stations	November 18 55 Stations	November 19 55 Stations
Observed: Total	615.4	26.0	358.1
Average	10.8	0.5	6.5
Min	0.0	0.0	0.0
Max	55.0	12.0	42.0
LM_TF(1.9): Total	657.4	94.1	574.3
Average	11.5	1.7	10.4
Min	0.0	0.0	0.0
Max	73.1	12.9	99.7
LM_Z_1.9: Total	553.6	59.5	450.2
Average	9.7	1.1	8.2
Min	0.0	0.0	0.0
Max	77.8	8.1	83.3
LM_TF_3.15: Total	1024.5	588.5	788.8
Average	18.0	10.7	14.3
Min	0.0	0.0	0.0
Max	99.4	76.8	187.6
LM_Z_1.5: Total	632.5	65.6	487.8
Average	11.1	1.2	8.9
Min	0.0	0.0	0.1
Max	76.8	8.4	44.9

Table 2: Total and average observed and forecasted precipitation height (mm)

Observations are cases where observed precipitation is greater or equal to the threshold value.

FalseAlarms are cases where the observed precipitation is smaller than the threshold value and forecasted precipitation is greater than the threshold value.

As it can also be seen from Table 2, the COSMO_TF_CONTROL runs provide a significant improvement to the total precipitation estimation against the older COSMO_TF_3.15 version and in comparison to observation while the results between COSMO_TF_CONTROL and the versions of COSMO_Z become quite comparable.

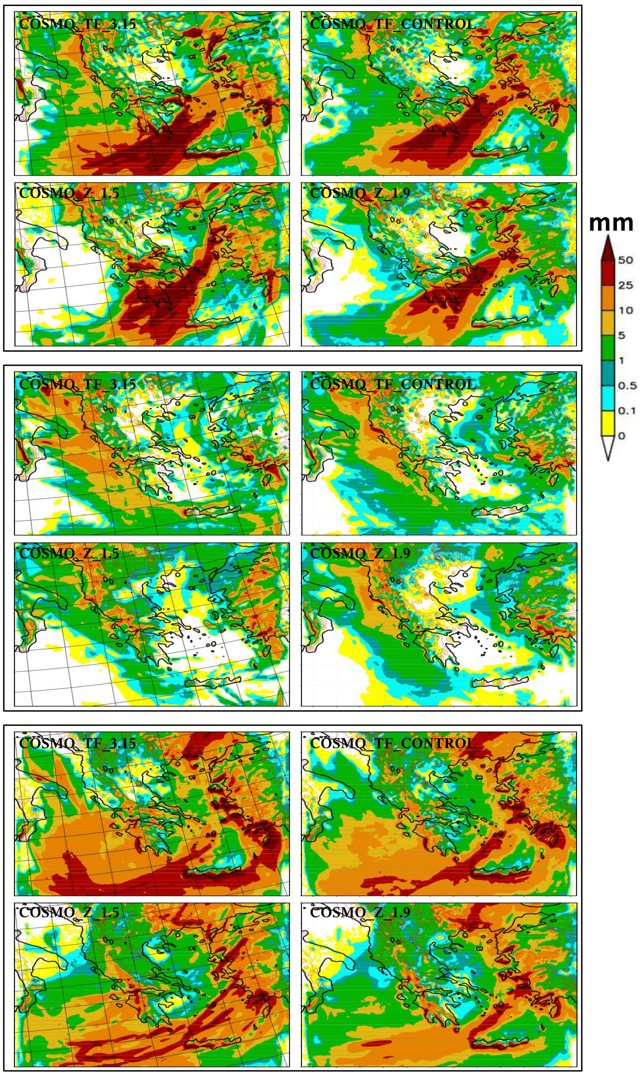

Figure 1: 12-hour (06 to 18 UTC) forecasted accumulated precipitation (mm) for 17, 18 and 19 of November 2005 in upper, middle and lower four-picture panels respectively. The initial conditions are from the Global Model of DWD based on 00 UTC analysis.

3 Summary and Outlook

In contrast to our previous works (Refs. [8] and [9]), the control runs using the latest version COSMO_Z_1.9, the preponderance of COSMO_Z against COSMO_TF is strongly reduced mainly because of the improvement that was observed in the results of COSMO_TF. However, COSMO_Z remains a fair alternative regarding precipitation.

References

[1] J. Steppeler, H.-W. Bitzer, M. Minotte and L. Bonaventura, 2002: Nonhydrostatic Atmospheric Modeling using a z-Coordinate Representation. *Mon. Wea. Rev.*, **130**, 2143-2149.

[2] H.-W. Bitzer and J. Steppeler, 2002: A description of the Z-Coordinate Dynamical Core of Lm. COSMO Technical Report, Deutscher Wetterdienst (DWD), Offenbach.

[3] J. Steppeler and H.-W. Bitzer , 2002: The Z-Coordinate Version of the LM. COSMO Newsletter No.2, 111-112.

[4] J. Steppeler and H.-W. Bitzer and U. Schättler, 2003: New Developments Concerning the Z-Coordinate Version of the LM. COSMO Newsletter No.3, 177-178.

[5] J. Steppeler, S. Janjic, H.-W. Bitzer, P. Prohl and U. Schättler, 2004: The Z-Coordinate LM. COSMO Newsletter No.4, 151-154.

[6] J. Steppeler, H.-W. Bitzer, S. Janjic, U. Schättler, P. Prohl, J. Parfiniewicz, U. Damrathh and E. Avgoustoglou, 2005: A Z-Coordinate Version of the Nonhydrostatic Model LM. COSMO Newsletter No.5, 149-150.

[7] Steppeler J, Bitzer HW, Janjic Z, Schättler U, Prohl P, Gjertsen U, Torrisi L, Parfinievicz J, Avgoustoglou E, Damrath U., 2006: Prediction of Clouds and Rain Using a z-Coordinate Nonhydrostatic Model. *Mon. Wea. Rev.* **134**, 3625-3643.

[8] E. Avgoustoglou, T. Tzeferi, V. Tirli, I. Papageorgiou, 2006: Application of the Z-Coordinate Version vs. Terrai Following Version of LM Nonhydrostatic Model over Greece. COSMO Newsletter No.6, 74-80.

[9] E. Avgoustoglou and I. Papageorgiou, 2007: Precipitation forecast of the Z-Coordinate vs. the Terrain Following Version of LM over Greece. COSMO Newsletter No.7 (submitted)

Introducing sub-grid scale orographic effects in the COSMO model

Jan-Peter Schulz

Deutscher Wetterdienst, Offenbach a. M., Germany

1 Introduction

Verification at the German Weather Service (DWD) has shown that the surface pressure in forecasts of the COSMO-EU model is systematically biased. COSMO-EU is an operational implementation of the COSMO limited area model (Doms and Schättler 2002, Schulz 2006) at DWD, covering almost all Europe using a mesh size of 7 km. In particular, in wintertime high pressure systems tend to develop a positive pressure bias, by 1-2 hPa after 48 h, low pressure systems a negative bias ("highs too high, lows too low") (see e. g. Damrath et al. 2007). At the same time the wind speed tends to be overestimated by up to 1 m/s throughout the entire troposphere. The wind direction near the surface shows a positive bias of some degrees.

The combination of these deficiencies leads to the hypothesis that in the model there is too little surface drag, causing an underestimation of the cross-isobar flow in the planetary boundary layer. Consequently, the solution would be to increase the surface drag in the model. This may be accomplished, for instance, by introducing an envelope orography (Wallace et al. 1983, Tibaldi 1986), but this has unfavourable effects e. g. for the simulated precipitation, or by including sub-grid scale orographic (SSO) effects, which were neglected in the COSMO model up to now. The SSO scheme by Lott and Miller (1997) has been selected for this. It is also included e. g. in the global models at ECMWF or DWD and works here well. In the following sections a short description of the scheme is given and results of numerical experiments comparing COSMO-EU with and without the SSO scheme are presented.

2 The sub-grid scale orography scheme

The SSO scheme by Lott and Miller (1997) deals explicitly with a low-level flow which is blocked when the sub-grid scale orography is sufficiently high. For this blocked flow separation occurs at the mountain flanks, resulting in a form drag. The upper part of the low-level flow is lead over the orography, while generating gravity waves.

In order to describe the low-level flow behaviour in the SSO scheme a non-dimensional height H_n of the sub-grid scale mountain is introduced:

$$H_\mathrm{n} = \frac{N\,H}{|U|} \tag{1}$$

where H is the maximum height of the mountain, U the wind speed and N the Brunt-Väisälä frequency of the incident flow. The latter is computed by

$$N = \sqrt{\frac{g}{\theta}\frac{\partial\theta}{\partial z}} \tag{2}$$

where θ is the potential temperature, g the acceleration of gravity and z the height coordinate.

A small $H_{\rm n}$ will mean that there is an unblocked regime, all the flow goes over the mountain and gravity waves are forced by the vertical motion of the fluid. A large $H_{\rm n}$ will mean that there is a blocked regime, the vertical motion of the fluid is limited and part of the low-level flow goes around the mountain. The SSO scheme requires four external parameters, which are the standard deviation, the anisotropy, the slope and the geographical orientation of the sub-grid scale orography. They are computed following Baines and Palmer (1990) from the same raw data set of orographic height which is also used for computing the mean orographic height in the model. This is currently the GLOBE data set (GLOBE Task Team 1999) which has a resolution of approximately 1 km.

The two components of the SSO scheme, i. e. the blocking and the gravity wave drag, can both be individually adjusted, or even be switched off, by a tuning parameter. Generally, these two SSO parameters need to be adjusted depending on the mesh size of the model. For this study, the same two parameter values were chosen in COSMO-EU (mesh size 7 km) as in the DWD global model GME (mesh size 40 km). This setting yields already good and satisfying results. They may be further improved by an extensive tuning effort, but this is left here for a future study.

3 Case study

In order to test the SSO scheme in COSMO-EU two continuous numerical parallel experiments, running analogously to the operational analyses and forecasts, were carried out: A reference experiment of COSMO-EU without SSO scheme (called REF), and an experiment of COSMO-EU with SSO scheme (called SSO). The period was 25 Feb. – 31 Mar. 2008.

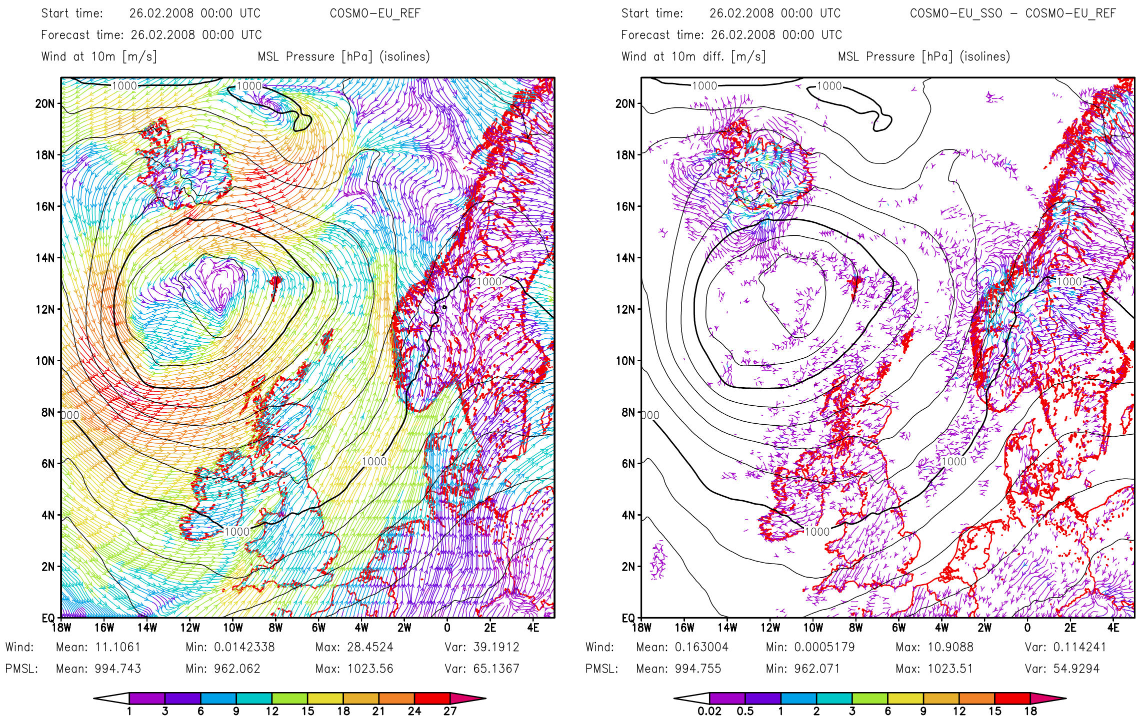

Figure 1: Left: 10-m wind (m/s) and mean sea level pressure (hPa) (isolines) simulated by the reference COSMO-EU without SSO scheme, 26 Feb. 2008, 00 UTC + 00h. Right: Difference of 10-m wind (m/s) between COSMO-EU with and without SSO scheme (SSO - REF), same date. The difference flow is usually pointing in opposite direction than the flow itself (over land), indicating that the flow is slowing down due to the SSO scheme.

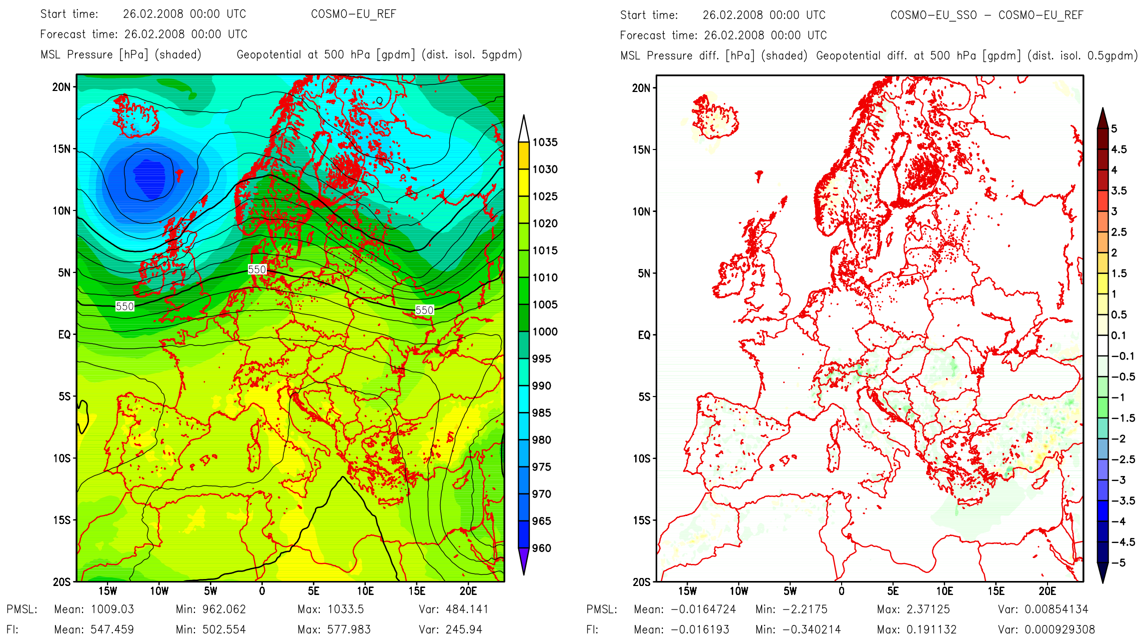

Figure 2: Left: Mean sea level pressure (hPa) and geopotential at 500 hPa (gpdm) (isolines) simulated by the reference COSMO-EU without SSO scheme, 26 Feb. 2008, 00 UTC + 00h. Right: Difference of mean sea level pressure (hPa) between COSMO-EU with and without SSO scheme (SSO - REF), same date.

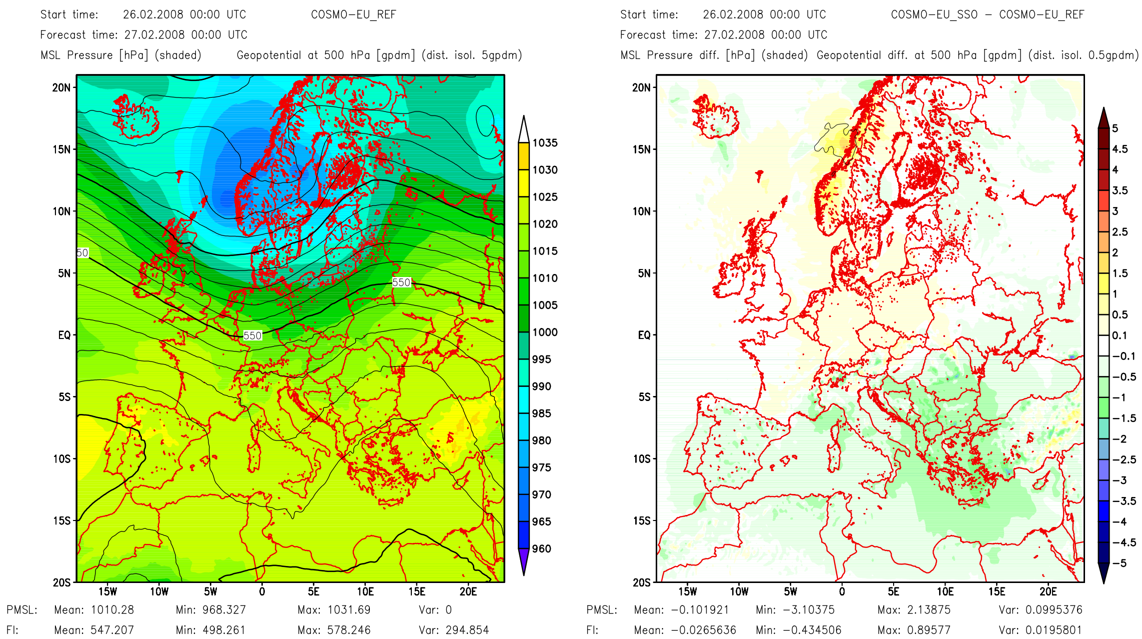

Figure 3: Same as Fig. 2, but for 26 Feb. 2008, 00 UTC + 24h.

This period was selected because several low pressure systems travelled through the model domain, providing good test cases for the SSO scheme.

One of them was on 26 Feb. 2008 which is presented here. Figure 1 shows the mean sea level pressure for the REF experiment in the Northwestern part of the model domain on 26 Feb. 2008, 00 UTC, at the beginning of the forecast, depicting a low pressure system over the Atlantic ocean, which was travelling eastward across Scandinavia during the next few days. The streamlines of the 10-m wind encircle the pressure system, with highest wind

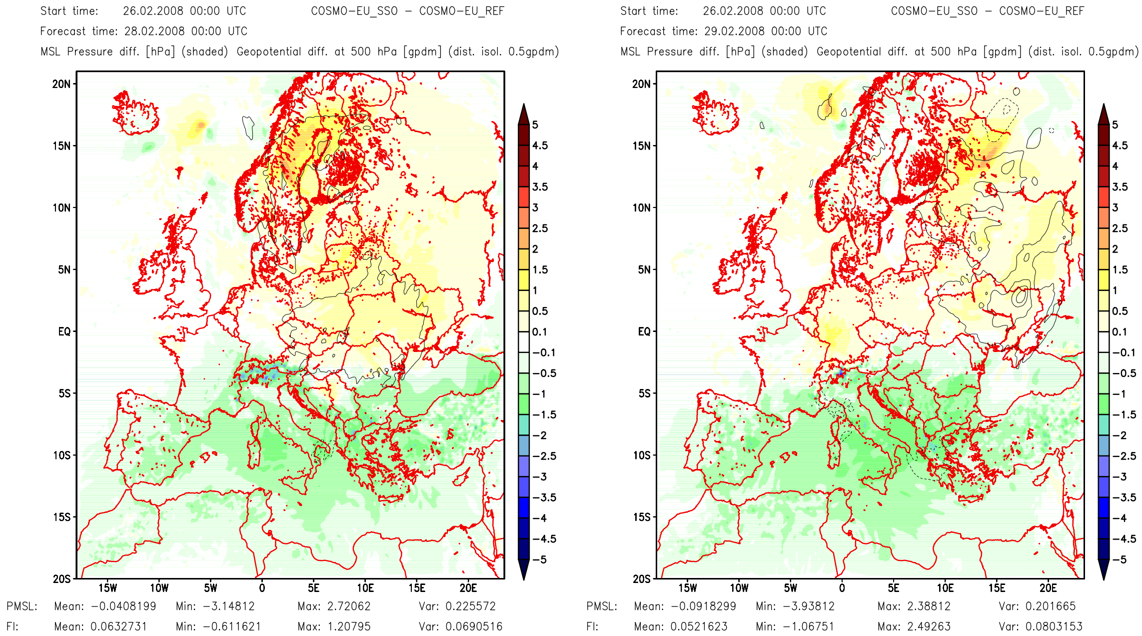

Figure 4: Difference of mean sea level pressure (hPa) between COSMO-EU with and without SSO scheme (SSO - REF). Left: 26 Feb. 2008, 00 UTC + 48h. Right: 26 Feb. 2008, 00 UTC + 72h.

speeds southwest of the core, where the pressure gradient is high, and generally lower wind speeds over land. Differences in the 10-m wind between the two experiments (SSO - REF) are mainly found over land. The difference flow is usually pointing in opposite direction than the flow itself, well seen for instance over the British Isles, indicating that the flow is slowing down due to the SSO scheme.

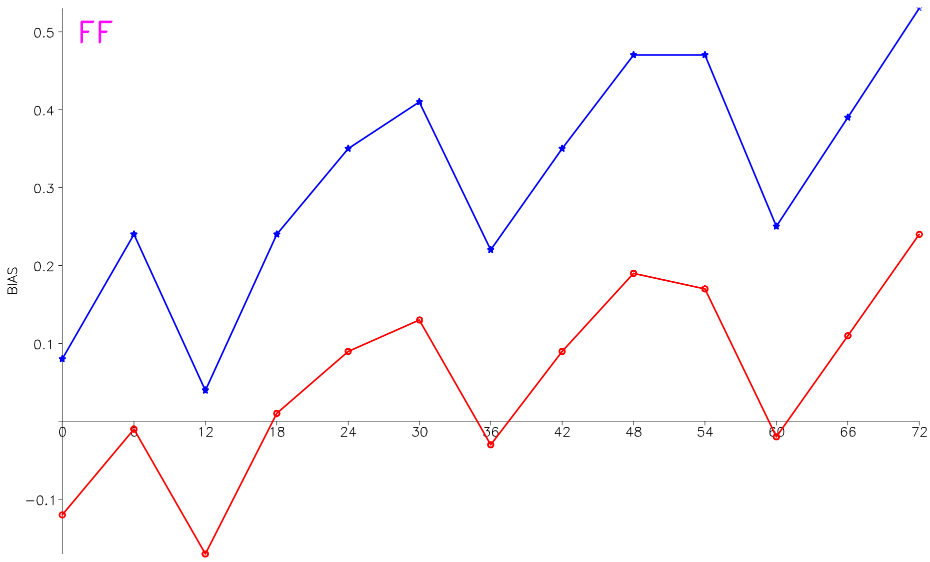

Figure 5: Bias of wind speed (m/s) versus forecast time (h) for the period 26 Feb. – 31 Mar. 2008, 00 UTC runs. Blue: Reference COSMO-EU without SSO scheme (REF), red: COSMO-EU with SSO scheme (SSO). All stations in the model domain were used.

Figure 2 shows the mean sea level pressure for the REF experiment in the full model domain, again on 26 Feb. 2008, 00 UTC. The low pressure system is clearly visible in the Northwest, in the Southern half of the domain, the mediterranean area, there stretches a region of prevailing high pressure. The geopotential at 500 hPa is overlaid as isolines showing the wave over

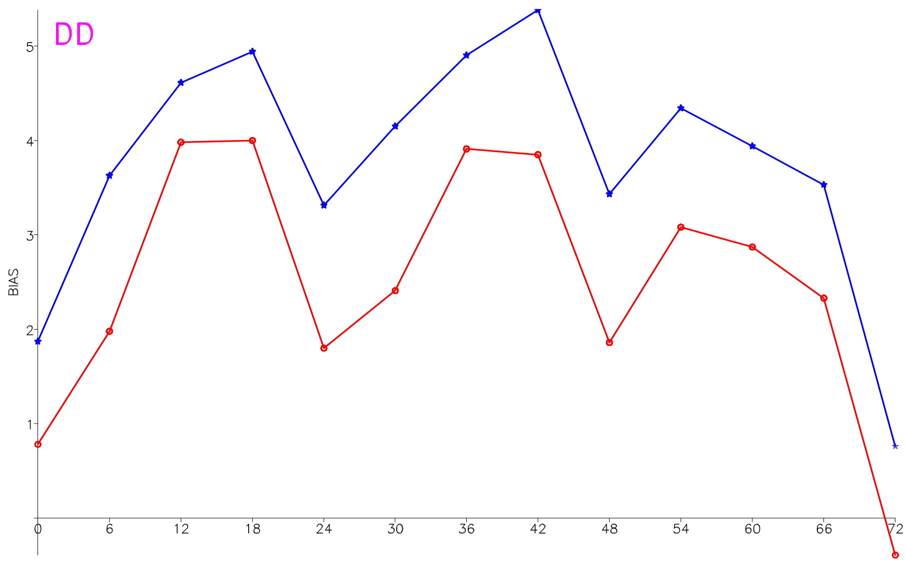

Figure 6: Same as Fig. 5, but for bias of wind direction (°). Blue: REF, red: SSO.

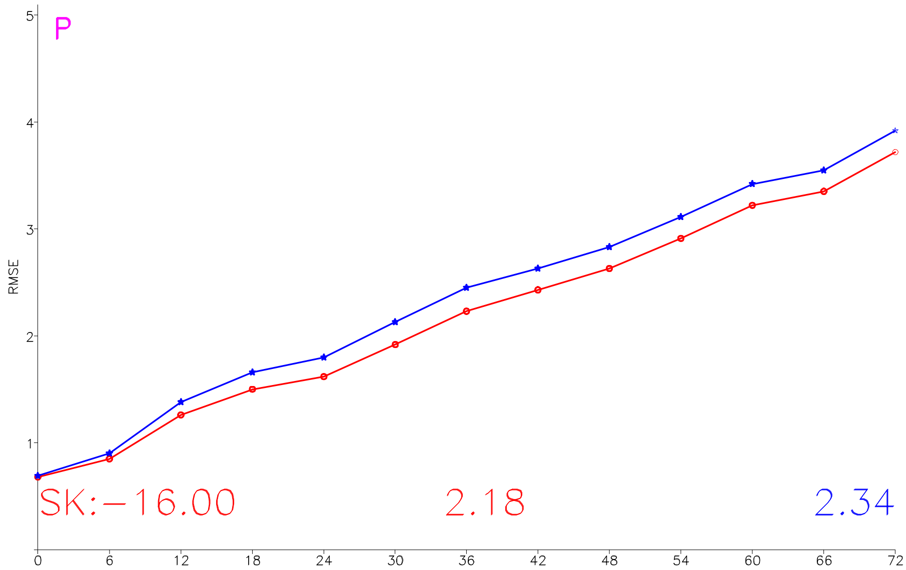

Figure 7: Same as Fig. 5, but for root mean square error of mean sea level pressure (hPa). Blue: REF, red: SSO. The reduction of its error variance in SSO amounts to 16%.

Northern Europe. In the beginning of the forecasts there are only very little differences in surface pressure between the two experiments. After 24h the low pressure system has moved further eastward (see Fig. 3). Pressure differences between the two experiments started to develop in a sort of dipole structure, the low pressure system in the North is filling up more efficiently in the SSO experiment compared to the REF experiment, the high pressure region in the South is weakening. This development continues during the further course of the forecasts while the low pressure system is moving eastward, Fig. 4 shows the pressure differences after 48h and 72h.

This case study shows that the SSO scheme, particularly by increasing the form drag, enhances the cross-isobar flow in the planetary boundary layer, which as a consequence helps filling up low pressure systems and weakening high pressure systems.

4 Numerical parallel experiments

In this section an objective verification of the REF and SSO experiment is presented. Figure 5 compares the biases of the wind speed versus the forecast time for the period 26 Feb. – 31 Mar. 2008. The REF experiment shows a positive bias of up to 0.5 m/s, while the SSO

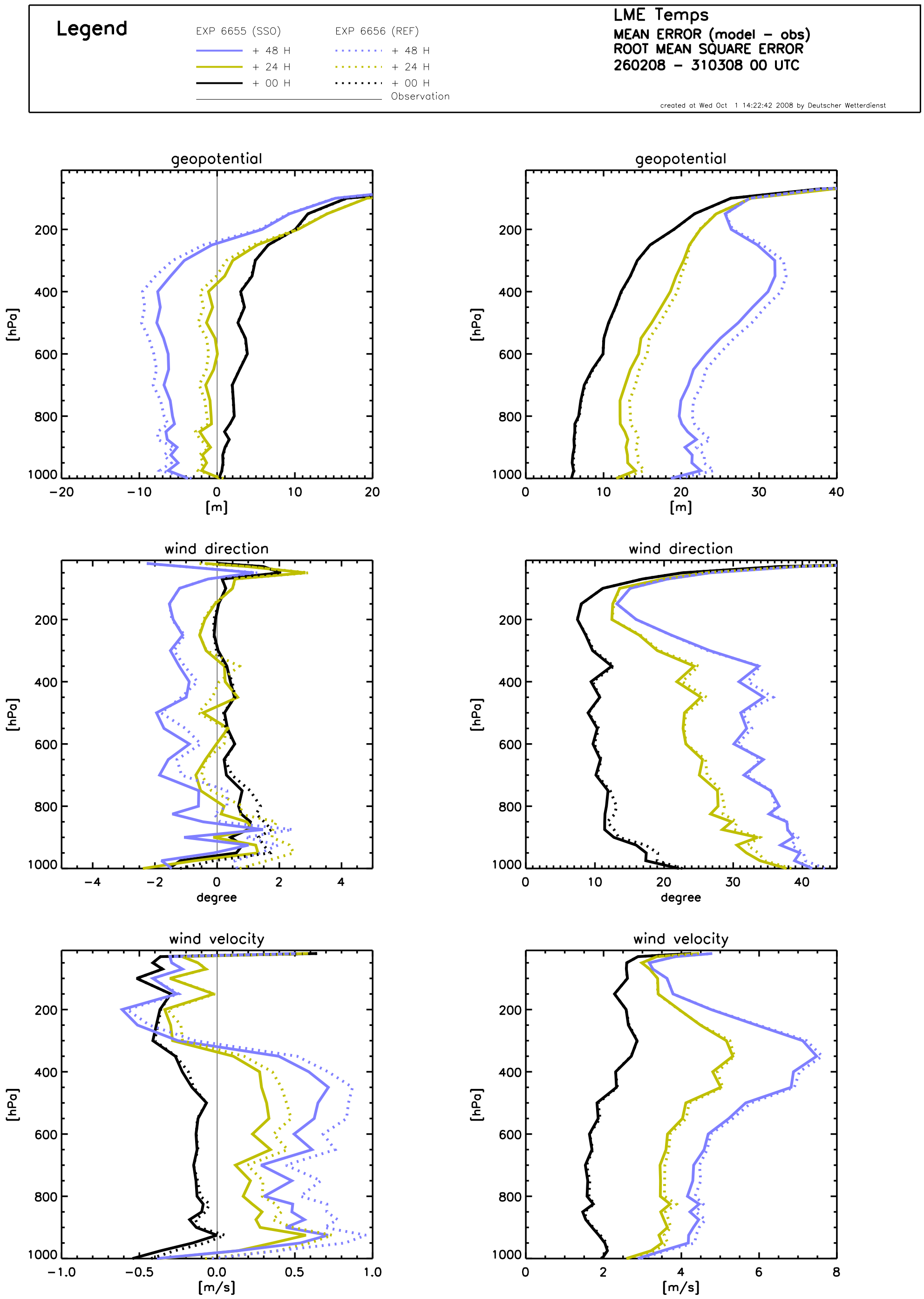

Figure 8: Upper air verification for geopotential (top), wind direction (middle) and wind speed (bottom) for the period 26 Feb. – 31 Mar. 2008, 00 UTC runs. Dotted lines: Reference COSMO-EU without SSO scheme (REF), solid lines: COSMO-EU with SSO scheme (SSO). Left column: Bias, right column: Root mean square error. Black lines: + 00h, yellow lines: + 24h, blue lines: + 48h. All radio sondes in the model domain were used.

experiment is basically bias free. The positive bias of the wind direction is reduced by about 1° in the SSO experiment (Fig. 6). The root mean square error of the vector wind is reduced as well, and also the negative bias of the mean sea level pressure (not shown). In particular, the root mean square error of the mean sea level pressure is significantly reduced, namely, the reduction of its error variance amounts to 16% (see Fig. 7). This means that the pressure patterns are much better captured by COSMO-EU with the SSO scheme.

Figure 8 presents an upper air verification of the two experiments with respect to geopotential, wind direction and speed. This shows a similar and consistent improvement of the model performance by the SSO scheme as well. COSMO-EU without the SSO scheme tends to develop a negative bias in the geopotential and a positive bias in the wind speed, both throughout the entire troposphere. Both biases are reduced by the SSO scheme. Furthermore, a positive bias in the wind direction in the lower troposphere is also getting smaller. Finally, the root mean square errors of all three quantities are slightly reduced as well.

5 Conclusions

The sub-grid scale orography scheme by Lott and Miller (1997) was implemented in the COSMO model. The scheme takes care of two different processes: a blocking of the low-level flow in case the sub-grid scale orography is sufficiently high, and a treatment of gravity waves excited in the flow over the mountains which will propagate through the atmosphere and eventually dissipate. Both processes tend to slow down the mean flow on different levels in the model. In particular the increased form drag results in an enhanced cross-isobar flow in the planetary boundary layer. As a consequence this weakens the development of high pressure systems and helps filling up low pressure systems.

This behaviour of the SSO scheme was successfully tested in COSMO-EU in a selected case study. The objective verification of a continuous numerical experiment with the SSO scheme in COSMO-EU for the period 26 Feb. – 31 Mar. 2008 shows good improvements. In particular, the positive bias of the surface wind speed is basically removed, and the positive bias of the surface wind direction is reduced. The root mean square error of the mean sea level pressure is significantly reduced, namely, the reduction of its error variance amounts to 16%. This means that the pressure patterns are much better captured by the model. Not shown was that the negative bias of the mean sea level pressure is reduced as well, and also the root mean square error of the vector wind. In addition to the surface weather elements the upper air verification shows a similar and consistent improvement as well.

Acknowledgement

Thanks to Ulrich Damrath and Ulrich Pflüger, DWD, for their verifications.

References

Baines, P. G. and T. N. Palmer, 1990: Rationale for a new physically based parametrization of sub-grid scale orographic effects, *European Centre for Medium-Range Weather Forecasts*, Tech. Memo. 169, Reading, 11 pp. (Available at: http://www.ecmwf.int).

Damrath, U., B. Brown and P. Nurmi, 2007: Different types of verification results required by different users, Presentation at the 3rd International Verification Methods Workshop, 31 Jan. – 2 Feb. 2007, Reading. (Available at:

http://www.ecmwf.int/newsevents/meetings/workshops/2007/jwgv/workshop_presentations/-U_Damrath.pdf).

Doms, G. and U. Schättler, 2002: A description of the nonhydrostatic regional model LM. Part I: Dynamics and Numerics, *Deutscher Wetterdienst*, Offenbach, 134 pp. (Available at: http://www.cosmo-model.org).

GLOBE Task Team, 1999: The Global Land One-kilometer Base Elevation (GLOBE) Digital Elevation Model, version 1.0, National Oceanic and Atmospheric Administration, National Geophysical Data Center, 325 Broadway, Boulder, Colorado 80305, USA. (Digital data base available at: http://www.ngdc.noaa.gov/mgg/topo/globe.html).

Lott, F. and M. J. Miller, 1997: A new subgrid-scale orographic drag parametrization: Its formulation and testing, *Q. J. R. Meteor. Soc.*, **123**, 101–127.

Schulz, J.-P., 2006: The new Lokal-Modell LME of the German Weather Service, *COSMO Newsletter*, **6**, 210–212. (Available at: http://www.cosmo-model.org).

Tibaldi, S., 1986: Envelope orography and maintenance of quasi-stationary waves in the ECMWF model, *Adv. Geophys.*, **29**, 339–374.

Wallace, J. M., S. Tibaldi and A. Simmons, 1983: Reduction of systematic forecast errors in the ECMWF model through the introduction of an envelope orography, *Q. J. R. Meteor. Soc.*, **109**, 683–717.

Component testing of the COSMO model's turbulent diffusion scheme

Balázs Szintai and Oliver Fuhrer

MeteoSwiss, Krähbühlstrasse 58, 8044 Zürich, Switzerland

1 Introduction

In the framework of the COSMO Priority Project UTCS (Towards Unified Turbulence-Shallow Convection Scheme) the current one-equation turbulence scheme of the COSMO model was further evaluated. The aim of this evaluation was to better understand and eventually improve the current scheme. The work was focused on the component testing of the one-equation scheme. The budget terms of the TKE equation were analysed one-by-one. During the component testing, the results of COSMO simulations were compared to Large Eddy Simulation (LES) data and turbulence measurements. In the present paper the results of the evaluation of an ideal convective case will be presented.

2 Method

For the parameterization of atmospheric turbulence the COSMO model uses a one-equation scheme, which corresponds to level 2.5 in the Mellor and Yamada notation (Mellor and Yamada, 1974 and 1982). This closure type carries a one-dimensional prognostic equation for turbulent kinetic energy (TKE), which can be written using the conventional notation as:

$$\frac{\partial e}{\partial t} = -\beta g \overline{w'\theta_v'} - \overline{u'w'}\frac{\partial U}{\partial z} - \overline{v'w'}\frac{\partial V}{\partial z} - \frac{\partial \left[\overline{w'(\frac{1}{2}u'^2_i + (p'/\rho))} \right]}{\partial z} - \epsilon,$$

where $e = \frac{1}{2}\overline{u'^2_i}$ is defined as TKE per mass unit. The term on the left hand side of the equation is the local tendency of the TKE. Terms on the right hand side refer to the buoyancy and shear production/destruction, the turbulent and pressure transport of TKE and the dissipation of TKE. In the COSMO model's scheme the turbulent transport of TKE (due to velocity-velocity triple correlation) and the pressure transport of TKE (due to velocity-pressure correlation) are parameterised together through the down-gradient formulation. For the parameterization of dissipation the Kolmogorov hypothesis is used. In the turbulence closure applied, equations for all second-order moments (fluxes and variances) except for the TKE are reduced to algebraic relations where the fluxes of momentum and scalar quantities are approximated with the down-gradient approach.

During the component testing of the turbulence scheme most of the above terms were analysed separately. It is important to note that in the current configuration all the terms are discretized using an implicit scheme, except for the turbulent transport term, which is discretized using an explicit scheme.

3 Results - Ideal case

The ideal convective case which was investigated for this study is described in Mironov et al. (2000). The setting for this simulation was a horizontally homogeneous and flat terrain with constant heating rate at the bottom. In the simulation no phase changes were considered (dry case) and wind shear was neglected. For this case the LES dataset was available from Dmitrii Mironov (DWD), containing all the TKE budget terms, which were important for the evaluation. Figure 1 shows the scaled profiles of TKE and the TKE budget terms after the steady state was achieved.

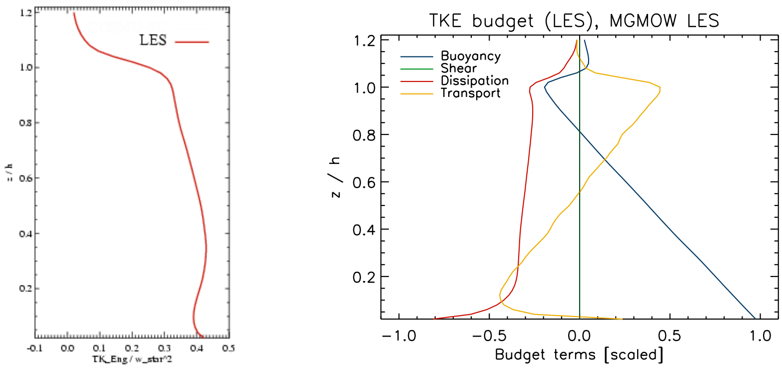

Figure 1: Scaled profiles of TKE (left) and the TKE budget terms (right) from the Large Eddy Simulation of the ideal convective case.

The above described case was simulated with the single column version of the COSMO model (Raschendorfer, 2007). In the first step, the settings of COSMO-2 were used. COSMO-2 is run operationally at MeteoSwiss at a horizontal resolution of 2.2 km. In the single column simulation 60 vertical levels were used with the first level at 10 m height, and the timestep for the integration was 72 s. The results (Fig. 2) show that the turbulent transport of TKE is too weak in the COSMO model, compared to the LES results. Consequently, TKE values at the top of the planetary boundary layer (PBL) are low and the negative bouyancy flux in the entrainment zone is nearly completely missing.

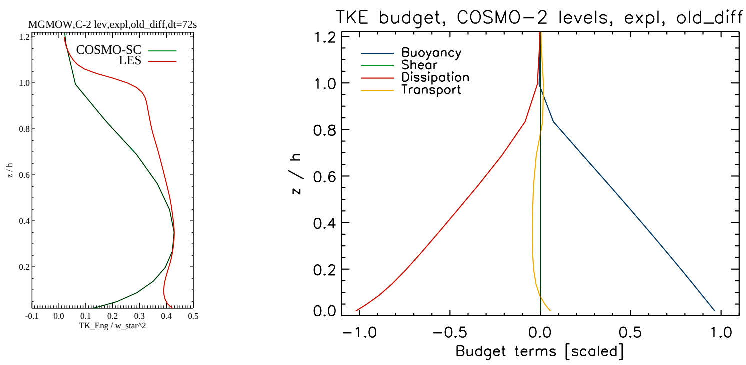

Figure 2: Scaled profiles of TKE (left) and the TKE budget terms (right) from the COSMO simulation with the operational level distribution and dt=72 s.

Due to the stretched vertical level distribution of COSMO-2, the model layers are relatively thick (around 100 m) near the top of the PBL. In the next step it was investigated, whether an increased resolution in the PBL would result in a better description of the transport term. To achieve this, a 10 m equidistant level distribution was tried with the same integration timestep (72 s). The result of this simulation (Fig. 3) is astonishing at first sight, because the transport term completely vanishes, causing a sharp decrease of TKE at the PBL top. The cause for this strange behaviour is a numerical limiter in the explicit scheme of the transport term. This numertical limiter is active, if the selected timestep is too large for the given vertical level distribution.

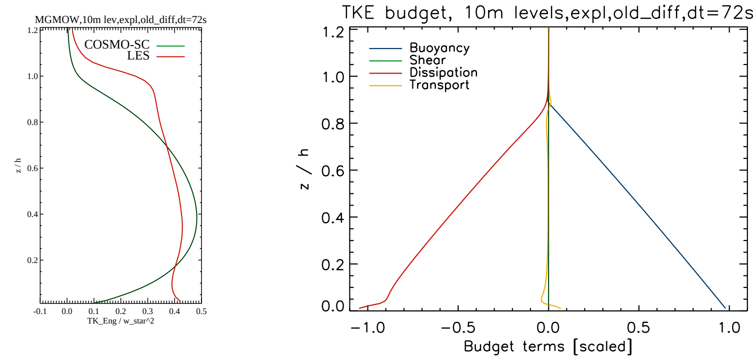

Figure 3: Scaled profiles of TKE (left) and the TKE budget terms (right) from the COSMO simulation with 10 m equidistant level distribution and dt=72 s.

To achieve a physically consistent solution without any numerical limitations, first, the numerical limiter in the transport term should be deactivated. This was realized in two different ways. First, an appropriately small timestep was chosen, and secondly, a semi-implicit formulation of the transport term was implemented. Figure 4 shows the result of the first approach. To achieve a stable integration without the numerical limiter, a significantly smaller timestep of 3.6 s had to be used for 10 m equidistant levels. It has to be noted, that the solution was independent of the vertical resolution, if the correct timestep was used in each case (eg. dt=7.2 s for 20 m equidistant levels).

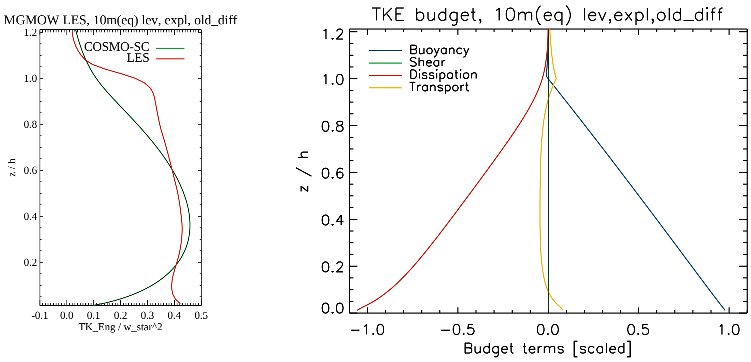

Figure 4: Scaled profiles of TKE (left) and the TKE budget terms (right) from the COSMO simulation with 10 m equidistant level distribution and dt=3.6 s.

In the case of the second approach a semi-implicit formulation was implemented for the transport term, which allowed the use of large timesteps even for very high (even 1 m) vertical resolution. Due to the semi-implicit approach the solution was independent of the vertical resolution and timestep (Fig. 5).

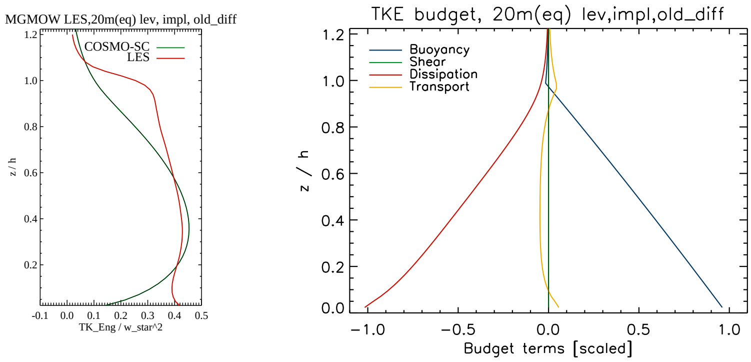

Figure 5: Scaled profiles of TKE (left) and the TKE budget terms (right) from the COSMO simulation with semi-implicit formulation for the transport term (20 m equidistant level distribution with dt=72 s).

4 Conclusion and Outlook

In the experiments described above a COSMO model solution of the ideal convective boundary layer was achieved which is independent of the vertical resolution and the timestep, consequently, representing the physical capabilities of the current turbulence scheme in such a situation. Compared to the LES results the turbulent transport of TKE is too weak in the COSMO model, and as a consequence TKE values near the PBL top are too low. This results in an insufficient negative bouyancy flux in the entrainment zone. If we compare the diagnosed horizontal velocity variances (not shown) with the LES results, it turns out that the anisotropy of turbulence is badly described in the COSMO model, i.e. the horizontal variances are too low in the upper and lower part of the PBL. The experiments have also shown the drawbacks of the explicit handling of the transport term. Consequently, in future developments a semi-implicit approach should be considered.

As a next contribution to the UTCS Project, a real-world convective case will be simulated with the COSMO model. For this experiment the LITFASS-2003 campaign (Beyrich and Mengelkamp, 2006) was chosen. To analyze the behaviour of the turbulence scheme in a real situation, COSMO results (both single column and three dimensional) will be compared to LES data and turbulence measurements.

Acknowledgements The authors would like to thank Dmitrii Mironov for providing the LES dataset and for useful discussions about the results. We would also like to thank Mathias Rotach, Pirmin Kaufmann and Matteo Buzzi for their help in analysing the results.

References

Beyrich, F. and H.-T. Mengelkamp, 2006: Evaporation over a heterogeneous land surface: EVA_GRIPS and the LITFASS-2003 experiment - an overview. Bound.-Layer Meteor., 121, 5-32.

Mellor, G. L. and T. Yamada, 1974: A hierarchy of turbulence closure models for planetary boundary layers. J. Atmos. Sci., 31, 17911806.

Mellor, G.L. and T. Yamada, 1982: Development of a turbulence closure model for geophysical flow problems. Rev. Geophys. and Space Phys. 20, 851-875.

Mironov D. V., V. M. Gryanik, C.-H. Moeng, D. J. Olbers, and T. H. Warncke, 2000: Vertical turbulence structure and second-moment budgets in convection with rotation: A large-eddy simulation study. Quart. J. Roy. Meteor. Soc, 126, 477-515.

Raschendorfer, M., 2007: A single column (SC) framework applied to the COSMO local model (SCLM), available at Deutscher Wetterdienst (DWD), Offenbach.

Main results of the SREPS Priority Project

Chiara Marsigli, Andrea Montani, Tiziana Paccagnella

ARPA-SIM, Bologna, Italy

Flora Gofa, Petroula Louka

HNMS, Athens, Greece

1 Introduction

The SREPS Priority Project focussed on the building up of a high-resolution ensemble system for the short-range. The project main tasks were to develop and implement such an ensemble, then to run it over extensive testing periods and to evaluate the system features and performances.
This system has been built to fulfil some needs that have arisen in the COSMO community:

- to have a short-range mesoscale ensemble to improve the support especially in situations of high impact weather
- to have a very short-range ensemble for data assimilation purposes
- to provide boundary conditions for the COSMO-DE-EPS convection-resolving ensemble, currently under development at DWD.

Hence, the strategy to generate the mesoscale ensemble members tried to take into account as many as possible sources of uncertainty which affect the scales of interest in the weather forecast at the short time range, in order to model many of the possible causes of the relevant forecast errors.
The main issues which have been addressed in the system evaluation are: 1) if the system shows a good spread/skill relationship, representative of the capability of the ensemble in describing the forecast error 2) how the different perturbations contribute to the spread and to the skill of the system 3) which is the ensemble skill in the forecast of surface weather parameters.

2 System description and methodology of analysis

COSMO-SREPS (COSMO Short-Range Ensemble Prediction System) it is based on 16 integrations of the limited-area non-hydrostatic COSMO model at about 10 km of horizontal resolution, with 40 vertical levels.
The driving model error is described by means of a multi-analysis multi-boundary approach. Initial and boundary condition perturbations are applied by driving the 10-km COSMO runs with the four 25-km COSMO members of the Multi-Analysis Multi-Boundary SREPS system of AENM. These four lower resolution COSMO runs, nested on four different global models (IFS, GME, GFS, UM) which use independent analyses, are provided by INM for this purpose. A representation of the smaller scale uncertainty is accomplished by applying limited-area model perturbations to the 10-km COSMO runs. In particular, 4 different set-up

of the model physics have been adopted in the ensemble members: 1) control set-up 2) use of the Kain-Fritsch scheme for the parametrisation of the deep convection, instead of Tiedtke as in the control 3) tur_len parameter equal to 1000 instead of 500 as in the control 4) pat_len parameter equal to 10000 instead of 500 as in the control. The combination of the 4 possible choices for the driving run with the 4 possible choices for the physics set-up lead to the 16 member ensemble.
During the project, the system was run over two main testing periods:

- 21 selected days of Autumn 2006, characterised by intense precipitation over either the Alpine area or Germany
- the MAP D-PHASE DOP (June to November 2007).

During the D-PHASE OP, 99 full runs of the COSMO-SREPS system were performed, covering not continuously the period, 50 in summer (JJA) and 49 in autumn (SON). Each full run (made up of 16 COSMO-model integrations at 10 km) started at 00UTC. The lack of continuity in the runs was mainly depending on the availability of initial and boundary conditions provided by INM.
The analysis of the system was carried out over two COSMO regions: the Alpine area and Greece.
This is due to the availability of observations and to the COSMO scientists involved in the project. The climatology of two regions is very different, but both regions are quite complex from the geographical point of view (orography, proximity of the sea). In particular, it should be underlined that in Greece few and less intense precipitation events were observed during the D-PHASE period (this is why also the month of December has been included in the sample for Greece) and that summer 2007 was a remarkably hot one.
Different data-sets have been used for the evaluation:

- high-res alpine: a dense network of stations covering Northern-Central Italy and Switzerland, providing precipitation data accumulated over 24h, from 06 to 06 UTC (about 1400 stations)
- high-res Italy: a dense network of stations covering Northern-Central Italy, providing precipitation data accumulated over 6h (about 900 stations) and 2m temperature data (about 600 stations)
- synop alpine: the SYNOP stations covering approximately the same area (43-48 N 6-14 E, 218 stations)
- synop Greece: the SYNOP stations covering Greece (about 90 stations)

3 Results

3.1 The spread-error relationship

The evaluation of the spread-error relationship was carried out on the Alpine area only, showing that the system tends to be under-dispersive. The gap between the spread and the error has been observed for a number of meteorological variables, both surface and upper-air (2m temperature, mean-sea-level pressure, precipitation, temperature at 850 hPa, geopotential height at 500 hPa). Moving from towards upper-air variables, the gap decreases, but it is still detectable (not shown).

In Figure 1, the root-mean-square error of the ensemble mean and the root-mean-square spread of the ensemble (or ensemble standard deviation) are compared for the two seasons, in terms of 2m temperature. The error is computed by comparing forecasts interpolated on station points belonging to the synop alpine dataset with the corresponding observations; the spread is computed using these same interpolated forecast values, for homogeneity reasons.

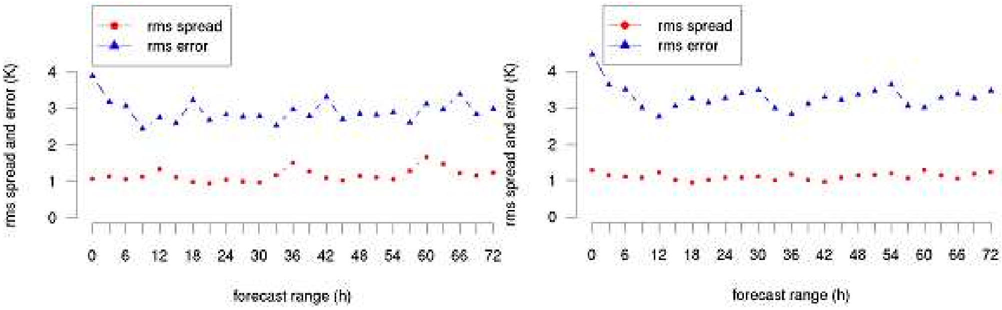

Figure 1: COSMO-SREPS spread (red) and error (blue) in terms of 2m temperature for summer (left) and autumn (right) 2007. Data are from the synop alpine dataset.

The ensemble spread is bounded between 1 and 2^oK in the summer season (Fig. 4, left panel), increasing with the forecast range and exhibiting a diurnal cycle, with values peaking at noon. In autumn (right panel) the spread stays close to 1^oK throughout the whole forecast range. In both seasons the ensemble mean error is quite larger than the spread, remaining below the 3^oK value in summer, with peaks grater than 3^oK at 18 UTC, while being generally above the 3^oK value in autumn. The gap between the two measures is due to both the underdispersion of the ensemble system and to the COSMO model systematic error, which should not be removed by ensemble techniques, but only by model improvement.

A better representation of the spread/skill relationship of the ensemble is shown in Figure 2, where the rms error is plotted as a function of the rms spread, after having divided the sample in classes of spread and computed for each class the average values of error and spread.

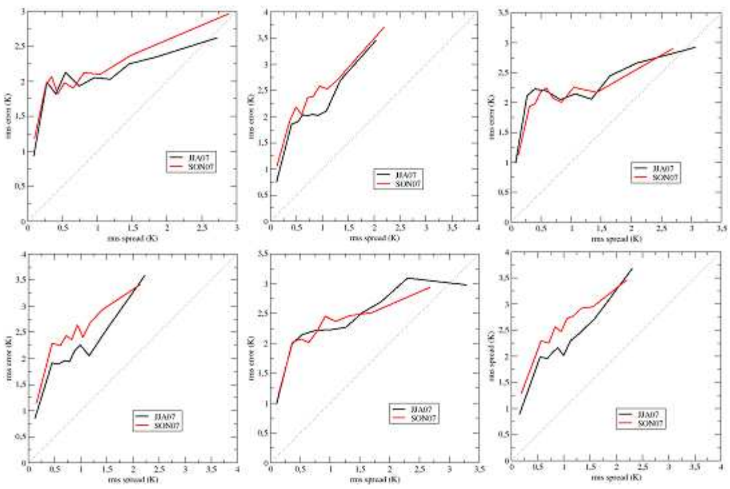

Figure 2: Spread/error relationship in terms of 2m temperature for summer (black line) and autumn (red line) 2007 for different forecast ranges (+12h, +24h, +36 h in the upper row, +48h, +60h, +72h in the lower row). Data are from the synop alpine dataset.

There is a clear correlation between error and spread, though at a given value of spread generally corresponds an higher value of error, even double. During the night (second, fourth and sixth panels, where data are from 00 UTC), the ensemble underdispersion is less marked in the summer season. At 12 UTC (first, third and fifth panels) there two seasons exhibit a more similar behaviour, with a good relationship for high spread values.

3.2 How different perturbations contribute to the ensemble skill

In order to assess the contribution to the skill of the system provided by the different ensemble members, verification of the performances of the 16 runs has been also made, both in terms of temperature and precipitation.
In terms of 2m temperature forecasts, the GME-driven members exhibit a peculiar behaviour in both the Alpine area and over Greece: the GME-driven members have better performance over both regions. Scores over Greece are shown in Figure 3.

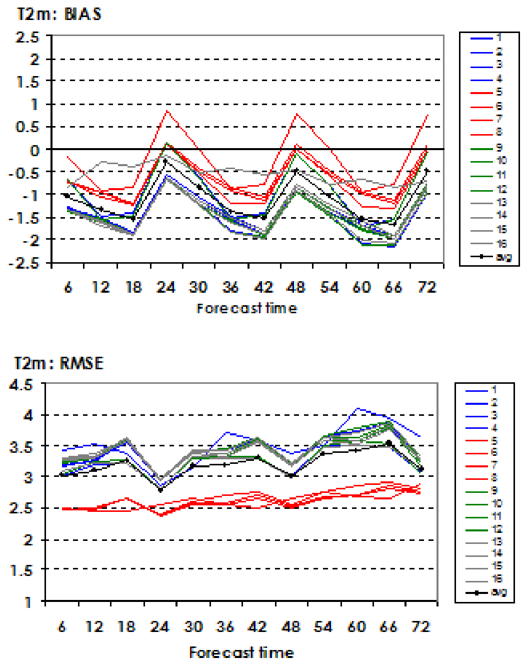

Figure 3: 2m temperature bias (upper panel) and RMSE (lower panel) for the 16 COSMO-SREPS runs, computed over Greece (lower panel, synop Greece dataset) for the whole period (June to December 2007).

It is worth pointing out that only the initial and boundary conditions provided to the GME-driven members are characterised by a coherence between soil and atmosphere. In fact, in the 25-km COSMO runs performed by INM, the atmospheric fields are provided by the 4 different global models, while the soil fields are always provided by the GME run. Hence, the coherence between atmosphere and soil in the "father" runs can have a positive influence on the forecast of 2m temperature by the GME-driven members.
In order to quantify the contribution of each type of perturbation to the ensemble skill, the scores of sub-ensembles made up by homogeneous members have been computed. The 16 members can be subdivided into 4 groups of 4 elements each, in 2 different ways:

- considering groups of elements homogeneous in terms of initial and boundary conditions, but distinct for the model parameterisations;

- considering groups of elements homogeneous in terms of the model parameters, but distinct in terms of initial and boundary conditions.

Considering 24h precipitation forecast, the scores have been computed for each of the 4 groups of 4 elements, in order to assess how the different forecast characteristics in terms of driving model and parameter contribute to the skill. The ROC area of the 4-member sub-ensembles are shown in Figure 4 for the autumn season and for the alpine area. The light blue line of each panel represents the ROC area of the full 16-member ensemble, which gives an indication of the COSMO-SREPS skill in forecasting precipitation for that period and in that particular area.

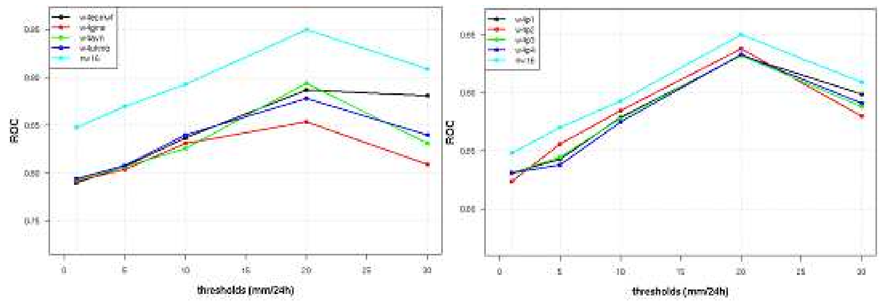

Figure 4: ROC area as a function of threshold for 24hr accumulated precipitation in the alpine area (high-res alpine data set) for the autumn season. Left panel: full 16-member COSMO-SREPS (light blue line) vs. 4-member ensembles with identical 'mother run' (black: ECMWF, red: GME, green: GFS, blue: UKMO). Right panel: full 16-member COSMO-SREPS (light blue) vs. 4-member ensembles with identical physical perturbation (black: p1, red: p2, green: p3, blue p4). Scores are for the +30 h forecast range.

Apart from the decrease in skill evident when passing from a 16-member to a 4-member ensemble, which is expected, it is worth pointing out that the different 4-member ensembles have different skill, which varies with the considered forecast range and also with threshold. In the right panel, the members of each sub-ensemble have identical physics perturbations. Therefore, these lines represent the skill of ensembles, which are perturbed in the initial and boundary conditions only, but have the same model set-up. Comparing each right panel with the corresponding left one suggests that perturbation of initial conditions generally yields more skilful performance than physical perturbation only. This is an indication of the fact that, the higher degree of diversity among members introduced by perturbing initial and boundary conditions determines a greater amount of skill with respect to the smaller-scale diversity introduced by the physics perturbations. As for the role of the different parameterizations, the 4-member ensemble where model perturbation p2 (Kain-Fritsch convection scheme) is applied to each member (red line on the right panels) turns out to be more skilful that other 4-member ensembles.
The same evaluation has been performed also for Greece. Scores over Greece are shown in Figure 5, for the whole period and at a +48h forecast range.

From these results is difficult to judge which driving-model leads to more skilful forecast, the results being dependent on the geographical area, on the season (not shown), on the forecast range (not shown) and on the precipitation threshold. As for the different parameter choice, we should be careful in the evaluation of the Kain-Fritsch members. They have the best performance in terms of ROC area but the worst in terms of BSS (not shown), due to the fact that they always tend to produce slightly too much rain (not shown).

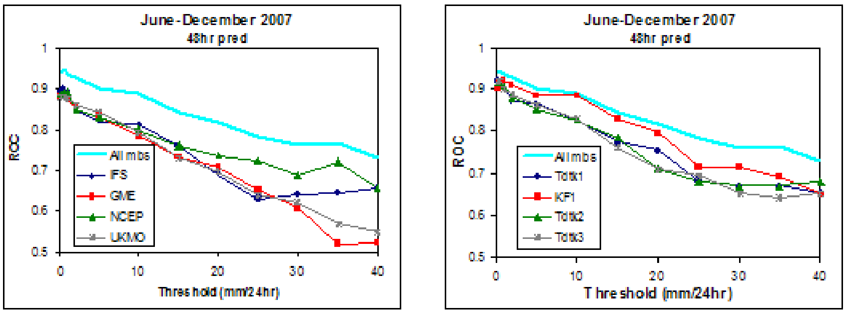

Figure 5: ROC area as a function of threshold for 24hr accumulated precipitation over Greece (synop Greece data set) for the whole period (June to December 2007). Left panel: full 16-member COSMO-SREPS (light blue line) vs. 4-member ensembles with identical 'mother run' (blue: ECMWF, red: GME, green: GFS, grey: UKMO). Right panel: full 16-member COSMO-SREPS (light blue) vs. 4-member ensembles with identical physical perturbation (blue: p1, red: p2, green: p3, grey p4). The forecast range is +48 h.

3.3 Study on parameter perturbations

Beside the COSMO-SREPS suite, a parallel suite, called CSPERT, was implemented and run continuously at ECMWF (but not in real time) for the whole Autumn 2007 (September-October-November, 91 runs). Since the preliminary tests on COSMO-SREPS had already identified a lack of spread due to due to an incomplete description of model uncertainty sources, this parallel suite was generated to choose more parameter perturbations for future implementation in COSMO-SREPS. This is necessary to increase the spread to values closer to the COSMO model error, especially for surface variables. The 16 perturbations involves also physical packages such as cloud and land schemes which had not been considered before. Initial and boundary conditions for the 16 runs were provided by the same run: the operational deterministic integration of ECMWF. The runs were starting daily at 00 UTC and the forecast range was 24 hours only.
The impact of the different set-up of the 16 runs on the selected meteorological variables is summarised in Table 1. The scores obtained by the 15 perturbed runs are evaluated against the score of the control run and a colour is assigned according to the performance:

- red: the perturbed run is worse than the control
- yellow: the perturbed run is slightly worse than the control
- light green: the perturbed run is slightly better than control
- green: the perturbed run is better than the control
- grey: the perturbed run is equivalent to the control
- white: no evaluation is possible, since the result changes with the forecast range

Looking at this table it is evident that none of the runs performs continuously better than the control, so that its set-up can be used as the new control set-up. Some improvement is possible by choosing rlam_heat=10, crsmin=200 and tur_len=1000, but it is yet to be investigated what effect will be if these three values are implemented in the same run. Instead, the choice of rlam_heat=0.1, c_lnd=1, c_soil=2 and tur_len=150 has lead to a worsening of the performances.
The fact that statistical behaviour of the various parameter set-ups "fluctuates" with respect

to the control run (it is not always better or worse) should be regarded as a positive outcome in this ensemble framework, since ensemble perturbations should be almost equivalent. The only set-ups which should be discarded are those which do not produce any (or a very small) impact (e.g. tur_len parameter).

	t BIA	t MAE	td BIA	td MAE	tp1 BS	tp1 TS	tp1 FA	tp10 BS	tp10 TS	tp10 FA
KF										
tur_len=150										
tur_len=1000										
pat_len=10000										
rat_sea=1										
rat_sea=60										
qc=0.001										
crsmin=50										
crsmin=200										
c_soil=0										
c_soil=2										
c_lnd=1										
c_lnd=10										
rlam_heat=0.1										
rlam_heat=10										

Table 1: Summary of the performances of the 15 perturbed runs with respect to the control.

4 Conclusions and future work

Some conclusions which can be drawn from the project are listed hereafter:

- there is a correlation between error and spread, but the system is under-dispersive, especially for surface variables
- the use of different driving models seems to dominate with respect to physics parameter perturbations as regards the contribution to the spread; these contributions are quite different in the two seasons in terms of 2m temperature
- the different driving models contribute differently to the ensemble skill, but the relative skill is strongly dependent on forecast range, season, verification area
- the different physics perturbations contribute differently to the ensemble skill as well
- for 2m temperature forecast, the GME-driven members perform generally better
- for precipitation forecast, perturbations of the convective schemes are more important than the perturbations of the particular parameters for turbulent and length scales used
- it seems that the members with Kain-Fritsch convective scheme have better probabilistic resolution but they overestimate precipitation more than Tiedtke scheme

Future work about the ensemble will be part of the new Priority Project CONSENS. In particular the work will focus mainly on:

- introduce the new parameter perturbations tested in the CSPERT suite, after an analysis of their impact also in a summer season
- analyse the impact of combine perturbations
- add perturbations of the lower boundary of the model
- combine the COSMO-SREPS ensemble with the COSMO-LEPS one, in a scientifically sound way

Performance of COSMO–LEPS system during the D–PHASE Operations Period

Andrea Montani, Chiara Marsigli, Tiziana Paccagnella

Hydrometeorological Regional Service ARPA–SIM, Bologna, Italy
email: amontani@arpa.emr.it

1 Introduction

COSMO–LEPS is the Limited–area Ensemble Prediction System developed and implemented by ARPA–SIM within COSMO (COnsortium for Small–scale MOdelling; the members of the Consortium are Germany, Greece, Italy, Poland, Romania and Switzerland). COSMO-LEPS project aims to generate "short to medium–range" (48–132 hours) probabilistic predictions of severe weather events based on the non–hydrostatic regional COSMO–model, nested on a number of ECMWF EPS members, chosen via a clustering selection technique (Marsigli et al., 2001).

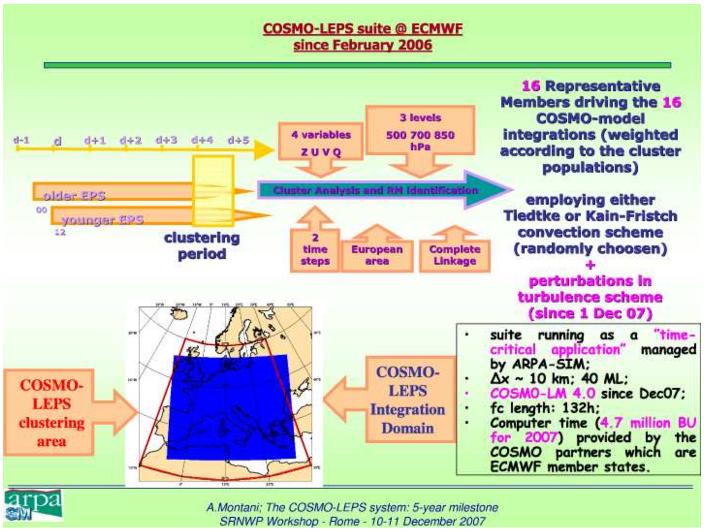

Figure 1: Present set–up of COSMO–LEPS operational suite.

The "experimental–operational" COSMO–LEPS suite (following the methodology described by Montani et al., 2003 and Marsigli et al., 2005) was set–up in November 2002 so as to produce probabilistic forecasts over a domain covering all countries involved in COSMO. After 6 years of activity, COSMO–LEPS application has become an "ECMWF member–state time–critical application" managed by ARPA–SIM and its present configuration in shown in Fig. 1. COSMO–LEPS is made up of 16 members, running at the horizontal resolution of 10 km with 40 model levels in the vertical. The computer–time to run COSMO-LEPS application on ECMWF supercomputers is provided from allocations to the ECMWF COSMO partners (i.e. Germany, Greece, Italy and Switzerland), whose contributions are joined into a unique "COSMO-account". Perturbations to the initial and boundary conditions are provided by the different EPS members driving the limited–area integrations. In addition to this, the following model perturbations are introduced:

- perturbations to the convection scheme: within each COSMO–LEPS integration, a random choice between Tiedtke or Kain–Fritsche convection scheme is made;
- perturbations in the maximal turbulent length scale;
- perturbations in the length scale of thermal surface patterns.

In this contribution, it is assessed the state–of–the–art of the system, showing its ability to provide warnings of severe weather events (e.g. heavy rainfall, strong winds, cold temperature anomalies).

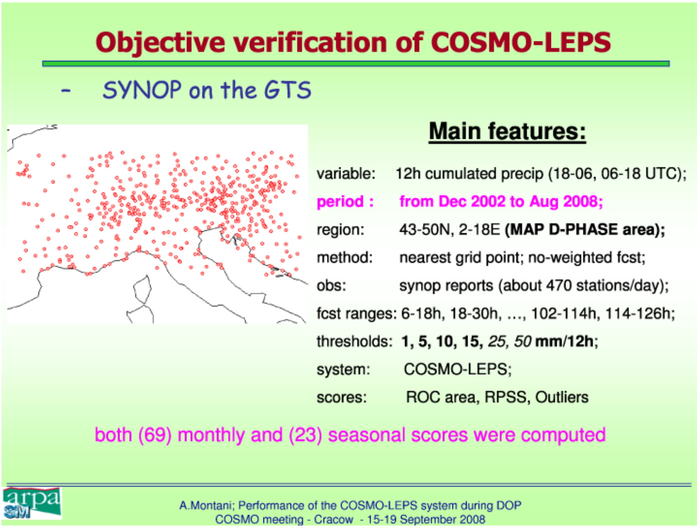

Figure 2: Main features of COSMO–LEPS verification.

2 Results of verification

As already mentioned, COSMO–LEPS has recently passed the 6–year milestone of activity. Therefore, a big verification effort was undertaken so as to assess objectively how the system changed in these years and the extent to which modifications have actually caused an improvement in terms of precipitation forecasts over mountainous areas.

In order to carry on this evaluation, a fix set of SYNOP stations (about 470) was selected, over an area covering the Alps (43-50N, 2-18E) and for the period ranging from December 2002 to August 2008. Precipitation accumulated over 12 hours (18-06 UTC and 06-18 UTC) was verified, comparing the values forecast on the grid–point nearest to each station against the observed values at that station. The other main features of the verification exercise are summarised in Fig. 2. Several probabilistic scores were used and the performance of the system was analysed both in terms of monthly and seasonal scores so as to identify the occurrence of possible seasonal variability.
As an example of the obtained results, Fig. 3 shows the performance of COSMO–LEPS in terms of the Relative Operating Characteristic (ROC) area, for 4 different thresholds (1, 5, 10, 15 mm/12h) at the 78–90h forecast range. Although the score is computed monthly, the 3–month running mean is actually shown in the plots to increase readability, due a marked month–to–month variability of the score itself. At the beginning of the verification period (early 2003), the ROC area scores (especially for high rainfall thresholds) were close to, or below, the 0.6 line, considered the discriminating value to detect between a useful and a useless forecast. Then, the scores increased for all thresholds starting from summer 2004.

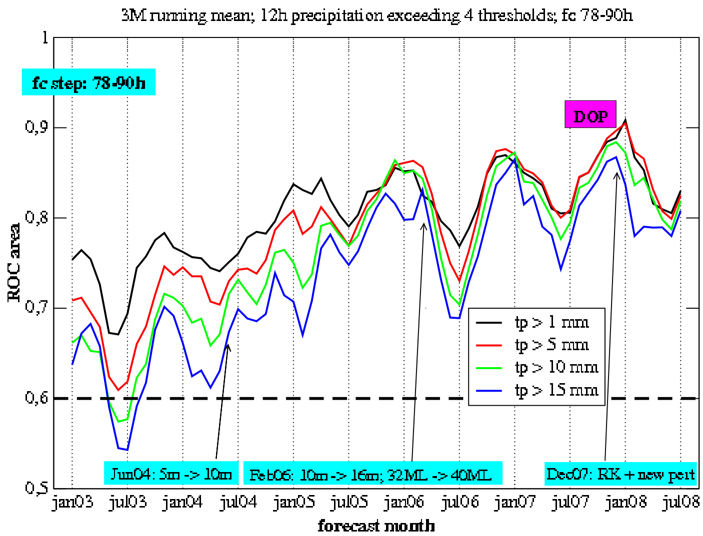

Figure 3: ROC area of COSMO–LEPS 12-hour precipitation forecasts for the forecast range 78–90h. The BSS was computed for each month, from January 2003 to July 2008. A 3-monthly running mean was applied to the scores to improve readability.

The ROC area has been well above 0.6 since spring 2004, for all the thresholds including the highest (15mm/12h). A different behaviour is exhibited in autumn 2006, which was a very dry season: COSMO–LEPS performance is not satisfactory. On the other hand, the ROC area is close to 0.8 during both 2007 and 2008, indicating a skillful system in the prediction of precipitation at the day–4 range. A marked seasonal variability is also evident, the system often performing better in the summer season.
In the overall evaluation of the system performance, it has to be kept in mind that, in addition to the upgrades in the COSMO–model itself, COSMO–LEPS configuration was subject to three major changes during the verification period:

- June 2004: the ensemble members were increased from 5 to 10 and only two EPS instead of three were considered to select the global–model members to drive the COSMO–LEPS integrations;
- February 2006: the ensemble members were increased from 10 to 16 and the vertical resolution of COSMO–LEPS integrations from 32 to 40 levels;
- December 2007: it was introduced the Runge–Kutta numerical scheme as well as new perturbations (in the maximal turbulent length scale and in the length scale of thermal surface patterns).

The former change seems to have led to better scores, since an improvement is evident from spring 2004. The impact of the latter change is more difficult to be judged, due to the already underlined problem in autumn 2006. Obn the other hand, a positive trend is well evident in the scores obtained in 2007, especially during the various meteorological experiments which took place during that year (e.g. COPS and MAP D-PHASE). This is also true if other scores, like the Brier Skill Score and the percentage of outliers, are considered (not shown).

As a final remark, it has to be pointed out that nowadays COSMO–LEPS forecast products are well–established in met–ops rooms across COSMO community. They have been recently used with success in EC projects (e.g. Windstorms PREVIEW) as well as in the field campaigns of the above–mentioned meteorological experiments. As future developments, it is planned to introduce more model perturbations, so as to improve the spread–skill relationship of the system, and to develop "calibrated" COSMO–LEPS forecasts.

References

Marsigli C., Montani A., Nerozzi F., Paccagnella T., Tibaldi S., Molteni, F., Buizza R., 2001: A strategy for high–resolution ensemble prediction. Part II: limited–area experiments in four Alpine flood events. *Quart. J. Roy. Meteor. Soc.*, **127**, 2095–2115.

Marsigli C., Boccanera F., Montani A., Paccagnella T., 2005: The COSMO-LEPS mesoscale ensemble system: validation of the methodology and verification. *Nonlin. Proc. Geophys.*, **12**, 527–536.

Montani A., Capaldo M., Cesari D., Marsigli C., Modigliani U., Nerozzi F., Paccagnella T., Tibaldi S., 2003: Operational limited–area ensemble forecasts based on the 'Lokal Modell'. *ECMWF Newsletter No. 98. Available from: ECMWF, Shinfield Park, Reading RG2 9AX, UK.*

Association of surface stations to NWP model grid points

Pirmin Kaufmann

MeteoSwiss, Zürich, Switzerland

1 Introduction

This document describes the algorithm to associate a surface station with a model grid point. This association is designed for delivery of direct model output at a station and for model verification with an optimized association of height dependent values. It is currently implemented and used in the operational verification of MeteoSwiss. The COSMO Working Group on verification has adopted this algorithm as a COSMO standard.

The algorithm searches grid points in the vicinity of the surface station, optimizing horizontal distance and vertical height difference. Land points in the model are preferred over water points, assuming that surface stations are located over land. This is important because some values as e.g. 2 m temperature are strongly influenced by the surface.

2 Search radius depending on model surface at station

First, the surface type (land or water) of the model at the station location is determined. The grid cell, which the station is located in, can be determined by rounding the grid coordinates of the station to the nearest whole number. The transformation of other than grid coordinates (e.g. geographical coordinates) to grid coordinates is not described in this document. Depending on the surface type of the respective model grid cell, the search radius for model grid points around the station is defined as:

$r_{search} = r_{land} = 1.415$ for land surface,
$r_{search} = r_{water} = 2$ for water surface, in model grid units.

The value of the radius is chosen to keep the method in close accordance with the previously used method but to allow a wider search area over a flat water surface.

3 Search area and preference of land points

All grid points within a horizontal distance of r_{search} of the exact station location are evaluated. The number of evaluated grid points depends on the location of the station relative to the model grid.

If at least one model grid point within the search radius has a land surface, all water points are excluded from the selection.

In the COSMO model, water surface is present when $FR\_LAND < 0.50$ or $SOILTYP = 9$.

4 Optimization of horizontal and vertical distance

Calculate the horizontal distance $d_{hor} = \sqrt{\Delta x^2 + \Delta y^2}$ (always positive) and the vertical height difference $d_{vert} = \Delta z$ of the station to all grid points to be evaluated, in the same geometrical length unit, e.g. in meter. Combine the two to an optimization distance d_{opt} according to:

$$d_{opt} = d_{hor} + |d_{vert}| \cdot f_{ve} \tag{1}$$

with the vertical emphasis factor $f_{ve} = 500$.

Then select the grid point with the smallest optimization distance d_{opt}. This grid point shall be the model grid point associated with the station.

Towards Operational Probabilistic Precipitation Forecast

Marco Turco, Massimo Milelli

ARPA Piemonte, Via Pio VII 9, I-10135 Torino, Italy

1 Aim of the work

Precipitation forecast from meso-scale numerical weather prediction (NWP) models often contains features that are not deterministically predictable and require a probabilistic approach. Therefore, a post-processing method has been developed in order to derive probabilistic precipitation forecasts from deterministic NWP model output. This method derives a Postprocessed Probabilistic Precipitation Forecast (PPPF) from a deterministic Direct Model Outputs (DMO) by using a spatio-temporal neighborhood method and it is based on the work of Theis et al., 2005 (see also Theis et al., 2002, Theis et al., 2003, Kaufmann, 2007). The procedure is applied to the output of the meso-scale model COSMO-I2, the regional very-high resolution version of the operational modelling system run in the framework of the COSMO consortium.

2 Implementation set-up

The procedure has been implemented on the intranet web page of ARPA Piemonte and at the moment is a tool for the ARPA forecasters only, but in its fully operational implementation it will be available for the Italian Department of Civil Protection. The procedure gives the probability of exceeding a certain threshold (1 mm/6h, 5 mm/6h, 15 mm/6h and 30 mm/6h) and two kind of maps are produced every 6h: over Piemonte region and over Italy. The probability in each grid point and in each forecast time is calculated considering the precipitation forecasted in that point and in the space-time neighborhood, using a certain radius in space and the previous and next forecast in time.

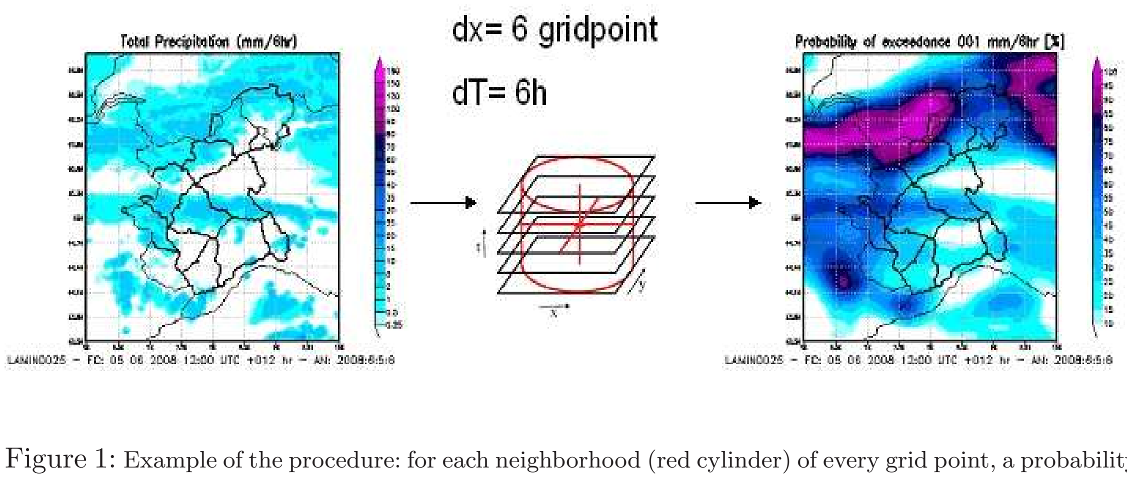

Figure 1: Example of the procedure: for each neighborhood (red cylinder) of every grid point, a probability distribution is calculated and it is converted in a map of probability of exceeding a given threshold.

The key assumption about this procedure is: QPF at the grid points within the neighborhood are assumed to be independent and identically distributed according to the probability density function of the precipitation forecast at the central grid point. Fig. 1 shows a schematic view of the procedure with the cylindrical neighborhood in the space-time plane (x, y and t), with the base in the space plane, and the vertical height in the time plane. The probability of exceeding a certain threshold is the number of the grid points within the neighborhood which are greater than the given threshold, divided by the total number of grid points within the neighborhood. In detail, a spatial radius of six grid cells is used (DX=6) and the spatial radius is kept constant within the temporal radius of 6 hours (DT=1). A crucial issue for these methods is the determination of an optimal size and shape of the neighborhood: in the following paragraph three space-time neighborhood methods have been tested in order to define the optimal one.

3 Verification

In the present study, we would like to answer to these two questions in an objective way:

- How does PPPF depend on the space and time windows ?
- Does this approach improve the DMO ?

In order to answer to these questions the verification procedure compares each observation in Piemonte (about 350 stations) with the nearest grid point, and calculates these scores (see Wilks, 1995 for more details):

- Reliability diagram (or attribute diagram): how well the predicted probabilities of an event correspond to their observed frequencies ?
- Brier Score (BS) & Brier Skill Score (BSS): what is the magnitude of the probability forecast errors ?
- ROC diagram: what is the ability of the forecast to discriminate between events and non-events ?
- Value diagram: given a cost/loss ratio C/L for taking action based on a forecast, what is the relative improvement in economic value between climatological and perfect information ? (see for instance Richardson, 2000)

The verification period is 1 year (June 2007 - May 2008) and 3 kinds of neighborhood are considered:

- DX=6 and DT=1 (i.e.: a circle of 6 grid points plus next and previous time steps, where the neighborhood has a cylindrical shape)
- DX=12 and DT=1 (cylindrical shape again)
- DX=6 and DT=0 (circular shape)

Since we have many combination of time steps (from +12 to + 42 hours), thresholds (1, 5, 15 and 30 mm/6h) and scores, in the following we will show only the results that are representative for deriving some general conclusion.

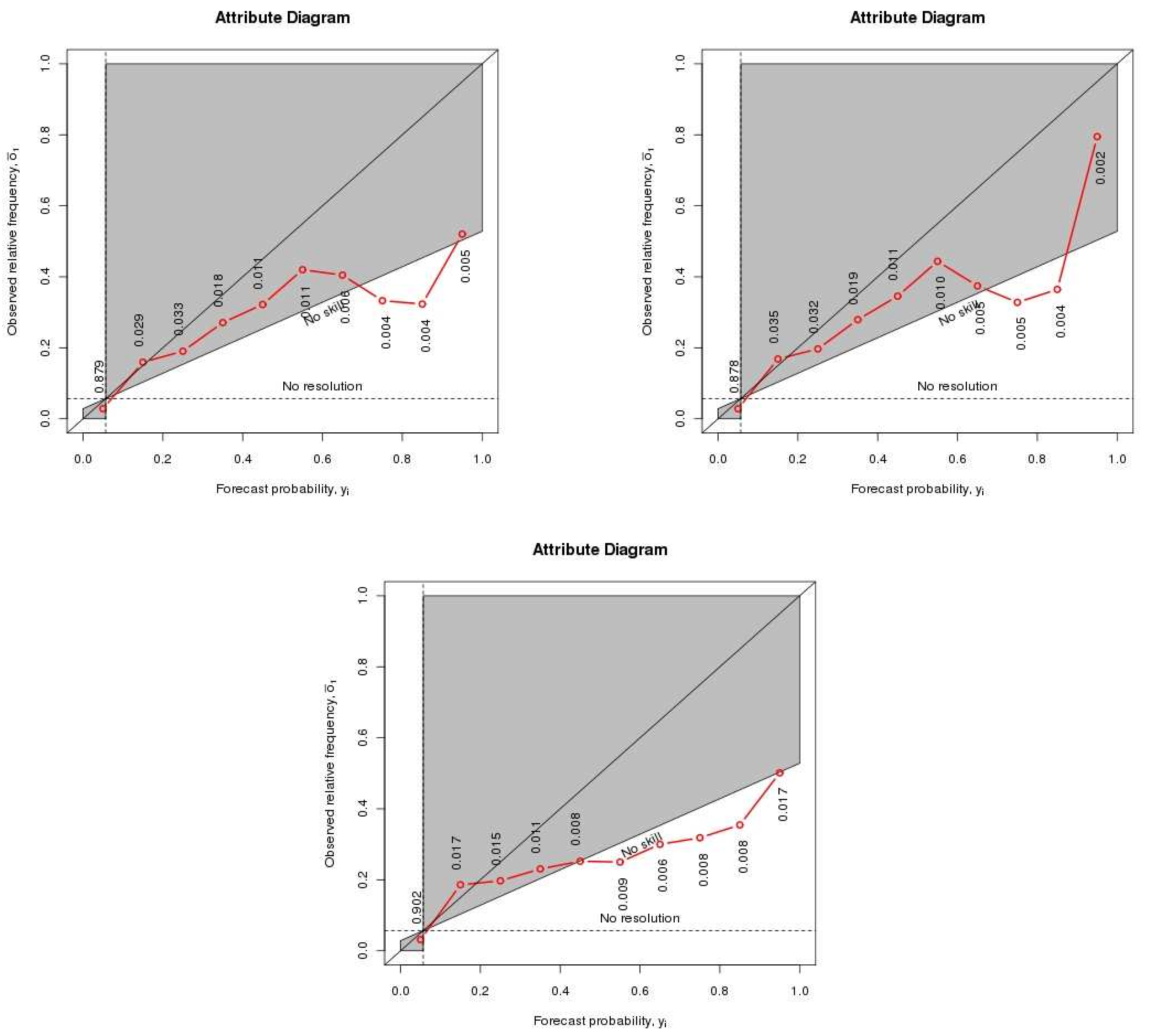

Figure 2: Reliability diagram (or attribute diagram) for the three different configurations: DX=6 and DT=1 (top left), DX=12 and DT=1 (top right), DX=6 and DT=0 (bottom) respectively with forecast time +42h and threshold 5 mm/6h.

Regarding the first question it is important to note that, as showed in Theis et al. (2005), an optimal universal neighborhood size cannot be determined: the effect of neighborhood size does not only depend on the precipitation amount, but also on the user's needs. The degree to which the forecast probabilities match the observed frequencies is shown in Fig. 2. The location of all the reliability curves (referred to the three neighborhoods for time step +42h and threshold 5 mm/6h) to the right of the diagonal indicates that the probabilities were always overestimated except for the 0.1 probability. For DX=12 and DT=1 and DX=6 and DT=1, only for 0.8 and 0.9 probabilities the PPPF have no skill whereas for the case with DX=6 and DT=0 all the higher probabilities have no skill.

Considering the accuracy (measured by the Brier Score BS, see Fig. 3), we show two examples: for the lowest (1 mm/6h) and the highest (30 mm/6h) thresholds. The best accuracy is achieved with DX=12 and DT=1 (small differences with respect to DX=6 and DT=1) and for the highest threshold, but this fact is not surprising since the Brier score is sensible to the climatological frequency of the event: if an event is rare, it is easier to get a good BS without having any real skill. In order to verify the ability of the forecast to discriminate between two

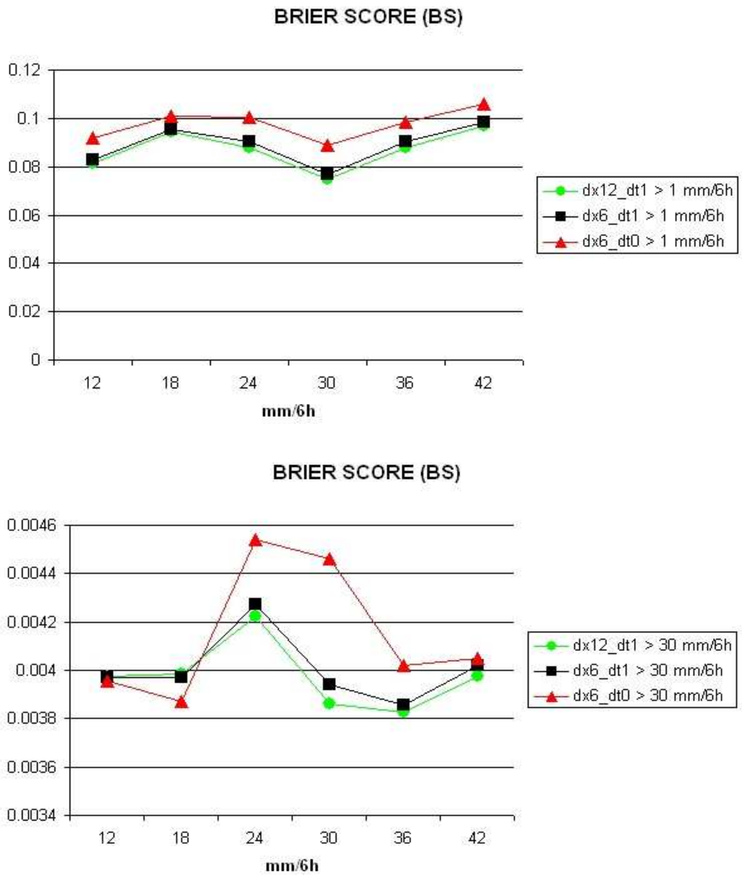

Figure 3: Brier Score for the lowest (1 mm/6h, top) and the highest threshold (30 mm/6h, bottom), for the three different configurations.

alternative outcomes, we consider the "Relative Operating Characteristic (ROC) Diagram", shown in Fig. 4. A perfect forecast would have a ROC curve starting in the lower left corner following the y-axis (false alarm rate=0) up to the top left corner, then following the x-axis (hit rate=1) until the upper right corner. The ROC curve for the three different PPPFs demonstrated that the best neighborhood is with DX=12 e DT=1, with small differences with respect to DX=6 and DT=1.

Summarizing, the results of the sensitivity study on DX and DT suggest that the best performances are obtained with DX=12 and DT=1, but they are not far from the DX=6 and DT=1 results, as it was also evident from all the other indices shown before. Therefore, since the DX=12 and DT=1 neighborhood has much more CPU costs (at least on our operational UNIX machines, where the DX=12 and DT=1 method requires 27 minutes of CPU and the DX=6 and DT=1 one only 10 minutes), we have chosen to use the latter in the operational setting.

In order to verify the ability of the forecast to discriminate between two alternative outcomes, we consider the "Relative Operating Characteristic (ROC) Diagram", shown in Fig. 4. A perfect forecast would have a ROC curve starting in the lower left corner following the y-axis (false alarm rate=0) up to the top left corner, then following the x-axis (hit rate=1) until the upper right corner. The ROC curve for the three different PPPFs demonstrated that the best neighborhood is with DX=12 e DT=1, with small differences with respect to DX=6

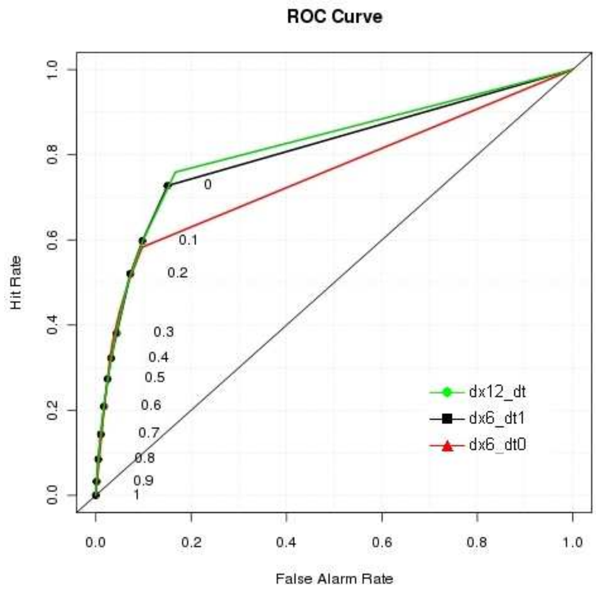

Figure 4: ROC diagram for the three neighborhoods fixed at forecast time +36h and threshold 5 mm/6h.

and DT=1. It can be noticed that considering the threshold of 5 mm/6h it is not evident the worsening with the forecast time. The best performances are found with DX=12 and DT=1, but they are not far from the DX=6 and DT=1 results, as it was also evident from all the other indices shown before. Therefore, since the DX=12 and DT=1 neighborhood has much more CPU costs (at least on our operational UNIX machines, where the DX=12 and DT=1 method requires 27 minutes of CPU and the DX=6 and DT=1 one only 10 minutes), we have chosen to use the latter in the operational setting.

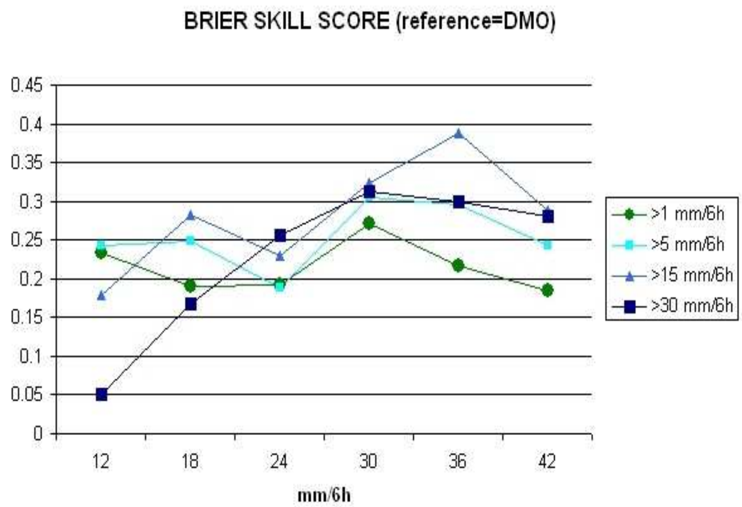

Figure 5: BSS with DMO used as a reference forecast.

The second question is "Does this approach improve the DMO ?". An answer is provided by the Brier Skill Score (BSS) that measures the improvement of the PPPF relative to a reference forecast (in this case the DMO). The BSS is constructed so that perfect forecast

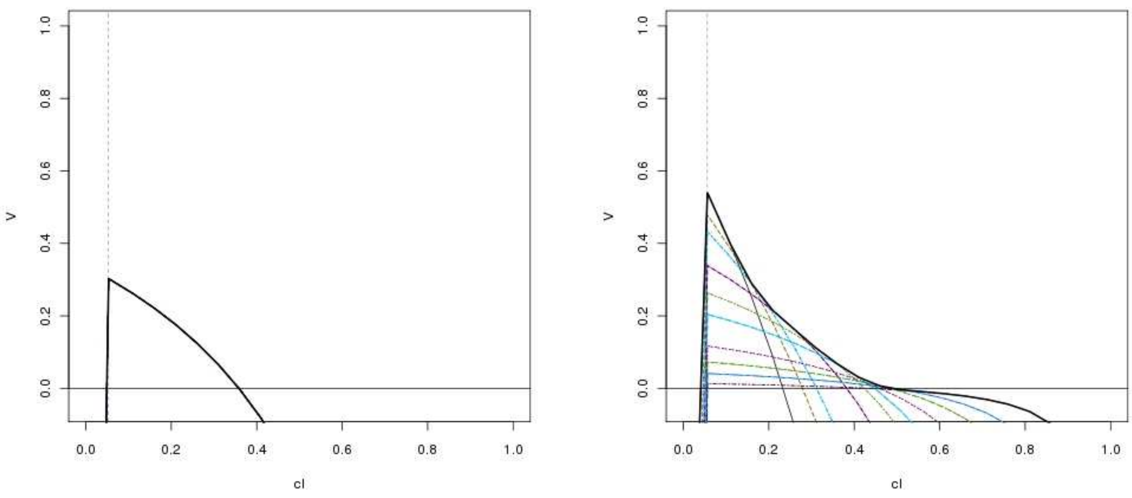

Figure 6: Relative value for DMO (left) and PPPF (right) at Forecast Time +18h and Thresholds=5mm/6h.

takes value 1 and reference 0, so it is positive (negative) if the forecast is better (worse) than reference. The BSS of the system with DX=6 and DT=1 is always positive, for all the thresholds and all the time steps and this means that the PPPF has more accuracy than the DMO (see Fig. 5).

Another diagnostic to measure the possible add value of the PPPF in respect to the DMO is the relative value (Richardson, 2000). This score is related to forecast resolution, but inserts the performance into a decision-making framework. The relative value V quantifies the usefulness of a forecast in minimizing the economic costs associated with protecting against the effects of bad weather and the losses incurred when bad weather occurs but the user did not take protective action. The improvement in economic value of the forecast is measured relatively to a climatology forecast and it is plotted as a function of the cost-loss ratio C/L. The relative value curves shown here are relative to forecast time +18h and to threshold 5 mm/6h (Fig. 6). For the PPPF box the lighter curves represent the relative value as a function of C/L using each of the probabilities (in this case, 0.0, 0.1, 0.2, ... 1.0) as a yes/no threshold for the forecast, while the heavy curve is the envelope representing the maximum relative value possible. The maximum PPPF relative value of 0.55 occurred for C/L close to 0.08, which is the climatological frequency of rain in the sample. These plots show:

- the PPPF have an added-value with respect to the DMO;
- the PPPF have value for all decision makers except those with very low C/L ratios or C/L ratios greater then 0.4.

4 Conclusions

The main conclusions could be here summarized:

- this method of post-processing improves the DMO;

- the best performances are found with DX=12 and DT=1, but the differences with respect to DX=6 and DT=1 are not sufficiently large to justify more CPU costs. Therefore we use operationally DX=6 and DT=1.

There are also some general observations:

- probabilistic forecasts provide an estimate of uncertainty that may be very useful for forecasters and end users;
- a direct link exists between probabilities and C/L;
- this approach should be complementary with an ensemble prediction system since they answer to different questions. For example:
  - EPS: will there be convection/front in a general area ?
  - PPPF: if there is convection/front, what will the peak precipitation be and where is it most likely to be located ?

References

Kaufmann, P., 2007: Post-processing of the aLMo Precipitation with the Neighborhood Method. COSMO Newsletter No. 7.

Richardson, D.S., 2000: Skill and relative economic value of the ECMWF ensemble prediction system. Quart. J. Royal Meteorol. Soc., 126, 649-667.

Theis, S., Hense, A., Damrath, U., and Renner, V., 2002: Ensemble Prediction and Statistical Post-processing of Weather Parameters. COSMO Newsletter No. 2.

Theis, S., Hense, A., Damrath, U., and Renner, V., 2003: Deriving Probabilistic Precipitation Forecasts from LM Simulations. COSMO Newsletter No. 3.

Theis, S., 2005: Deriving probabilistic short-range forecasts from a deterministic high-resolution model. Ph. D. thesis, University Bonn, Germany.

Theis, S., Hense, A., and Damrath, U., 2005: Probabilistic precipitation forecasts from a deterministic model: a pragmatic approach. Meteorological Applications, 12, 3, 257-268.

Wilks, D.S., 1995: Statistical Methods in the Atmospheric Sciences. An Introduction. Academic Press, San Diego, 467 pp.

QPF verification for 2007: COSMO-I7, COSMO-7, COSMO-EU, COSMO-ME, COSMO-I2, COSMO-IT.

Elena Oberto, Massimo Milelli

ARPA Piemonte, Via Pio VII 9, I-10135 Torino, Italy

1 Introduction

In this report we present the QPF verification of 4 model versions at 7 km resolution (COSMO-I7, COSMO-7, COSMO-EU, COSMO-ME) and 2 model versions at 2.8 km resolution (COSMO-I2, COSMO-IT). The observations come from the high resolution network of rain gauges of the COSMO dataset and Civil Protection Department, i.e. about 1300 stations. We show an update of the most recent results highlighting the failings and improvements of the model: the skills and scores are calculated considering 6h or 24h averaged cumulated observated/forecasted precipitation value over 90 meteo-hydrological basins that cover all the peninsula with the exception of two Southern regions: Sicilia and Puglia (see Fig. 1). In detail, we show:

- scores over a long period (seasonal trend);
- verification over last year (200706-200806).

Figure 1: Italian high resolution raingauge distribution.

2 Long period verification

We evaluated the seasonal skills (BIAS, ETS, FAR, POD) for 0.2, 2, 10, 20 mm/24h for the first and the second day starting from DJF 2004 to MAM 2008 for COSMO-I7 and COSMO-7, from MAM 2006 to MAM 2008 for COSMO-EU and from DJF 2006 to MAM 2008 for COSMO-ME. The reason for this discrepancy is the different availability of the data. In the following pictures only BIAS (see Fig. 2 left) and POD (see Fig. 2 right) for 20 mm/24h are shown and we can suggest the following remarks:

- there is a certain periodicity that shows in general that fall and summer have the best and worst skills respectively;
- the error periodicity is usually amplified with the increasing of the threshold;
- BIAS and FAR reduction and ETS increase have been achieved over a long period;
- POD obtains globally contradictory results whit general worsening for low thresholds and improvement for high thresholds, but only for COSMO-7 and COSMO-I7;
- COSMO-I7 and COSMO-7 have a similar error behavior, especially during last period, with a general worsening of the performance;
- COSMO-EU and COSMO-ME show similar trends and performances.

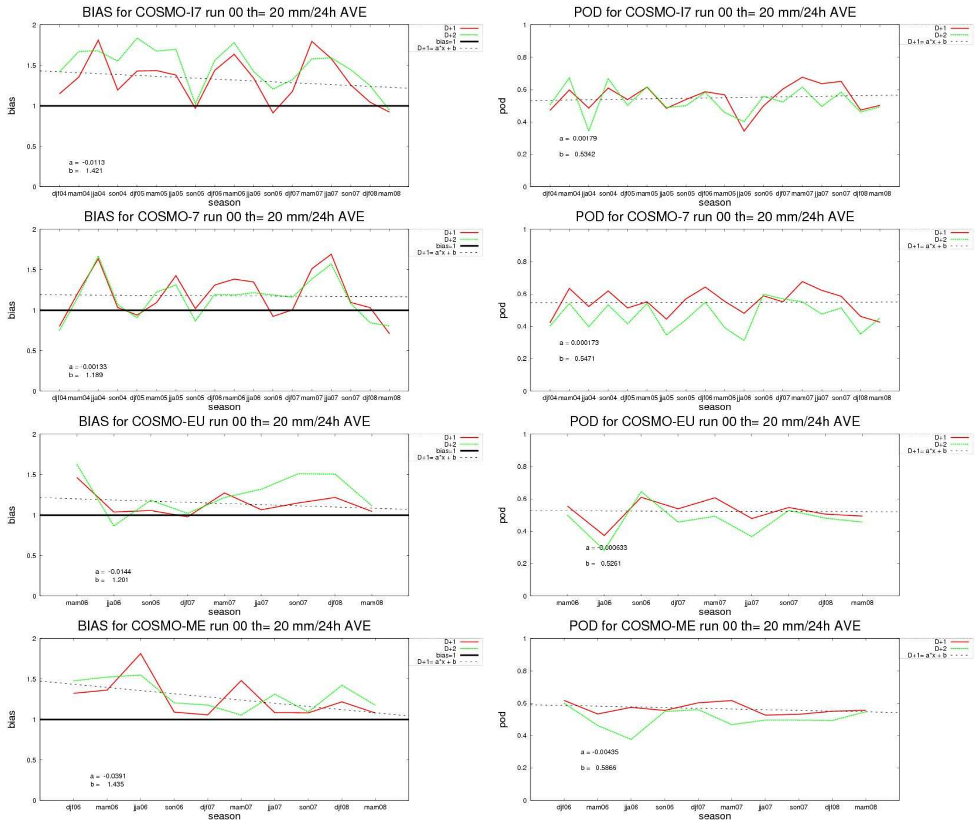

Figure 2: Seasonal trends (dashed line) for the various model versions, starting from DJF 2004 to MAM 2008 for 20 mm/24h threshold: D+1 (red) and D+2 (green) respectively. BIAS on the left side and POD on the right side.

3 Verification over last year

A focus on the verification over last year is reported here, in the second part of the work. Starting from June 2007 to June 2008 we analyze the feature and performance of the 6 model versions, 4 at 7 km resolution and 2 at 2 km resolution. A scheme to summarize the meaning of the main statistical indices used for categorical forecasts is shown in Fig. 3: we add a fifth index that takes into account the correct negative term in the contingency table and it represents the *specificity*, that is the percentage of correctly forecasted not-event.

	FORECASTED	
OBSERVED	NO	YES
NO	A	B
YES	C	D

MEANING	INDEX	RANGE	IDEAL VALUE
Overestimation/ underestimation	$BIAS = \frac{B+D}{C+D}$	[0, ∞]	1
% correctly forecasted events	$POD = \frac{D}{C+D}$	[0,1]	1
False alarme ratio	$FAR = \frac{B}{B+D}$	[0,1]	0
Eq. Threat Scores	ETS	[-1/3,1]	1
% correctly forecasted not-events (specificity)	$1\text{-}POFD = \frac{A}{B+A}$	[0,1]	1

Figure 3: Indices table.

A comparison between COSMO-7/COSMO-EU is reported in Fig. 4, with the five statistical indices and the number of cases, using a bootstrap technique developed by Hamill: in order to compare two model versions, it is necessary to have a confidence interval in order to assess the real differences between skills and scores. We consider the average precipitation values over each meteo-hydrological basin and the error bars indicate the 2.5th and 97.5th percentiles of a resampled distribution, applied to the *reference* model.

There are no significant differences between the two versions with the exception of a slightly improvement on average for COSMO-7. But, if we plot the season indices we can appreciate some strong difference (see Fig. 5):

- COSMO-EU seems to have a quite stable overestimation and the other indices do not show a strong periodicity;
- COSMO-7 shows a strong decreasing of BIAS and POD: the BIAS has a very big overestimation during last summer and a big underestimation during last spring. POD has a worsening during the latest two season.

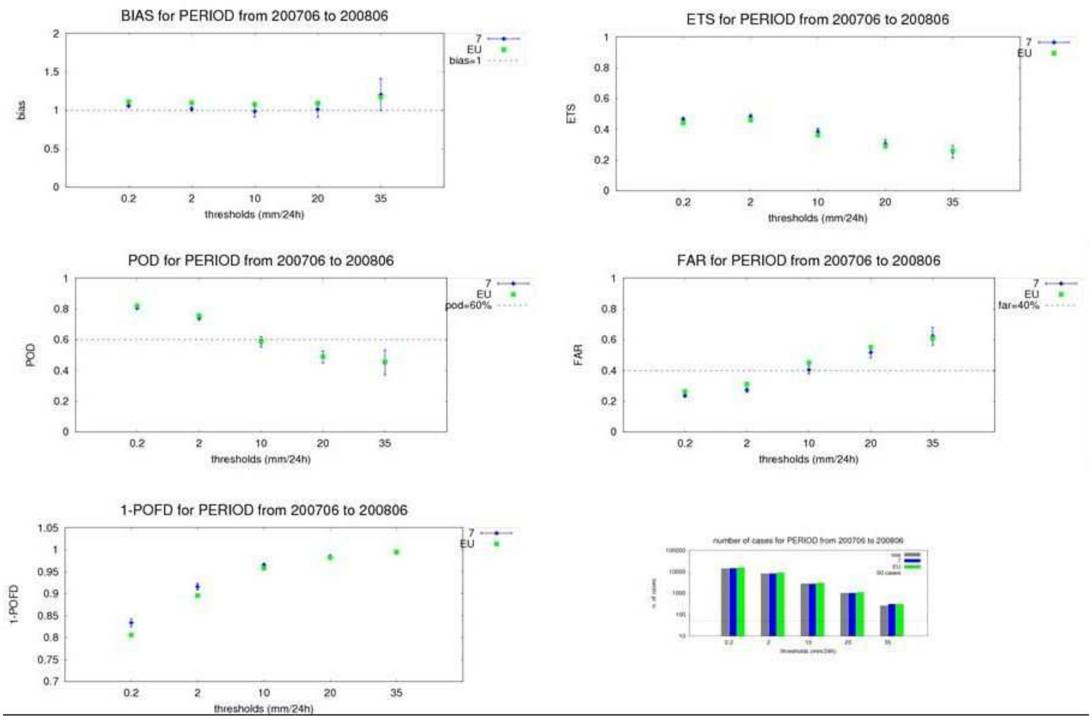

Figure 4: COSMO-EU/COSMO-7: BIAS, ETS, POD, FAR and number of cases during 200706-200806.

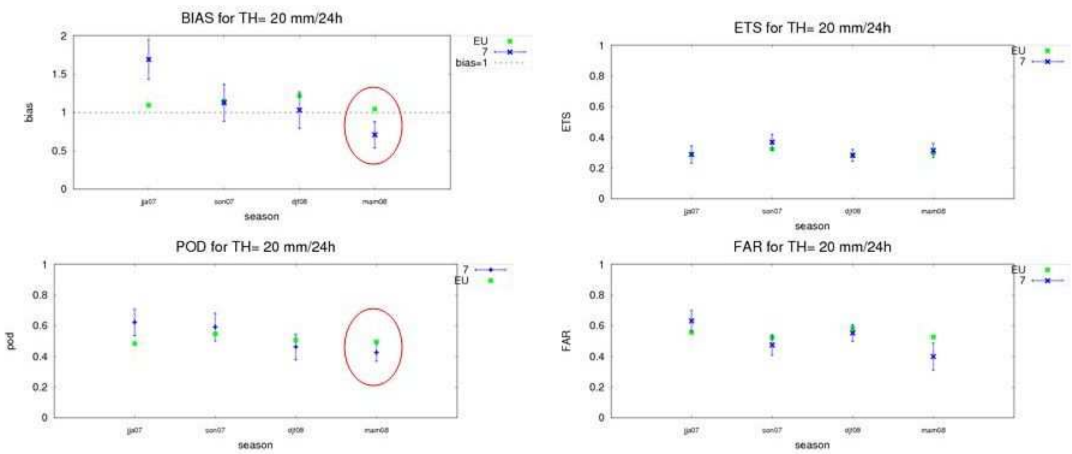

Figure 5: COSMO-EU/COSMO-7: BIAS, ETS, POD, FAR seasonal trend during last year.

Similarly, a comparison between COSMO-I7/COSMO-ME over the whole period is not so significant but, some peculiarity is noticeable if we look at the seasonal indices (see Fig. 6):

- COSMO-ME seems to have a behavior similar to COSMO-EU, with a quite stable overestimation without periodicity;
- in addition, COSMO-I7 seems to have a behavior similar to COSMO-7, with strong BIAS and POD decrease and with a general worsening during the latest seasons.

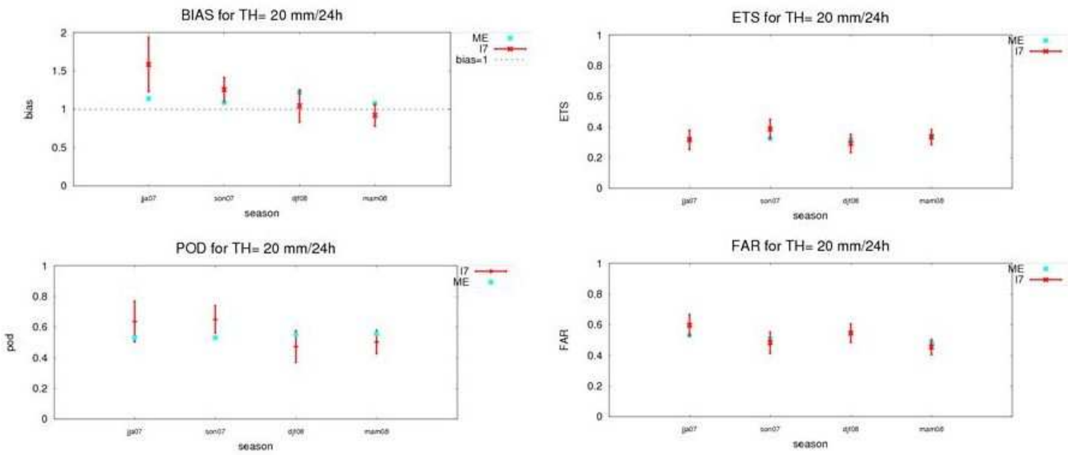

Figure 6: COSMO-I7/COSMO-ME: BIAS, ETS, POD, FAR seasonal trend during last year.

Now we present the results for 2.8 km model versions over a complete period (1 year), with a comparison between COSMO-I7/COSMO-I2, the Italian model versions (7 km and 2.8 km) run in Bologna, and COSMO-ME/COSMO-I2, the Italian model version (7 km and 2.8 km) run in Rome. The COSMO-I7 and COSMO-I2 seasonal error is shown in Fig. 7, where COSMO-I2 seems to follow COSMO-I7 trend, with a strong positive bias last summer (probably because the deep convection parameter was on at that time) and a negative bias this spring.

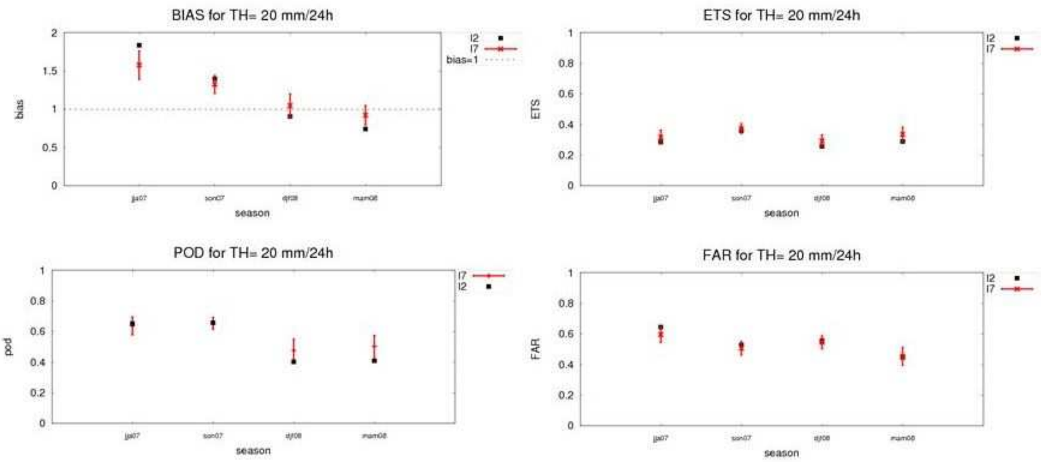

Figure 7: BIAS, ETS, POD, FAR seasonal trend during last year for COSMO-I7/COSMO-I2.

Concerning to the comparison between COSMO-ME/COSMO-IT, as we note in Fig. 8, the two models seem to have a similar trend with a BIAS greater than one.

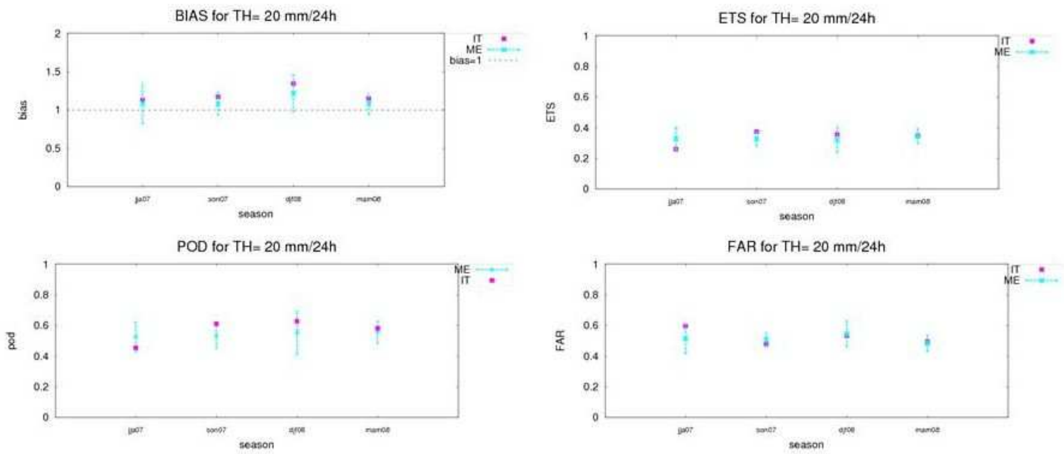

Figure 8: BIAS, ETS, POD, FAR seasonal trend during last year for COSMO-ME/COSMO-IT.

Finally, we show in Fig. 9 some results concerning the diurnal cycle: we considered 6h averaged cumulated observated/forecasted precipitation from June 2007 to June 2008 for all the six model versions with different thresholds, starting from 0.2 mm up to 10 mm. For low thresholds all the models present a bias overestimation peak at midday, while the best value peak for POD, ETS and FAR occurs around the afternoon. Moreover, it is noticeable a spin-up problem for all the models especially for COSMO-I7 and COSMO-I2 that seems to disappear for higher thresholds.

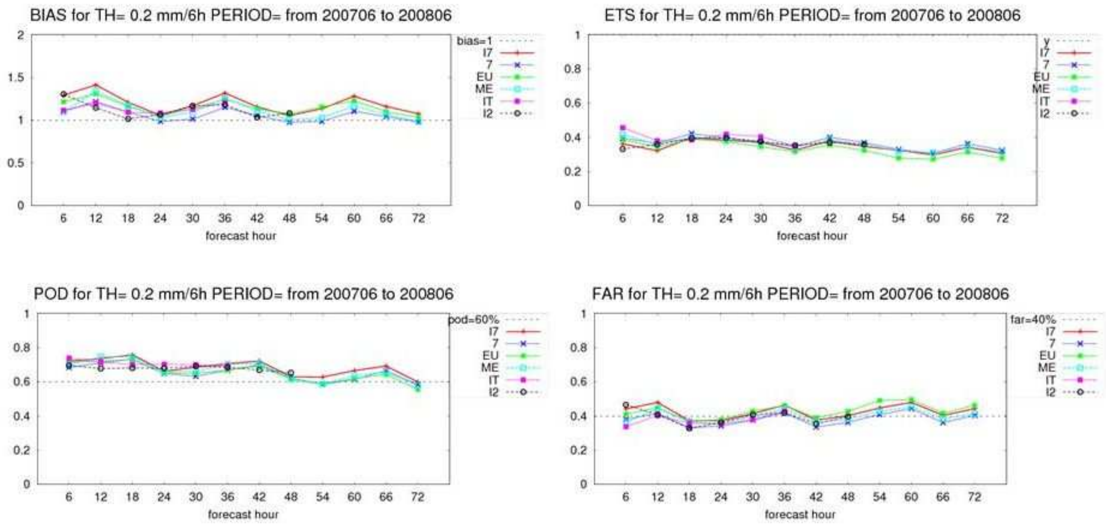

Figure 9: BIAS, ETS, POD, FAR for 6h cumulated precipitation of the six model versions.

Comparison of COSMO models and Multimodel SuperEnsemble outputs in Piemonte

Daniele Cane, Massimo Milelli

ARPA Piemonte, Via Pio VII 9, I-10135 Torino, Italy

1 Introduction

In the framework of the COSMO consortium we have already developed the Multimodel SuperEnsemble technique (Krishnamurti et al., 2000). We applied it to temperature, relative humidity, wind speed and precipitation during the XX Olympic Winter Games of Torino 2006 over the Olympic area (Cane and Milelli, 2005). Moreover we use it operationally over Piemonte, in comparison with other post-processing results (Milelli and Cane, 2006, Cane and Milelli, 2006). The technique consists in weighting the forecasts from several models with a set of weights calculated in the so-called training period by comparison with the observed data. For a complete description of our implementation of Multimodel SuperEnsemble please refer to the publications listed above. In this paper we will show the scores of this technique over a long period and over a wide sample of weather stations covering Piemonte region, together with a comparison of the results of the COSMO models covering the area. In order to better compare the post-processing outputs with the direct model outputs, the results of the models are unbiased with respect to their mean BIAS in the verification period. The Multimodel SuperEnsemble here shown is the operational version calculated with the ECMWF IFS model and the COSMO-I7 model, combining the 00 UTC and 12 UTC runs. The training period of 145 days is obtained with a moving window before the day of the forecast, then the model weights are not fixed in time but vary from day to day, as described in Cane and Milelli, 2006. The statistics here shown are relative to a whole year, from September 2007 to August 2008.

2 Temperature results

The observed data come from the very dense non-GTS weather station network managed by Arpa Piemonte. The stations are grouped by height: 127 low-lying stations (h $<$ 700 m), 77 middle-mountain stations (700 m $<$ h $<$ 1500 m) and 72 high-mountain stations (h $>$ 1500 m). These three groups reflect a standard height division and allow us to distinguish between plains, valleys and higher mountain areas of Piemonte. We evaluated the forecast improvement by comparison with observed values in the given period. The models are interpolated to the station point with horizontal bi-linear interpolation and a vertical correction with station height is applied. Here are shown the results of 6h values of temperature up to +72h forecast, because 6h is the common interval of data availability for the different models. Only the 00 UTC results are shown, but the 12 UTC runs scores do not differ very much. For each height we draw the mean error and the root mean square error. Fig. 1 shows the results for the diurnal cycle of temperature: the COSMO models usually underestimate the 12 UTC forecasts, while they overestimate the 00 UTC temperatures. The biases increase with the height. COSMO-I7 is slightly better in the evaluation of the plains temperatures in comparison to the other models, while it worsens in the higher levels, where a slight predominance of COSMO-7 can be observed, in particular at noon. Multimodel SuperEnsemble is working very well in the bias (close to 0 °C) and RMSE (near 2 °C), always obtaining better results than the models; the SuperEnsemble errors are also stable with the forecast time.

Fig. 2 shows the results for the extreme temperatures: as expected, the COSMO models underestimate maxima and overestimate minima. Again, the COSMO-I7 model is better in the lower-level stations, while in this case there is no difference in the behavior of the models at higher elevations. The Multimodel SuperEnsemble behaves very well again, with a reduction of the bias practically to zero and RMSE in the range of 10-15 %.

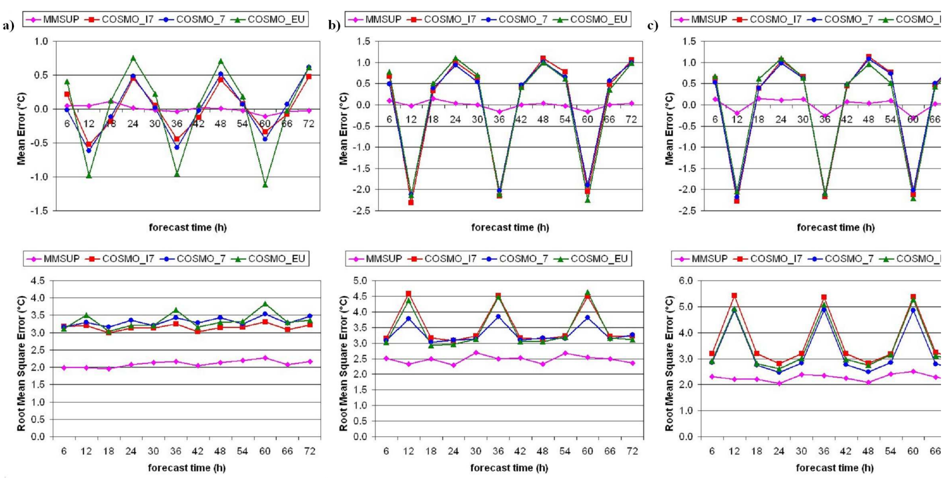

Figure 1: Temperature forecast errors compared to observations by Multimodel SuperEnsemble (purple), COSMO-I7 (red), COSMO-7 (blue) and COSMO-EU (green) in the period September 2007-August 2008. a) stations below 700 m; b) stations between 700 m and 1500 m; c) stations above 1500 m.

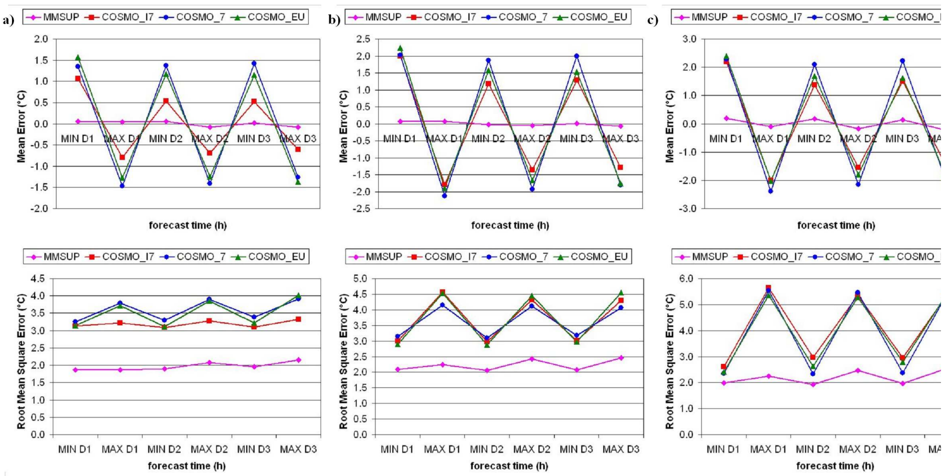

Figure 2: Extreme temperature forecast errors compared to observations by Multimodel SuperEnsemble (purple), COSMO-I7 (red), COSMO-7 (blue) and COSMO-EU (green) in the period September 2007-August 2008. a) stations below 700 m; b) stations between 700 m and 1500 m; c) stations above 1500 m.

3 Humidity results

For the relative humidity the models are again interpolated to the station point with horizontal bi-linear interpolation and vertical correction with station height is applied. Fig. 3 shows the results for humidity: the COSMO models usually overestimate RH at 12 UTC forecasts and underestimate at 00 UTC forecasts. In this case the error decreases with the height, as expected due to difficulty of forecasting the humidity at lower locations. The three models behave quite similarly, apart from the stations over the plains, where COSMO-I7 has slightly better results, while COSMO-7 is clearly worse than the others. The Multimodel SuperEnsemble is working again very well in the bias and RMSE reduction, always obtaining better results than the models; the SuperEnsemble errors are also stable with the forecast time. It is quite noticeable the behavior of this post-processing technique applied to a parameter like the relative humidity, which is quite difficult to manage with other post-processing techniques (like Kalman filter, see Kalman, 1960) because gaussian distribution of the forecast errors is required. This hypothesis is not required by the Multimodel SuperEnsemble technique.

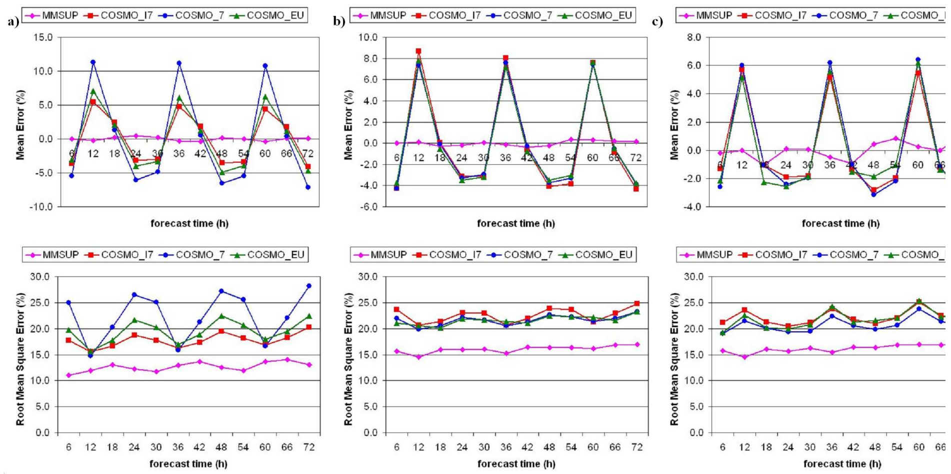

Figure 3: Relative humidity forecast errors compared to observations by Multimodel SuperEnsemble (purple), COSMO-I7 (red), COSMO-7 (blue) and COSMO-EU (green) in the period September 2007-August 2008. a) stations below 700 m; b) stations between 700 m and 1500 m; c) stations above 1500 m.

4 Wind speed results

Wind speed is calculated from the model by extracting the nearest grid point to the station, both in the horizontal and in the vertical. Due to data availability, only the COSMO-I7 and COSMO-EU results are shown here. Fig. 4 shows the results for the wind speed: the COSMO models underestimate the wind intensity at 12 UTC forecasts, while they usually overestimate at 6 UTC forecasts. The COSMO-I7 model performs better for the lower level stations, while the COSMO-EU is better at higher elevations. The post-processed data by Multimodel SuperEnsemble are again performing well, with RMSE in the range of 1-1.5 m/s.

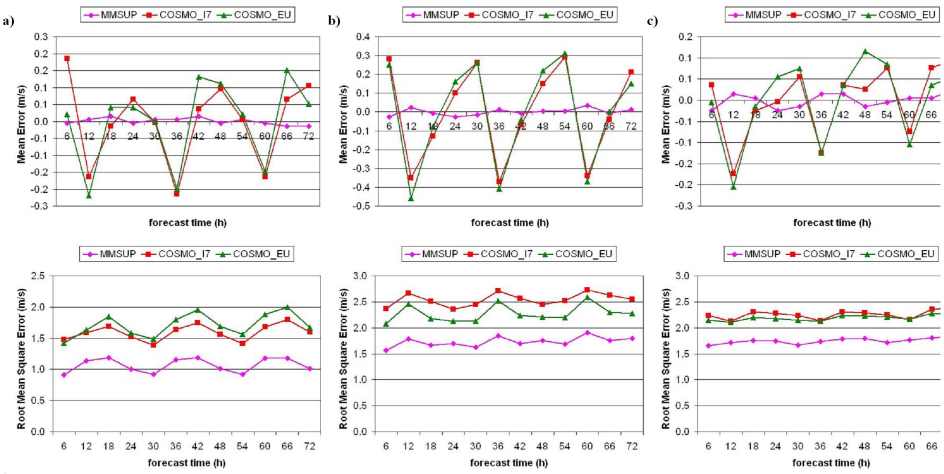

Figure 4: Wind speed forecast errors by compared to observations Multimodel SuperEnsemble (purple), COSMO-I7 (red), COSMO-7 (blue) and COSMO-EU (green) in the period September 2007-August 2008. a) stations below 700 m; b) stations between 700 m and 1500 m; c) stations above 1500 m.

4 Conclusion

A large number of stations are used for the validation of the COSMO models and the Multimodel SuperEnsemble outputs in the Piemonte area over a whole year. There is a slight prevalence of COSMO-I7 in the parameters over the plains, while COSMO-7 and COSMO-EU show better results at higher elevations. The Multimodel SuperEnsemble technique is very effective in reducing the forecast errors at every height and forecast time.

References

Krishnamurti, T.N., Kishtawal, C.M., Larow, T., Bachiochi, D., Zhang, Z., Williford, C.E., Gadgil, S., Surendran, S., 2000: Multi-Model Superensemble Forecasts For Weather And Seasonal Climate. J. Climate, 13, 41964216.

Cane, D., Milelli, M., 2005: A new method for T2m forecast in complex orography areas. COSMO Newsletter n. 5, 151-157.

Milelli, M., Cane, D., 2006: Use of Multimodel SuperEnsemble Technique for complex orography weather forecast. COSMO Newsletter n. 6, 146-151.

Cane, D., Milelli, M., 2006: Weather forecasts with Multimodel SuperEnsemble Technique in a complex orography region. Meteorologische Zeitschrift, 15, 2, 207-214.

Kalman, R.E., 1960: A new approach to linear filtering and prediction problems. Journal of Basic Engineering, 82 (1), 3545.

Seasonal verification over Poland

Katarzyna Starosta and Joanna Linkowska

Institute of Meteorology and Water Management, Centre of Numerical Weather Prediction, Poland

1 Introduction

The surface fields of the LM_ PL have been verified for Polish SYNOP stations and the precipitation field has been verified for rain gauges. For the verification before June 2007, the model data were retrieved from model version 3.5. For verification after that date, the model data are retrieved from model version 4.0. The model runs in an operational mode at 14-km grid spacing, twice a day 00 UTC and 12 UTC.

2 Surface verification

The LM_PL had been verified for all seasons from June 2007 to May 2008 JJA, SON, DJF, MAM. The mean error (ME) and the root square mean error (RMSE) were calculated for the following parameters: the temperature at 2m (T2m), the dew point at 2m (TD2m), the wind speed 10m (Wspeed) and the pressure reduced to mean sea level (MSLP). ME and RMSE were calculated using 8 forecast time points (every 6 hours) for 48 hours forecast starting at 00 UTC. ME and RMSE of the surface variables as a function of the forecast time are presented on figures 1 - 4.

3 Precipitation verification

Verification for the 24hour accumulated precipitation (a comparison with 60 SYNOP stations) had been made for all seasons from June 2007 to May 2008. Seven indices from the contingency table were calculated. In this paper only frequency bias index (FBI), probability of detection (POD) and false alarm ratio (FAR) are presented for thresholds: 0.2, 2, 10, 20 mm. These indices are shown on figures 5-9. Figures 10-21 contain distribution pattern of seasonal precipitation for model, rain gauges (301 stations) and their differences.

4 Results

4.1 The 2 m temperature

Mean error below zero occurred in winter (December, January, February). In spring (March, April, May) and summer (June, July, August) was above zero. In autumn (September, October, November) mean error was around zero. In summer and spring a diurnal cycle of RMSE was observed with maximum at noon (FCT 12, 36 h) and minimum at night (FCT 6, 30 h). No explicit diurnal cycle occurred in winter and autumn.

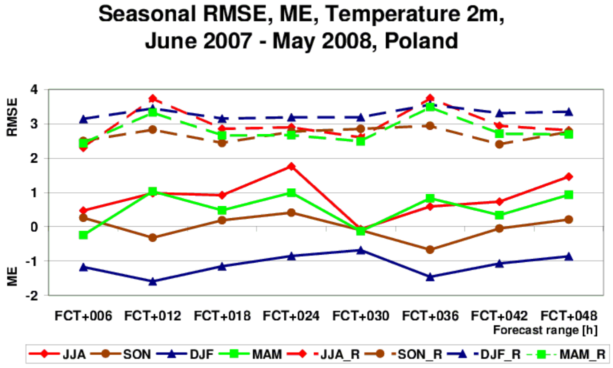

Figure 1: Sesonal RMSE, ME, Temperature 2m, June 2007 - May 2008, Poland

4.2 The dew point temperature at 2m a.g.l

ME around zero in winter and autumn was observed. In summer and spring ME was below zero. Diurnal cycle of RMSE was noticed in summer and spring. There was no explicit diurnal cycle of RMSE for winter and autumn.

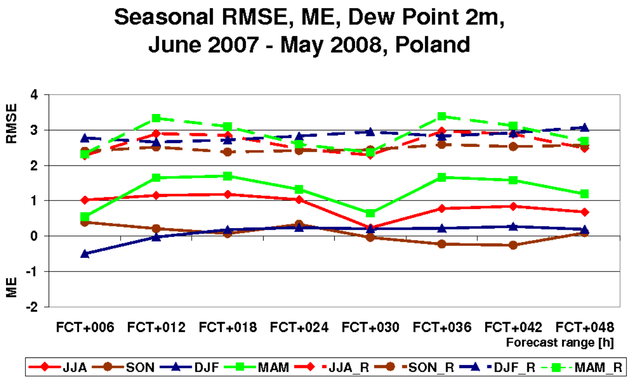

Figure 2: Sesonal RMSE, ME, Dew Point 2m, June 2007 - May 2008, Poland

4.3 The wind speed 10m a.g.l.

In DJF, ME was below zero at noon and above zero at night. ME above zero occurred for JJA SON. In MAM, ME was near zero. Fluctuations of ME for all seasons were really small. ME of wind speed was from [-0.27, 0.64] m/s. Also fluctuations of RMSE for all seasons were very small. No clear diurnal cycle was noticed.

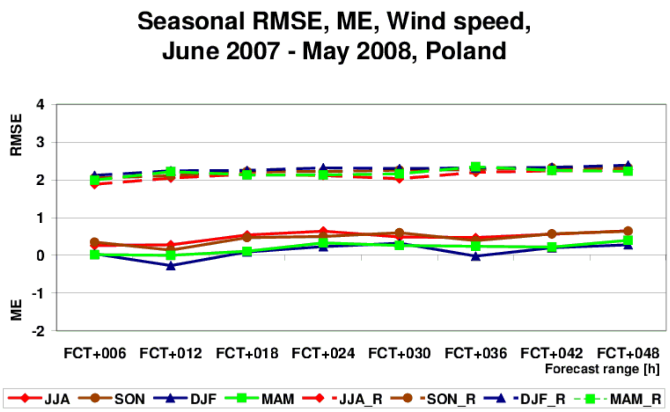

Figure 3: Sesonal RMSE, ME, Wind speed, June 2007 - May 2008, Poland

4.4 The sea level pressure

ME for all seasons increased with forecast time. ME was positive in winter for all the forecast ranges. In autumn and summer ME was near zero (FCT 6h - FCT 18h) and negative (FTC 24h FCT 48h). In spring, ME was negative for almost all forecast ranges. Similar to ME, also RSME increased with forecast time for all seasons. The highest values were observed in winter time (above 3h Pa) and the smallest in summer.

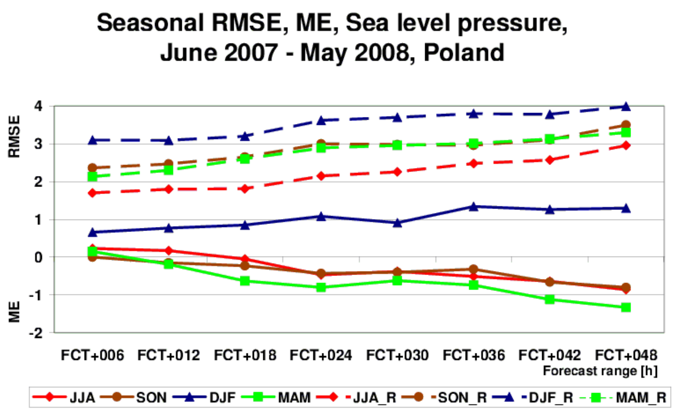

Figure 4: Sesonal RMSE, ME, Sea level pressure, June 2007 - May 2008, Poland

4.5 24h accumulated precipitation

Three indices: Frequency Bias Index, Probability of Detection and False Alarm Ratio computed for two forecast ranges (FCT 24h , FCT 48h) are presented below (fig5 - fig.6). FBI in DJF, for threshold 0.2 mm and 2 mm was above 1 for the both of forecast ranges. It implies over forecasting. FBI between 0.96-1.01 (almost no bias) was noticed for threshold 2 mm for the first forecast day in JJA, SON, MAM and for the second forecast day in JJA. Underestimation of precipitation occurred for higher thresholds (10mm, 20 mm) for the first forecast range in all of the seasons and in summer 2007 and autumn 2007 for the second day of forecast. In winter 2007/2008 and spring 2008 intensive, heavy precipitation was predicted more than in reality occured.

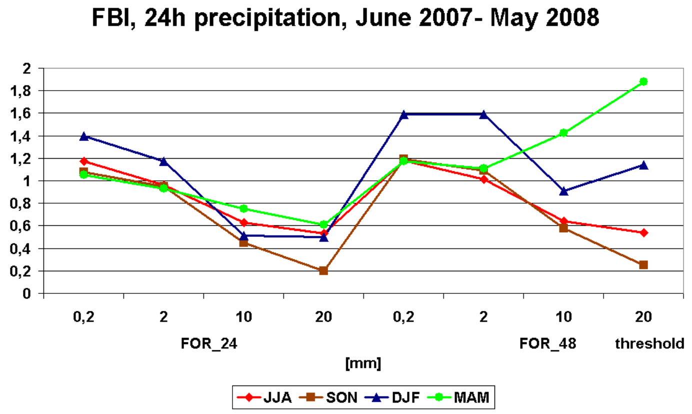

Figure 5: Frequency Bias Index, 24 h accumulated precipitation, the first (FCT_24) and the second (FCT_48) day of forecast, June 2007 - May 2008, Poland

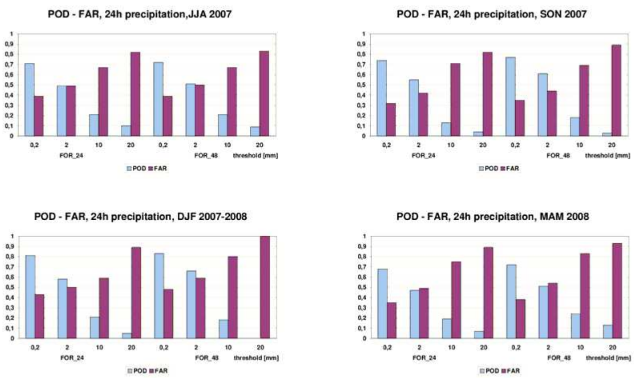

Figure 6: Probability od Detection, False Alarm Ratio, 24 h accumulated precipitation, the first (FCT_24) and the second (FCT_48) day of forecast, JJA 2007,SON 2007, DJF 2007/2008, MAM 2008, Poland

Distribution patterns of precipitation in the spring and the winter showed overprediction for almost whole country area. In summer underestimation occurred in central Poland and also partially near seaside and mountain areas.

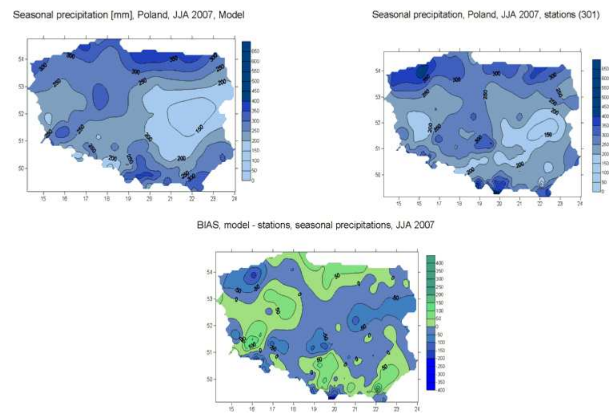

Figure 7: Distribution pattern of seasonal 24 h accumulated precipitation for model, rain gauges (301 stations) and BIAS, JJA 2007, Poland

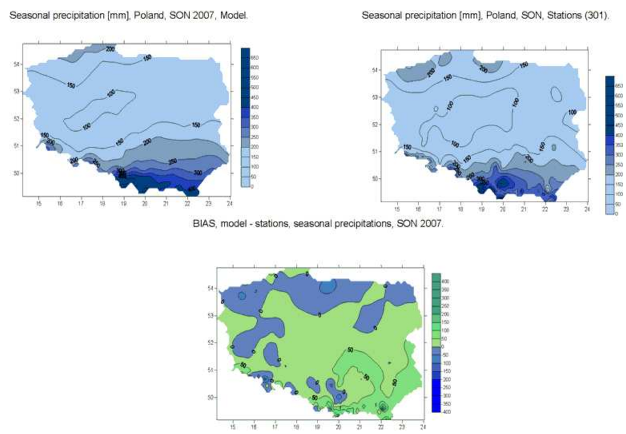

Figure 8: Distribution pattern of seasonal 24 h accumulated precipitation for model, rain gauges (301 stations) and BIAS, SON 2007, Poland

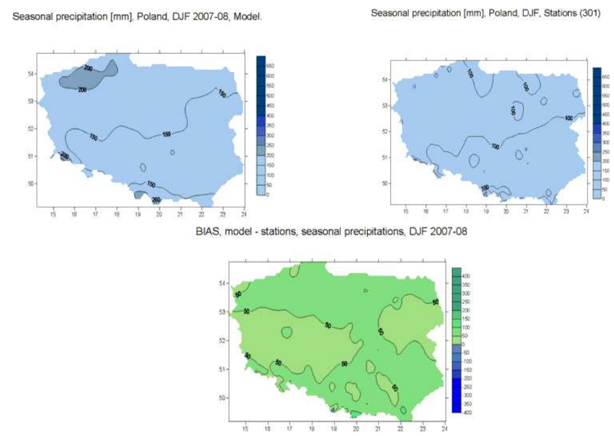

Figure 9: Distribution pattern of seasonal 24 h accumulated precipitation for model, rain gauges (301 stations) and BIAS, DJF 2007/2008, Poland

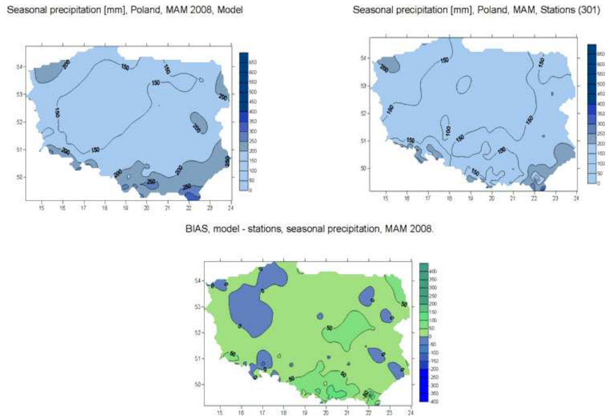

Figure 10: Distribution pattern of seasonal 24 h accumulated precipitation for model, rain gauges (301 stations) and BIAS, MAM, Poland

20^{th} of July 2007 — Explosive Convection over Europe The COSMO Perspective

Jan Parfiniewicz

Institute of Meteorology and Water Management
61 Podlesna str., PL-01673 Warsaw, Poland

1 Introduction

On the 20^{th} of July 2007 an explosive convection weather event has affected a number of European countries: England, Germany, Poland and Ukraine. Severe storms caused extreme floods (Britain and Ukraine) and damaging winds, with a tornado in Poland. For multiscale analysis purpose COSMO-Model simulations with 14 km / 35 levels, 7 km / 50 levels, and 2.8 km / 50 levels (nested) over Europe and Poland have been performed and the 3D history of the giant supercell storm that produced the tornado near Czestochowa has been retrieved. Many synoptic features were correctly reproduced by the model and helped to understand the mechanisms of the case and deduce even such subtle processes like right and left moving wind patterns of tornado convective system. Nevertheless the cloud water convective structures as simulated by the model remains underestimated. One of the fault reasons is that the proper radar assimilation scheme was not adopted, but the second suspicion is that the ageostrophic flow just under the jet stream was not adequately represented. This kind of upper flow caused overriding warm and wet subtropic and even tropic air by the extra cold (arctic) and dry air, thus generating instant upraise of potential instability and explosive convection - the well known mechanism (see Browning, 1985).

2 Understanding the process

On the 12^{th} of July 2007 a deep massive drop of cold arctic air started south of Greenland (see Fig. 1: the temperature field on 300 hPa) to move south-east over north Atlantic towards the British Isles pushing ahead the polar jet branch (see Fig. 2: the air temperature at 20th of July 00 UTC, and the location of the polar jet, Fig.3). These are the key features that control the process on synoptic scale. The polar jet that merges at the moment subtropic jet branch was elongating south-westerly pumping hot and wet tropic air masses towards Europe as seen by temperature field on 850 hPa (Fig. 4). The configuration of isentropic surface 315 K shows the giant hill of cold air related to deep low over south-west Britain as seen via pressure field on 8 km level and embedded jet (Fig. 5). During the next 16 hours the jet was torn out by explosive convection (Fig. 6), still preserving two weakening branches of the main stream: the one towards the British Isles and the second one over Germany and Poland.

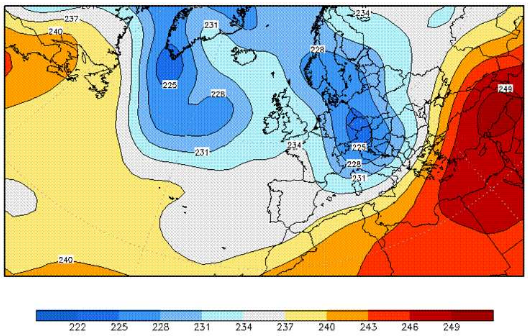

Figure 1: Temperature (K) at 300hPa on 00Z 12 July 2007.

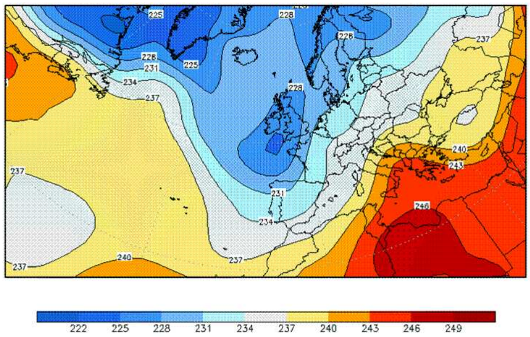

Figure 2: Temperature (K) at 300hPa on 00Z 20 July 2007.

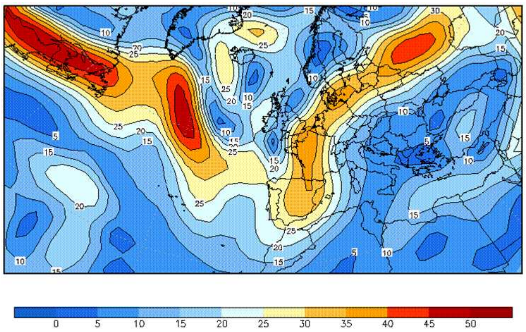

Figure 3: Jet (m/s) at 300hPa on 00Z 20 July 2007.

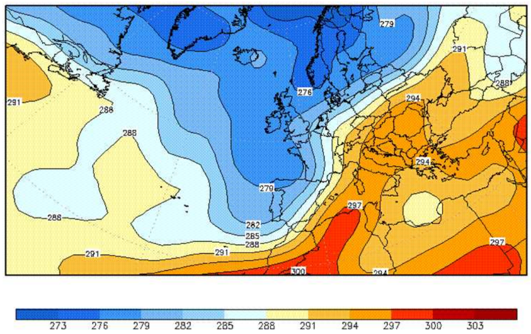

Figure 4: Temperature (K) at 850hPa on 06Z 20 July 2007.

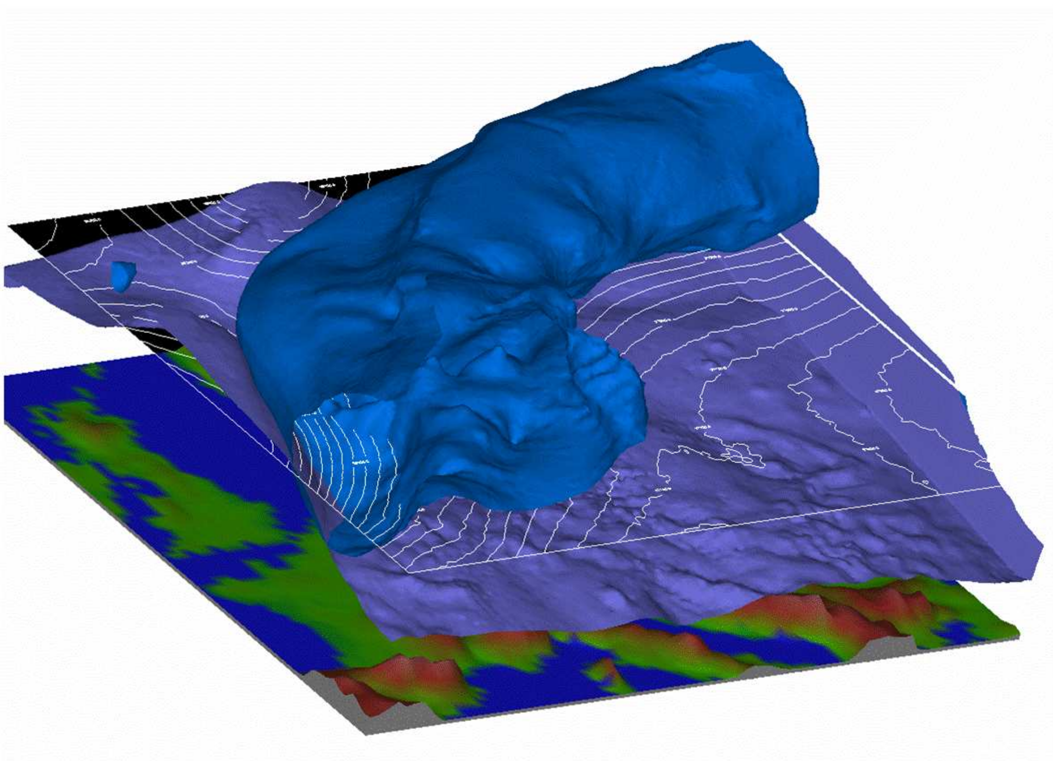

Figure 5: Isentropic surface 315 K and pressure field on 8 km level with embedded jet

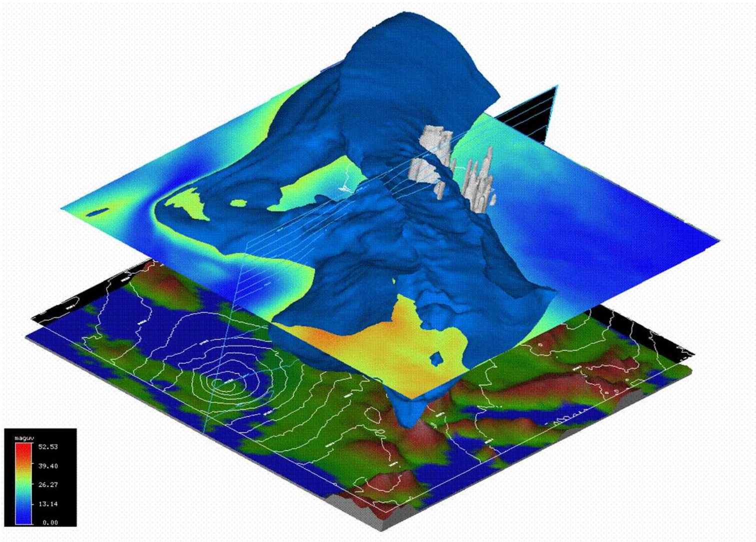

Figure 6: Jet at 30 m/s surface and wind speed on 10.2 km level. Pressure on 1.5 km + radar reflectivity over southern Poland. Vertical cross-section of Potential Temperature – squeezing temperature isopleths represent passage to stratosphere.

3 The model performance – large scale perspective

As the large scale features represented via pressure, horizontal wind and even specific humidity fields were well and satisfactory restored by the model on all resolutions, the cloud water still remains underestimated (see Fig. 7 compared with satellite picture, Fig. 8).

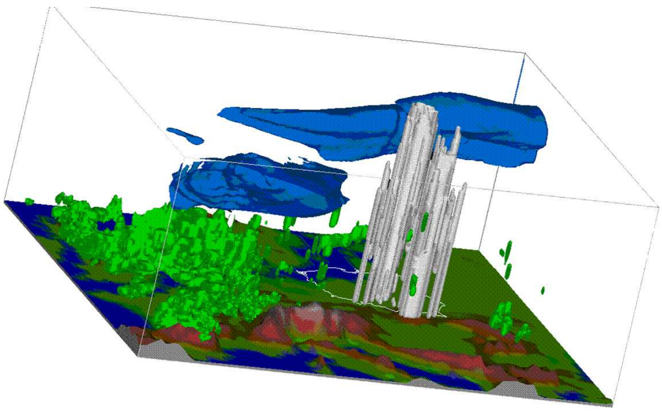

Figure 7: On the 3D picture we have jet-stream (in blue) presented against clouds: a) simulated (for 4h) by model (light green) and b) found by 3 radars (reflectivity in dBZ) over PL (in white). The 2 big white objects are convective complexes, and the one of them near Czestochowa (south-middle Poland) was recognised as a Thunderstorm Supercell – the matter cloud that born tornado beneath. We see the object 30 km wide and 18 km high. Jet-stream and model clouds (cloud water `QC`) are taken from the polish implementation COSMO-PO (Version 4.0, 35 levels / 14 km). However, the modeled cloud water, the radar reflectivity and the respective infrared / thermal satellite band (see Fig. 8) are measured in different units - but all represent clouds and then might be compared, at least visualized, together.

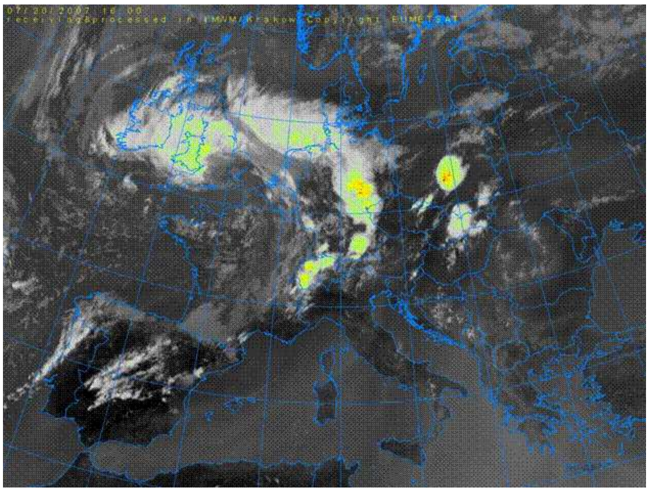

Figure 8: 16Z: Satellite infrared picture. Colored are areas of explosive convection. The picture name is OverShootingTops (OST), also called as *difference image* and represent the difference of brightness temperature of two spectral channels of the satellite Meteosat 9: the channel WV6.2 micrometer (the so called water vapour) and IR10.8 micrometer (infrared). This allows to recognize OverShootingTops (with the difference of brightness temperature > 0) – the most active area of Cb (the strongest updrafts), usually connected with severe thunderstorms with hails. The colors represent: green – still not yet OST (the temperature difference between -3. to 0. C) strong convection reaching tropopause; from yellow to orange to violet - Overshooting tops, cloud tops in stratosphere. The value over +3 (violets) appear very rare. (thanks to Monika Pajek, IMGW – personal communication).

4 The model performance – tornado perspective

The important processes on the tornado forming have been diagnosed as follows:

- upper cold and dry air advection over wet and warm masses,
- lee cyclogenesis in the vicinity of southern Poland mountains,
- the high temperatures growth on the surface,
- the local vorticity transport.

Recognized are five stages of convective situation evolution:

a) decay of previous convective complex; 00-04Z

b) growth and decay of the individual convective cells; 04-10Z

c) creation of convective cluster – the *slow right mover* (the main future supercell body) and the cell *rapid growing left mover* (the future trigger that tornado was generated); 10-14Z

d) The supercell generation by fusion of slow right moving convective complex and the rapidly growing huge Cumulonibus – deduced *left mover*; 14-16Z

e) The mature supercell stage with tornado beneath 16:05 – 16:15Z and huge convective system over Tatry mountains and Slovakia; 16-18Z

An example of transition from stage d) to e) as seen by different means is enclosed beneath.

4.1 The supercell transition from early to mature stage

An example of transition from stage d) to e) as seen by different means is enclosed beneath. Here the vertical mean of radar reflectivity (the upper panel) is presented against 3D composite of radar reflectivity and satellite Meteosat 9 picture from HRV high resolution solar channel.

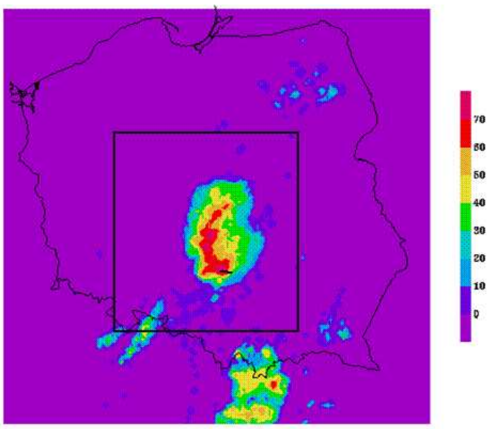

(a) Radar reflectivity on 16Z 20 July 2007.

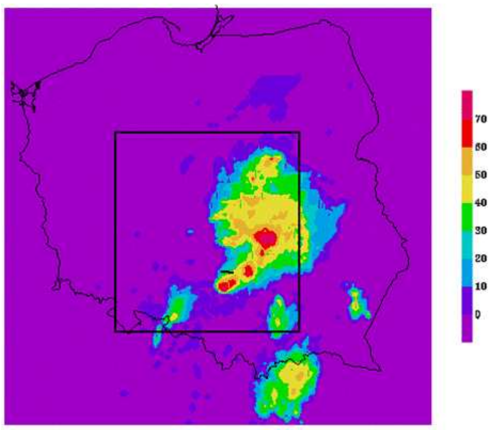

(b) Radar reflectivity on 18Z 20 July 2007.

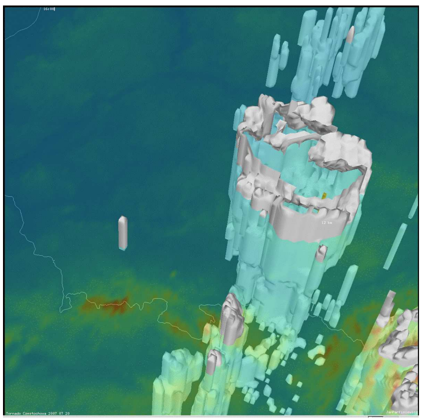

(c)

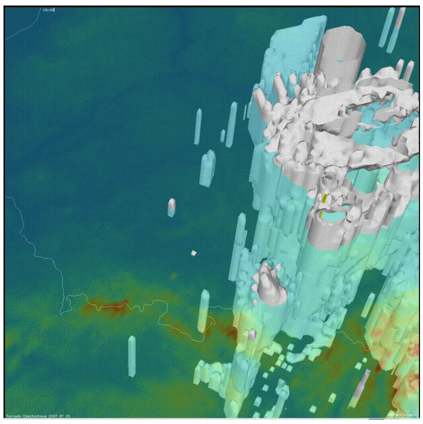

(d)

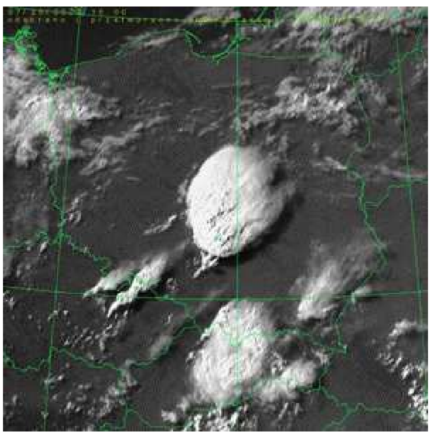

(e)

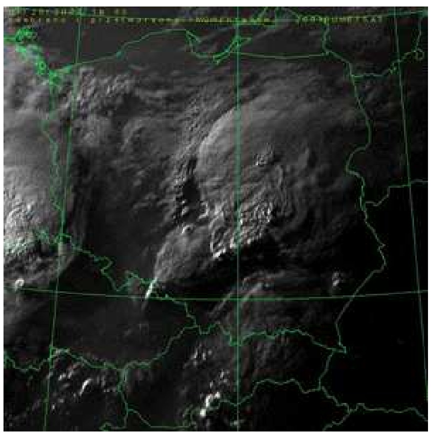

(f)

Figure 9: Supercell transition from early (16 UTC, left column) to mature stage (18 UTC, right column).

4.2 An example of restored tornado related features

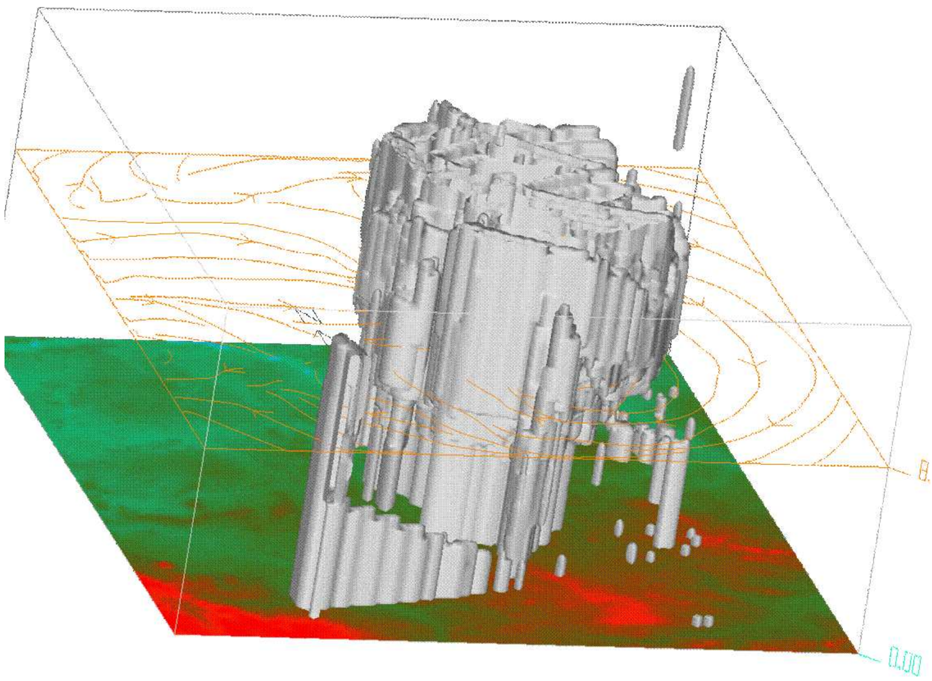

Figure 10: 16Z: Restored 3D supercell structure of the *right mover* type. On the 3D radar reflectivity composite the streamlines of relative motion are super imposed. These relative streamlines depending on the height and must reflect the horizontal vorticity field as taken from the COSMO-PO (Version 4.0 50 levels / 2.8 km). Vertical extent of the domain is 15 km.

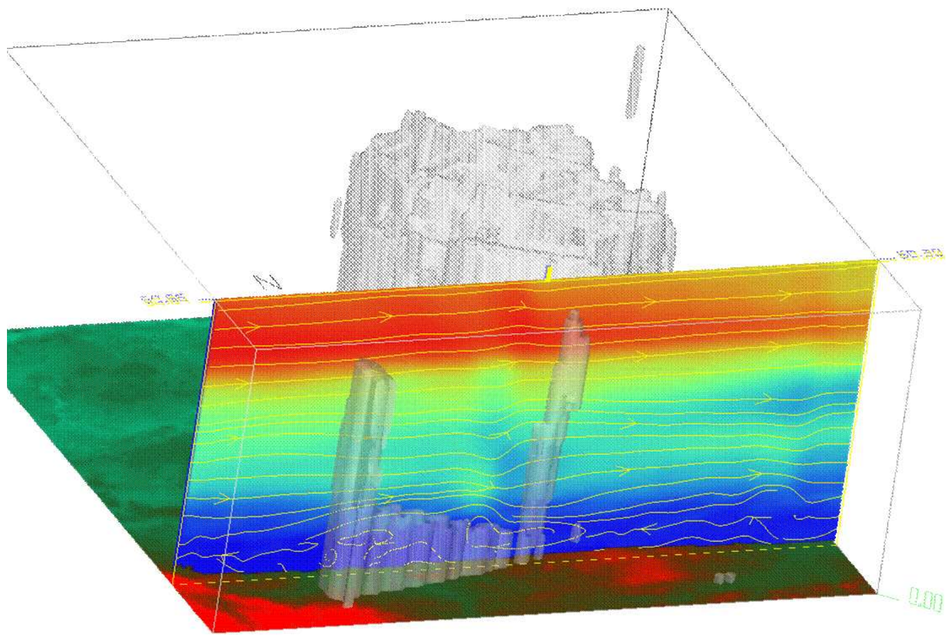

Figure 11: The supercell cross section with streamlines and wind speed as the background. The characteristic typical wind jump and related vortex tube trace as simulated by the COSMO-Model high resolution 2.8 km / 50 levels nested model.

5 Towards a conclusion

Just after K. Browning et al. (2002): *Local severe weather events often occur in association with convection organized on the mesoscale within larger-scale weather systems. Observing, understanding and predicting such events is difficult because of the multiscale nature of such events.* Despite the *difficult nature* of the searched event the COSMO-model shows its capability to cope with the case. All basic features related to pressure, wind, temperature and even specific humidity fields were satisfactory restored. The problem occurred with convective cloud water structures. It is not allowed (e.g. from aviation point of view) to treat big convective objects (like suppercells) stochastically. The overtaking time could be squeezed but reasonable foreseen effect of several hours for suppercells (and possibly 1 hour for tornados) should be performed by the model – at least to keep it as a challenge. The easiest obvious truism would be to quote Browning's conclusion: *Improving the resolution of the model and assimilating more mesoscale observational data will increase its ability to produce very-short-range forecasts of these important features.* Concerning heavy precipitation and explosive convection it was shown that non-orographic effect of upper cold and dry air advection over wet and warm air masses is equally important to be properly represent by the model resolution.

References

Browning, K. A., 1985. Conceptual models of precipitation systems. *The Meteorological Magazine*, **No. 1359, Vol. 114**, pp. 293-319.

Browning, K. A., Panagi, P., Dicks, E.M., 2002. Multi-sensor synthesis of the mesoscale structure of a cold-air comma cloud system. *Meteorol. Appl.*, **9**, pp. 155-175.

List of COSMO Newsletters and Technical Reports

(available for download from the COSMO Website: `www.cosmo-model.org`)

COSMO Newsletters

No. 1: February 2001.

No. 2: February 2002.

No. 3: February 2003.

No. 4: February 2004.

No. 5: April 2005.

No. 6: July 2006; Proceedings from the COSMO General Meeting 2005.

No. 7: May 2008; Proceedings from the COSMO General Meeting 2006.

No. 8: August 2008; Proceedings from the COSMO General Meeting 2007.

COSMO Technical Reports

No. 1: Dmitrii Mironov and Matthias Raschendorfer (2001):
Evaluation of Empirical Parameters of the New LM Surface-Layer Parameterization Scheme. Results from Numerical Experiments Including the Soil Moisture Analysis.

No. 2: Reinhold Schrodin and Erdmann Heise (2001):
The Multi-Layer Version of the DWD Soil Model TERRA_LM.

No. 3: Günther Doms (2001):
A Scheme for Monotonic Numerical Diffusion in the LM.

No. 4: Hans-Joachim Herzog, Ursula Schubert, Gerd Vogel, Adelheid Fiedler and Roswitha Kirchner (2002):
LLM ⁻ the High-Resolving Nonhydrostatic Simulation Model in the DWD-Project LITFASS.
Part I: Modelling Technique and Simulation Method.

No. 5: Jean-Marie Bettems (2002):
EUCOS Impact Study Using the Limited-Area Non-Hydrostatic NWP Model in Operational Use at MeteoSwiss.

No. 6: Heinz-Werner Bitzer and Jürgen Steppeler (2004):
Documentation of the Z-Coordinate Dynamical Core of LM.

No. 7: Hans-Joachim Herzog, Almut Gassmann (2005):
Lorenz- and Charney-Phillips vertical grid experimentation using a compressible nonhydrostatic toy-model relevant to the fast-mode part of the 'Lokal-Modell'

No. 8: Chiara Marsigli, Andrea Montani, Tiziana Paccagnella, Davide Sacchetti, André Walser, Marco Arpagaus, Thomas Schumann (2005):
Evaluation of the Performance of the COSMO-LEPS System

No. 9: Erdmann Heise, Bodo Ritter, Reinhold Schrodin (2006):
Operational Implementation of the Multilayer Soil Model

No. 10: M.D. Tsyrulnikov (2007):
Is the particle filtering approach appropriate for meso-scale data assimilation?

No. 11: Dmitrii V. Mironov (2008):
Parameterization of Lakes in Numerical Weather Prediction. Description of a Lake Model.